DYNAMICS IN THE ANVIL OUTFLOW OF TROPICAL CONVECTION

JERUSHA ISABEL LEDERMAN

A DISSERTATION SUBMITTED
TO THE FACULTY OF GRADUATE STUDIES
IN PARTIAL FULFILLMENT FOR THE DEGREE OF
DOCTOR OF PHILOSOPHY

GRADUATE PROGRAM IN EARTH AND SPACE SCIENCE
YORK UNIVERSITY
TORONTO, ONTARIO

January, 2015

Abstract

This thesis presents results of an experiment to investigate the dynamics of air motions within the outflow of tropical deep convection in the upper troposphere above Darwin, Australia. The research involved analyzing in situ measurements within the anvil outflow from the Egrett aircraft and also coincident laser remote sensing measurements of cloud structure from a King Air aircraft, flying directly below the Egrett. The data included the only in situ turbulence measurements that have been obtained with a resolution of 4 meters inside of an anvil outflow.

The research shows that gravity waves and coherent structures exist in the anvil outflow. High frequency gravity waves were identified from the 90^{o} phase lag between temperature and vertical wind oscillations. The gravity waves had wavelengths of 2 – 5 km and were observed as isolated waves with less than two oscillations, or, as extended waves with several oscillations. In some instances, correlations between temperature and vertical wind oscillations had zero phase lag between them and this was consistent with Rayleigh-Bénard convective rolls. Turbulence in the outflow was observed to be intense within patches separated by more quiescent flow. This turbulence had some characteristics that were unique in comparison to previous turbulence measurements at similar altitudes in the jet stream or midlatitude cirrus clouds. The ratio of the power spectral density of vertical wind fluctuations to the horizontal wind fluctuations was greater in the anvil outflow in comparison to the measurements in turbulence generated by shear in mid latitude jet stream and cirrus clouds. The relative magnitude of the vertical wind fluctuation spectrum decreases at all wavelengths with increasing distance away from the core region of the storm. This constitutes the first evidence that is consistent with theoretical predictions of "stratified turbulence."

Measurements in flights above and below the outflow base indicate that momentum flux is directed both upward and downward, away from the cloud base. This suggests the combination of shear and undulations in the cloud base are a mechanism for generating the observed high frequency gravity waves. This mechanism has not been previously identified from measurements or theoretical modelling and thus adds to our knowledge of processes that transport constituents and momentum within the tropical upper troposphere.

Dedication

To my ever supportive parents, Jennifer & Mark and my adorable baby brother, Tristan.

Acknowledgements

”*Good words are more difficult to find than the emerald*.”

- Ptah Hotep, 5th dynasty Egyptian scholar

This thesis is the culmination of many years of investigation and analysis of the EMERALD (Egrett Microphysics Experiment with RAdar, Lidar & Dynamics) campaign. To Professor Jim Whiteway, I am grateful for having been given the opportunity to work with unique data under expert guidance derived from his first-hand, experiential knowledge.

This work could not have been completed without the patience, encouragement and supervision provided by Professor Spiros Pagiatakis and the ongoing mentorship and support of my supervisory committee members, Professors Peter Taylor and Gary Klaassen.

Additionally, I would like to acknowledge the interest and assistance I received from Dean Barbara Crow, Vice-Provost Alice Pitt, Noel Badiou and Karen Swartz.

Finally, I could not have made this journey without my family and friends. In particular, I would like to acknowledge my long standing friend, Ross Baker, Dr. Marianna Shepherd and Dr. Jeff Seabrook for their continued encouragement and enthusiastic support. To my parents and brother, Jennifer, Mark and Tristan, my surrogate sisters and brother, Gilda, Sana, and Ennio, and my godmother, Dr. Vera Bril, you have been my rock and anchor.

Table of Contents

Abstract ..... **ii**

Dedication ..... **iii**

Acknowledgements ..... **iv**

List of Tables ..... **vii**

List of Figures ..... **viii**

Chapter 1: Introduction **1**

Chapter 2: Background **14**

2.1. Atmospheric Structure 14
2.1.1. The Tropopause 15
2.1.2. Stratosphere – Troposphere Exchange (STE) 16

2.2 Atmospheric Properties 18

2.3 Vertical Motions and Atmospheric Stability 19
2.3.1 Potential Temperature 22
2.3.2 Buoyancy Oscillations or Instability 24

2.4 Atmospheric Gravity Waves 26
2.4.1 Internal Propagating and Evanescent Gravity Waves 33
2.4.2 Gravity Wave Momentum Transport 34
2.4.3 Effect of Background Wind 36
2.4.4 Gravity Wave Breaking 38
2.4.5 Measurements of Mountain Wave Breaking 39
2.4.6 Phase relations expected for gravity waves 42

2.5 Rayleigh-Bénard Convection (Rolls) 44
2.5.1 Rankine Vortex 47

2.6 Turbulence 50
2.6.1 The Spectrum of Turbulence 52

Chapter 3: Measurements and Analysis Methods **55**

3.1 The Aircraft and Payload 56

3.2 Airborne Measurements of Wind, Temperature and Pressure 60

3.3 Lidar System 61
3.4 Design of the Experiment 64
3.4.1 Anvil Outflow Geometry and Flight Tracks 66
3.5 Analysis of Wave and Turbulence Fluctuations 72
3.6 Spectral Analysis 74

Chapter 4: Data Analysis and Results 78
4.1 November 23rd, Flight Leg 1: Waves and Rolls across the Outflow 80
4.2 Isolated Waves in Flight Leg 1 84
4.3 General Analysis of Isolated Waves 90
4.4 Extended Waves and Rayleigh-Bénard Convective Rolls in Flight Leg 1 97
4.5 General Analysis of Convective Rolls 99
4.6 Wavelet Analysis of Coherent Structures 103
4.7 Flight Leg 2: Turbulence and Coherent Structures 110
4.8 Spectral Analysis of Turbulence and Coherent Structures in Flight Leg 2 112
4.9 Flight Legs 3 & 4: Dynamical Measurements along the Axis of the Anvil Outflow 121
4.10 Evolution of the Spectrum of Turbulence along the Outflow 129
4.11 Dynamics at the base of the anvil outflow 133
4.12 Mammatus Clouds 141

Chapter 5: Summary and Conclusions 149

References 155

List of Tables

Table 3.1: EMERALD-2 instrument payload (aboard Egrett and King Air). 57

Table 3.2: EMERALD-2 lidar transmitter specifications 64

Table 3.3: Overview of transverse (1, 2) and longitudinal (3,4) flight legs on Nov. 23, 2002..... 70

Table 4.1: Properties of selected transverse flight legs exhibiting distinct isolated wave signatures. 91

Table 4.2: Basic properties in isolated waves encountered during EMERALD 2. 91

Table 4.3: Properties of selected transverse flight legs exhibiting distinct signatures of Rayleigh-Bénard convection (rolls). 99

Table 4.4: Properties of December 2, 2002 flight legs for the EMERALD 2 campaign. 134

Table 4.5: Comparison of observed properties of Mammatus 142

List of Figures

Figure 1.1: Schematic of the Upper Troposphere, Lower Stratosphere (UTLS) region depicting Stratosphere-Troposphere Exchange (STE) of various atmospheric constituents including STE by breaking gravity waves. The dashed green line represents the tropopause, or boundary between the troposphere and the stratosphere. Image copyright 2014, UCAR. 2

Figure 1.2: Area roughly encompassed by the "Maritime Continent." The region includes the archipelagos of Malaysia, Indonesia, New Guinea and the coast of Northern Australia including its outlying islands, the Tiwi Islands. Figure generated from Google Earth. 5

Figure 1. 3: Schematic illustration of the Hadley (meridional) and Walker (zonal, around the equator) circulations copyright the COMET program. 6

Figure 1.4: Deep tropical convection as initiated by anvil convection and cirrus outflow, copyright Robert Simmons. 7

Figure 1.5: Cumulus cloud convective tower with cirrus outflow constitutes the Hector storm. Outflow is in the direction of the mean background wind and is concentrated at the height of the tropopause, ~15 km. 8

Figure 1.6: The Tiwi Islands, Bathurst and Melville island, pictured with Northern Australia's city of Darwin out of which the EMERALD 2 campaign was conducted. Figure courtesy of Australian Geographic. 11

Figure 2.1: Four main atmospheric layers with associated temperature and pressure profiles. Taken from Professor Steven Wofsy, lecture notes, 2006, published online 11

Figure 2.2: Simplified schematic representative of global scale STE taken from Holton et al., 1995. The tropopause is marked by the thick black line. Thin black lines represent isentropes (surfaces of uniform temperature) in ^{o}K. Broad arrows denote global scale circulation processes while wavy arrows denote meridional transport via eddy motions. 17

Figure 2.3: Illustration of gravity wave motion along slanted streamlines. 27

Figure 2.4: Orientation of air motions induced by a gravity wave and the phase and group velocity. Upward group (energy) propagation yields downward phase velocity. Sinusoid represents the particle's displacement. 31

Figure 2.5: Fluctuations in vertical (w) and horizontal (u) wind as a gravity wave approaches the critical level. Figure modified from Nappo, 2002. 38

Figure 2.6: (a) Measurements of vertical wind by the Aberystwyth VHF radar. (b) Spectral width of the radar signal (proportional to turbulence intensity) averaged between 12:30 and 01:00 UTC. (c) Vertical wind measured on the Egrett. Each flight leg is placed at its height relative to the vertical scale in (a). The topographic height below the Egrett track is shown in green at the bottom with the same relative vertical scale as in (a). The coast of Wales is at 4.1^{o} longitude; the position of the Aberystwyth radar is indicated by the vertical dotted line at 4.0^{o} longitude. Crosses in (a) indicate the time and height when the Egrett passed directly above the radar. Taken from Whiteway et al., 2003. 41

Figure 2.7: Phase relations between fluctuation in displacement, wind velocity and potential temperature. Fluctuations in vertical wind velocity are 90 degrees out of phase with fluctuations in potential temperature. 44

Figure 2.8: Numerical simulation of Rayleigh-Bénard convection with three rolls. Blue indicates relatively cool fluid, while red indicates relatively warm fluid. Figure taken from Alexei Stoukov, ENSEEIHT (École nationale supérieure d'électronique, d'électrotechnique, d'informatique, d'hydraulique et des telecommunications.) 45

Figure 2.9: Phase relations for Rayleigh-Bénard convection showing three convective rolls. Fluctuations in vertical velocity are in phase (0^{o} shift) with potential temperature fluctuations..... 46

Figure 2.10: Phase relations for a rankine vortex. 49

Figure 2.11: Turbulent energy spectrum, E(**κ**), associated with range of wavenumbers, **κ**. Taken from Kaimal and Finnigan (1994). Region (A) is where energy is produced, region (B) is the inertial subrange and region (C) is the dissipation range where kinetic energy is lost as heat. The symbols ∧ and η represent the integral length scale of turbulence and the Kolmogorov microscale length, respectively. 53

Figure 3.1: The Egrett aircraft outfitted with the suite of instruments for the EMERALD project to measure wind speed, temperature, pressure, water vapour, ozone, far-IR spectra, aerosol, and cloud particle microphysical properties 56

Figure 3.2: The King Air **(a)** external view, **(b)** internal instrumentation and cabin configuration. 57

Figure 3.3: Hector's anvil outflow as seen from **(a)** the Egrett (altitude 15 km) and **(b)** the King Air (altitude 5 km.)..... 59

Figure 3.4: **(a)** BAT probe mounted on the left wing of the Egrett aircraft, **(b)** Rosemount turbulence probe mounted on the right wing of the Egrett aircraft..... 60

Figure 3.5: (a) Schematic diagram of the lidar employed aboard the King Air for the EMERALD 2 campaign. (b) Lidar system under construction in the lab, (c) lidar system installed on the King Air with upward pointing orientation. 63

Figure 3.6: CPOL radar reflectivity as measured in a vertical scan of Hector's convective tower and cirrus anvil outflow (dark blue, regions between ~0-70km) This scan was taken looking north near Darwin at 6:18 p.m. local time on November 15, 2001. Figure by Peter May of the Australian Bureau of Meteorology (BOM). 66

Figure 3.7: (a) Australian Bureau of Meteorology C-pol radar backscatter contours outlining the convective core at different altitude levels and times for November 23, 2002. (b) Flight tracks of the Egrett (red) and King Air (blue) are shown relative to the regional geography and the direction of the cirrus outflow. 06:00 UTC corresponds to 3:30 p.m. local time. Taken from Cook, 2004. 67

Figure 3.8: Satellite IR imagery from 23 Nov. 2002. **(a)** Early afternoon: developing convection over Tiwi Islands. **(b)** Late afternoon: remnants of convection with cirrus anvil outflow. 69

Figure 3.9: Four flight legs on November 23, 2002. Egrett track in red, King Air track in blue. Taken from Cook, 2004. 70

Figure 3.10: Lidar backscatter contour plot of the anvil base showing flight leg altitude and track taken across the outflow for flight leg 1, oriented westward at approximately 12.7 km, and flight leg 2, oriented eastward at approximately 13.6 km. Outflow direction is out of the page, toward the reader. Solid lines represent the flight leg actively shown in the panel while dotted line shows where the other flight leg in the other direction occurred. Taken from Cook, 2004. 71

Figure 3.11: Contour plot of lidar backscatter contour from the anvil outflow cirrus cloud. Flight leg 3 was directed southward along the axis of the outflow away from the decayed convective core and flight leg 4 was back along the same ground path, toward the north. Solid lines represent the flight leg actively shown in the panel while dotted line shows where the other flight leg in the other direction occurred. Taken from Cook, 2004. 71

Figure 3.12: (a) example of overlapping third order polynomial fit to obtain perturbed quantities, specifically, zonal wind velocity, u'. The solid black line is the original measurements while the red line is the smoothed, composite polynomial background fit. (b) Perturbed zonal wind velocity (u') as calculated from measurements subtracted from the background fit. 73

Figure 3.13: Different time frequency windows utilized in **(a).** a Fourier transform, **(b).** a windowed Fourier transform and **(c).** a wavelet transform. Taken from Lau and Weng, 1995..... 76

Figure 4.1: Example of coherent structures found in cirrus anvil outflow **(a)** isolated waves: the coloured lines represent actual isolated wave measurements in fluctuation in vertical velocity from seven different flight legs conducted over 13 flight days. The black line is the averaged, zero aligned (i.e. to the point of x-axis zero-crossing) signal. **(b)** Rayleigh-Benard convective rolls, **(c)** extended waves, and **(d)** turbulence from flight leg 1, Nov. 23, 2002, designated a7r3_391 where the naming convention is as follows: a = day number (up to a total of 13) r = run number on that day, last three digits = internal distance / time index. 80

Figure 4.2: Contour of lidar backscatter signal showing the cloud base across the cirrus anvil outflow for flight leg 1 (a7r1_391) on 23 Nov. 2002. The red horizontal line shows the Egrett's flight path (at altitude ~12.4 km) and serves as an x-axis for the overlaid display of in situ vertical velocity measurements (white.) Three regions of interest are circled and labelled. 81

Figure 4.3: Perturbation wind velocities & perturbation potential temperature signals with distance along flight track (km) for flight leg 1 (a7r1_391) with three highlighted regions showing coherent structures of interest. Y-axes on left (black) denotes values of perturbation vertical velocity while y-axes in right (red) denote perturbed quantities of theta, u and v, from top to bottom, respectively. 83

Figure 4.4: (a) measurements of vertical wind, potential temperature and horizontal wind for flight leg 1 of the Emerald 2 campaign, November 23, 2002. **(b)** In situ Egrett measurements of vertical wind compared with fluctuations in potential temperature and horizontal wind velocity for breaking gravity wave observed on May 11, 2000 during the Aberystwyth Egrett Experiment. Egrett altitude is ~10.5 km. 85

Figure 4.5: Detail of region 2 (37 km -42 km) of 23 Nov. Flight leg 1 (a7r1_391.) Fluctuations of vertical velocity (black) are over plotted against, from top to bottom, fluctuations in potential temperature, zonal, and meridional wind velocities. 89

Figure 4.6: Fluctuations of vertical velocity (black) are over plotted against, from top to bottom, fluctuations in potential temperature, zonal, and meridional wind velocities for transverse flight leg a2n1_400 on 13 Nov., 2002. 92

Figure 4.7: Fluctuations of vertical velocity (black) are over plotted against, from top to bottom, fluctuations in potential temperature, zonal, and meridional wind velocities for transverse flight leg a5r1_301 on 21 Nov. 2002. 93

Figure 4.8: Fluctuations of vertical velocity (black) are over plotted against, from top to bottom, fluctuations in potential temperature, zonal, and meridional wind velocities for transverse flight leg a6r3_381 on 22 Nov., 2002. 94

Figure 4.9: Fluctuations of vertical velocity (black) are over plotted against, from top to bottom, fluctuations in potential temperature, zonal, and meridional wind velocities for transverse flight leg a6r6_447 on 22 Nov., 2002. 95

Figure 4.10: Fluctuations of vertical velocity (black) are over plotted against, from top to bottom, fluctuations in potential temperature, zonal, and meridional wind velocities for transverse flight leg a7r1_391 on 23 Nov., 2002. 96

Figure 4.11: horizontal wavenumber spectrum from Lane et al, 2001. Red line marks the range in which isolated wave observations fall. The spectrum is normalized with logarithmic contours. Only the largest 1.5 orders of magnitude are shown. Darker contours represent higher spectral power while lighter contours represent lower spectral power. Contours of horizontal phase speed c=5 m/s are also shown..... 97

Figure 4.12: Detail of region 3 (43 km - 57 km) of 23 Nov. Flight leg 1 (a7r1_391.) Fluctuations of vertical velocity (black) are over plotted against, from top to bottom, fluctuations in potential temperature, zonal, and meridional wind velocities. 98

Figure 4.13: Fluctuations of vertical velocity (black) are over plotted against, from top to bottom, fluctuations in potential temperature, zonal, and meridional wind velocities for transverse flight leg a2n1_400 on 13 Nov., 2002. w' and θ' are indicative of rolls (in phase) between 40km – 50km..... 100

Figure 4.14: Fluctuations of vertical velocity (black) are over plotted against, from top to bottom, fluctuations in potential temperature, zonal, and meridional wind velocities for transverse flight leg a2n2_448 on 13 Nov., 2002. w' and θ' are indicative of rolls (in phase) between ~15km – 21km. 101

Figure 4.15: Fluctuations of vertical velocity (black) are over plotted against, from top to bottom, fluctuations in potential temperature, zonal, and meridional wind velocities for transverse flight leg a2n2_448 on 13 Nov., 2002. w' and θ' are indicative of rolls (in phase) between ~25km – 45km. 102

Figure 4.16: Morlet wavelet analysis panel for flight leg 1, Nov 23, 2002. (a) fluctuations in vertical velocity (w') as measured along the flight track. (b) wavelet domain showing the wavelet transform of fluctuation in vertical velocity, (c) cospectral wavelet analysis between w' and θ', and (d) wavelet based phase difference analysis between w' and θ'. 104

Figure 4.17: Demonstration of using wavelet based phase difference contour diagrams to ascertain phase shift between fluctuations in vertical velocity and potential temperature for three cases of isolated waves. Measurements along the flight track are shown on the left while the corresponding phase difference plot is shown on the right. The region at which the phase difference is read is indicated marked by an orange dot, indicated by a large black arrow..... 107

Figure 4.18: Demonstration of using wavelet based phase difference contour diagrams to ascertain phase shift between fluctuations in vertical velocity and potential temperature for three cases of rolls. Measurements along the flight track are shown on the left while the corresponding phase difference plot is shown on the right. The region for which the phase difference is read is indicated by a dashed black box..... 108

Figure 4.19: PSD for flight leg 1. Fluctuations in vertical wind velocity (w') is shown in black while fluctuations in horizontal wind velocity (u') is shown in red. Dashed blue line represents -5/3 slope. 109

Figure 4.20: Lidar backscatter signal contour outlining the anvil cloud's base with superimposed (white) fluctuations in vertical velocity (white) along the Egrett flight track (red). **..**.....109

Figure 4.21: Fluctuations of vertical velocity (black) are over plotted against, from top to bottom, fluctuations in potential temperature, zonal, and meridional wind velocities for transverse flight leg a7r2_420 on 23 Nov., 2002..... 112

Figure 4.22: **(a)** fluctuations in vertical velocity along flight leg 2 (a7r2_420) between 30km-65km. **(b)** wavelet contoured power spectrum. **(c)** w'θ' wavelet contoured cospectrum for region of flight track. **(d)** wavelet based phase difference spectrum for w'θ'. 114

Figure 4.23: **(a)** PSD for vertical (black) and horizontal (red) wind velocity fluctuations. -5/3 slope is denoted by blue dashed line . **(b)** Spectral ratio, SR, of vertical to horizontal PSDs, i.e. PSD[w']/(PSD[u']+PSD[v']). SR = 1 denoted by blue dashed line..... 116

Figure 4.24: **(a)** [top] PSD for vertical (black) and horizontal (red) wind velocity fluctuations for June 6, 2000. [bottom] ratio of vertical to horizontal PSDs for June 6, 2000, **(b)** [top] PSD for vertical (black) and horizontal (red) wind velocity fluctuations for flight leg 2, November 23, 2002. [bottom] SR for flight leg 2, November 23, 2002. 116

Figure 4.25: (a) [top] PSD for vertical (black) and horizontal (red) wind velocity fluctuations for top of cloud on September 19, 2001. Blue dashed line represents -5/3 slope. [bottom] ratio of vertical to horizontal PSDs for top of cloud, **(b)** [top] PSD for vertical (black) and horizontal (red) wind velocity fluctuations for bottom of cloud,

September 19, 2001. [bottom] SR for bottom of cloud where there is greater convection and fall streaks / virga. Blue dashed line represents SR = 1. 118

Figure 4.26: Spectral comparisons of scenarios with differently generated turbulence. **(a)** PSD for fluctuations in vertical velocity **(b)** PSD for fluctuations in horizontal velocity (U'=u'+v'). **(c)** Ratio of PSDs of vertical to horizontal wind fluctuations..... 120

Figure 4.27: Flight leg 3. Egrett flight track shown in red with overlaid vertical velocity fluctuation measurements shown in white. 121

Figure 4.28: Flight leg 4. Egrett flight track shown in red with overlaid vertical velocity fluctuation measurements shown in white. 123

Figure 4.29: Vertical profiles of Richardson number (yellow line is cricitical Richardson number = 0.25), horizontal wind velocity (u = blue, v = green), potential temperature (red = vertical averaging of flight leg data over 100 m) and Root Mean Square (RMS) perturbation vertical velocity (w') used as a proxy for TKE from flight leg 4 on November 23rd. 124

Figure 4.30: horizontal measurements of Richardson number, wind velocity and turbulence kinetic energy along flight leg 3. Zonal wind, u, measurements are in blue while meridional wind, v, measurements are in green. 127

Figure 4.31: horizontal measurements of Richardson number, wind velocity and turbulence kinetic energy along flight leg 4. Zonal wind, u, measurements are in blue while meridional wind, v, measurements are in reen. 128

Figure 4.32: Lidar backscatter contour profile showing the outline of the cloud base as measured flight leg 3, Nov. 23, 2002. The convective core of the storm is located near -11.5 degrees and the end of the outflow occurs just beyond -13.5 degrees. The two regions where horizontal and vertical wind fluctuation PSDs are sampled are approximately located between 60 km – 75 km and 275 km -290 km, respectively. The Egrett flight track is shown in red. 130

Figure 4.33: Lidar backscatter contour profile showing the outline of the cloud base as measured flight leg 4, Nov. 23, 2002. The convective core of the storm is located near -11.5 degrees and the end of the outflow occurs just beyond -13.5 degrees. The two regions where horizontal and vertical wind fluctuation PSDs are sampled are approximately located between 60 km – 75 km and 275 km -290 km, respectively. The Egrett flight track is shown in red. 131

Figure 4.34: Lidar backscatter contour plot outlining anvil base taken in flight leg 3 (Nov. 23, 2002) with overlaid curves for different horizontal averaging periods displaying decreasing SR with increasing distance from the core. 132

Figure 4.35: sample of stepwise flight leg pattern along outflow conducted on December 2, 2002..... 134

Figure 4.36: Lidar backscatter contour plots of flight legs along the anvil base at varying altitudes from December 2, 2002. 1375

Figure 4.37: Lidar backscatter contour plots of flight legs along the anvil base at varying altitudes from December 2, 2002..... 137

Figure 4.38: Vertical profiles of potential temperature, zonal and meridional wind velocities (absolute, i.e. quantities are u, v, w, not u', v', w') and turbulence kinetic energy in the vicinity of the cloud base (located around 8 km.)..... 138

Figure 4.39: Momentum flux in the direction of outflow background wind (u) as calculated for all 11 legs on December 2, 2002. Each point represents momentum calculated over one flight leg from that day. 139

Figure 4.40: Gravity waves propagating upward and downward to the east, away from the cloud base..... 141

Figure 4.41: Close up of mammatus lobe formations from flight leg a13r4_dn on December 2, 2002. 142

Figure 4.42: Fluctuations of vertical velocity (black) are over plotted against, from top to bottom, fluctuations in potential temperature, zonal, and meridional wind velocities for section of Dec. 2 flight leg a13r4_dn showing mammatus like lobes. 144

Figure 4.43: (a) PSD for vertical (black) and horizontal (red) wind velocity fluctuations for mammatus region of leg a13r4_dn. -5/3 slope is denoted by blue dashed line. (b) Ratio of vertical to horizontal PSDs. SR = 1 denoted by dotted blue line..... 145

Figure 4.44: Comparison of measured mammatus spectrum (black) to numerical model of mammatus spectrum at anvil cloud base from Garrett, et al, 2010 (red.) Dashed blue line indicates -5/3 slope. 147

Figure 4.45: Kanak & Straka 2009 numerical simulations for mammatus formation at anvil base for different shear, from left to right, shear values are 0.0030 $s-1$, 0.0035 $s-1$ and 0.0040 $s-1$. 148

Figure 5.1: Schematic overview of where dynamical phenomena were generally observed in the anvil outflow of tropical convection for the total thirteen flight days of the EMERALD-2 experiment, conducted out of Darwin, Australia, Nov-Dec. 2002. Isolated waves tended to be observed at anvil edges & throughout anvil in transverse flight legs while extended, wave-like structures and convective rolls were observed along the length

of the outflow axis. Turbulence was observed along the top (shear generated) and bottom (convectively generated) of the outflow. The coloured shading behind the outflow outline roughly depicts local buoyant conditions with altitude, i.e. stable (red), neutral (green) and unstable (blue). 151

Chapter 1: Introduction

The Upper Troposphere Lower Stratosphere (UTLS) is a complex, dynamic and as yet poorly understood region of Earth's atmosphere. The troposphere is the lowest region of the atmosphere extending from the surface to the tropopause at 10 km –18 km. About 90% of the total atmospheric mass resides in the troposphere (Monks, 2005). It is the layer in which weather occurs. Weather can be defined as short term atmospheric conditions in a certain location as opposed to climate which is a long term average of atmospheric conditions such as temperature, precipitation, humidity and wind velocity.

UTLS processes directly influence both weather and climate by virtue of the fact that such processes occur over a multitude of scales extending through the planetary and synoptic down to microscales associated with turbulent mixing. Within the UTLS, the Tropical Tropopause Layer (TTL) spans altitudes between approximately 13 km to 17 km (Fig. 1.1) depending on latitude. The TTL serves as an interfacial zone through which the compositionally and dynamically varied stratosphere and troposphere exchange constituents, one of these being water vapour.

Water vapour is the most important radiatively active gas (Manabe and Wetherald, 1967; Houghton et al. 1990; Lindzen, 1990) for determining the Earth's climate because it is such a strong absorber in the infrared. Climate is especially sensitive to changes in water vapour content in the upper troposphere (Harries, 1996.) Water absorbs most of the thermal radiation emitted from Earth's surface, but a smaller amount is emitted to

space from the upper troposphere since the temperature there is lower than at the surface thus requiring greater surface temperatures for planetary radiation balance.

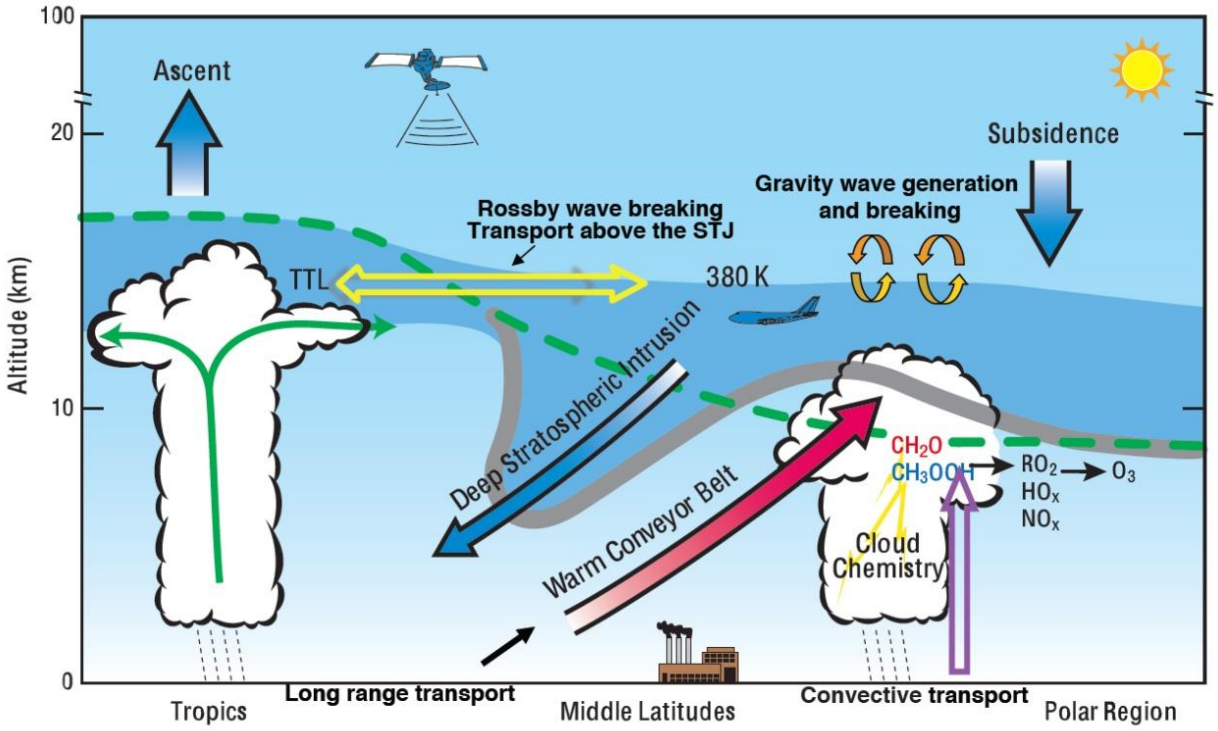

Figure 1.1: Schematic of the Upper Troposphere, Lower Stratosphere (UTLS) region depicting Stratosphere-Troposphere Exchange (STE) of various atmospheric constituents including STE by breaking gravity waves. The dashed green line represents the tropopause, or boundary between the troposphere and the stratosphere. Image copyright 2014, UCAR.

A very important issue in atmospheric science is climate change within the troposphere. The challenge is to predict changes in climate in the coming decades and requires advancement in our knowledge of the transport and phase transformations of water within the upper troposphere. At slightly lower altitudes within the TTL, water vapour descends, radiatively cooling and exerting vast impact on the radiative forcing of climate (Hartmann et al., 2001b). At these lower altitudes, cirrus clouds, generally

characterised by thin and wispy strands at heights typically greater than ~ 6km, act effectively as water reservoirs and temperature regulators (Held and Soden, 2000). It is estimated that as much as 20% - 25% of the Earth's atmosphere is covered by cirrus clouds in the mid latitudes and as much as 70% in the tropics (Liou, 2002). Large thunderstorms can generate a layer of cirrus cloud flowing outward from the thunderstorm's main convective core at the approximate altitude of the tropopause; i.e. approximately 12 km at midlatitudes and approximately 17 km in the tropics.

At altitudes above 15 km, the average solar heating is slightly greater than infrared cooling and the air slowly rises into the stratosphere, while the airflow is mainly horizontal. The minimum temperature encountered determines the amount of humidity in the air that enters the stratosphere. The air then continues to rise into the stratosphere and, while circling the globe, it moves slowly toward the polar regions. This is referred to as the Brewer-Dobson circulation. It was first postulated (Brewer 1949; Dobson, 1956) to explain the dryness of the stratosphere, since it is only above the tropics where air would encounter sufficiently low temperatures in the tropopause (e.g. -80^{o}C) that would correspond to the frost point of stratospheric air.

As air passes through the coldest areas of the tropical tropopause region the relative humidity with respect to ice is maintained at 100%, while the excess humidity is deposited on ice crystals that precipitate. The amount of water vapour in the air corresponds to the saturated vapour pressure at the minimum temperature that was encountered. The air is freeze dried as it rises into the stratosphere. Clouds will later form in this air only when the temperature drops below the minimum at the tropical

tropopause and this occurs only over the polar regions. These polar stratospheric clouds are a key component in the heterogeneous chemistry that causes the depletion of ozone in the polar stratosphere. Thus, the dynamical processes distributing water within the tropical upper troposphere have a key influence stratospheric chemistry in addition to on climate change (Holton, 2004).

The dynamics by which water vapour is introduced into the TTL and the character of turbulence occurring in the TTL are the key focus of this thesis. One of the world's largest, annually occurring "maritime continent" thunderstorms known as "Hector," which occurs over the Australian Tiwi Islands, provides the perfect natural laboratory in which to study such dynamics. Figure 1.2 displays the approximate area commonly referred to as the maritime continent. While not a physical landmass, the maritime continent (Ramage, 1968) is located within the Indo-Pacific warm pool region where sea surface temperatures typically reach higher than 28^{o}C, making the area unique in its capability for en masse heat transport that is tightly related to large-scale variations in Earth's climate (Neal and Slingo, 2003). Convection in this region is initiated by sea breeze circulations over islands comprising the maritime continent and maintained by colliding precipitation gust fronts.

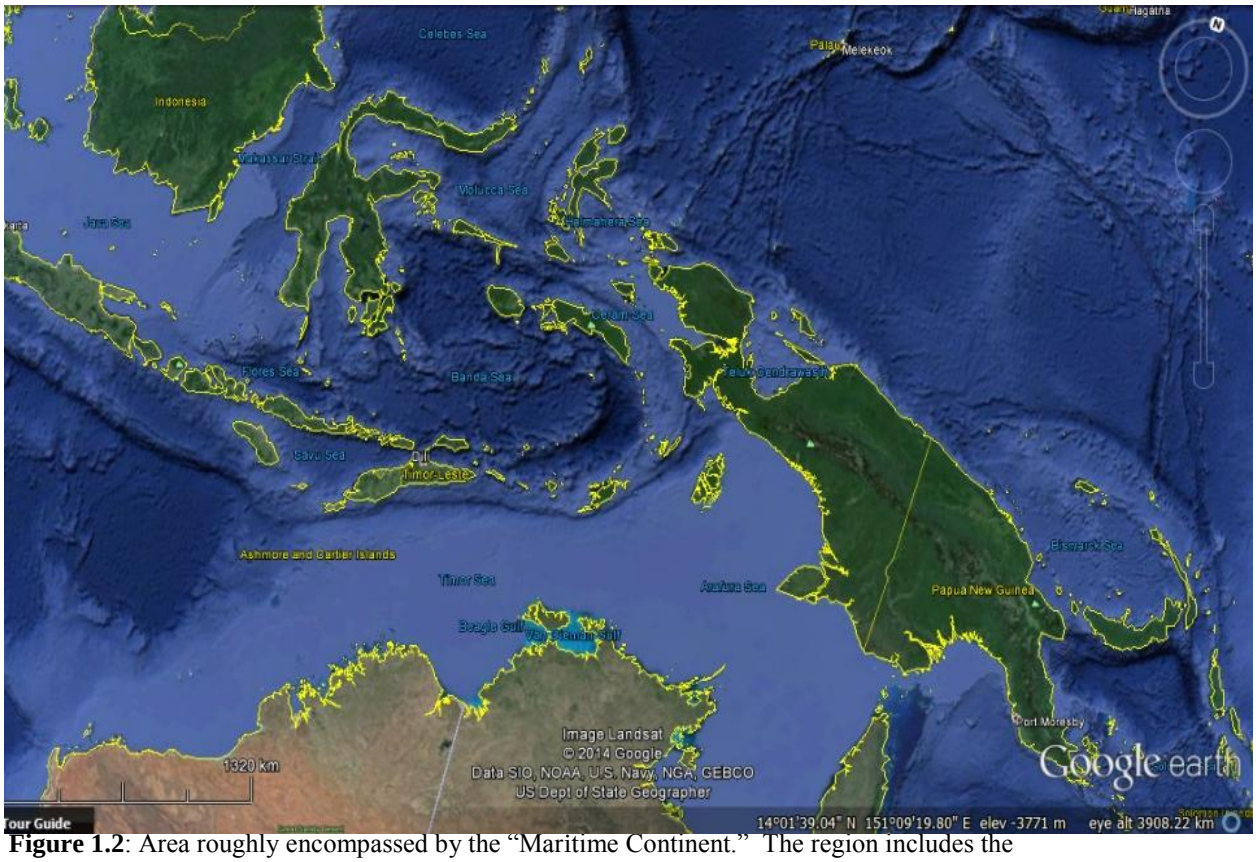

Figure 1.2: Area roughly encompassed by the "Maritime Continent." The region includes the archipelagos of Malaysia, Indonesia, New Guinea and the coast of Northern Australia including its outlying islands, the Tiwi Islands. Figure generated from Google Earth.

Satellite observations have shown that Hector and other extensive, diurnally generated tropical thunderstorms are the primary deep convective (i.e. convection extending up to and sometimes defining the tropopause) mechanism driving the "boiler box" of the tropics and also the Hadley and Walker circulations (Holland and Keenan, 1980) (Figure 1.3). These large storms, or Mesoscale Convective Systems (MCS), can be visually distinguished by the appearance of towering, convectively driven, cumulus cloud pillars.

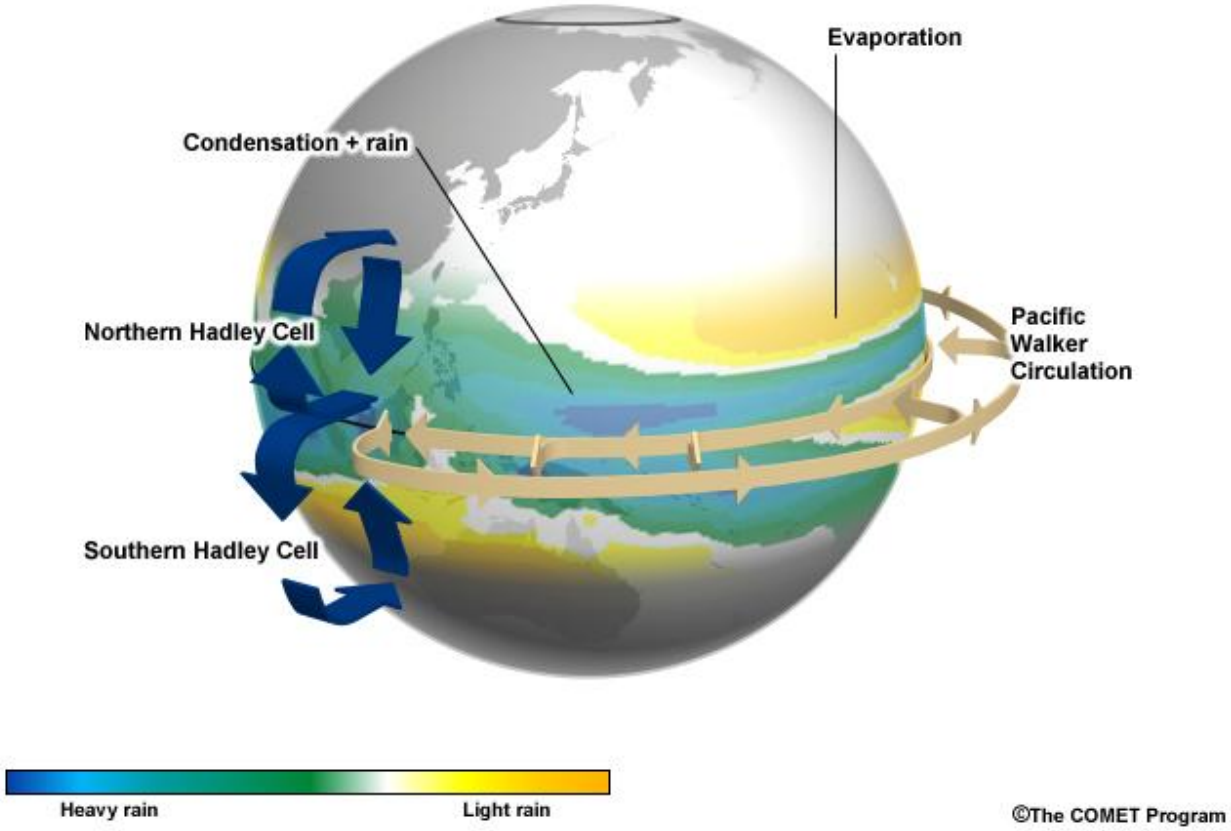

Figure 1.3: Schematic illustration of the Hadley (meridional) and Walker (zonal, around the equator) circulations copyright the COMET program.

The cumulus cloud pillars indicate that there are abundant upward motions of air inside the clouds; the speed of which can reach as much as 600 meters per minute. In as short as ten minutes, a cloud pillar over 6000 meters in height can be formed. These cloud pillars extend to the tropopause and are comprised of ice crystals and water drops. The ice crystals near the top of the cloud are usually dragged by the wind into the shape of an anvil.

Extending hundreds of kilometers outward from the cumulus cloud pillars is an expansive region of cirrus cloud which moves away from the convective core with the background wind, giving the MCS a distinctive, anvil-like appearance as depicted schematically in Fig. 1.4. This anvil shaped cirrus cloud region is referred to as the "anvil outflow" and is the environment in which measurements presented throughout the thesis were taken.

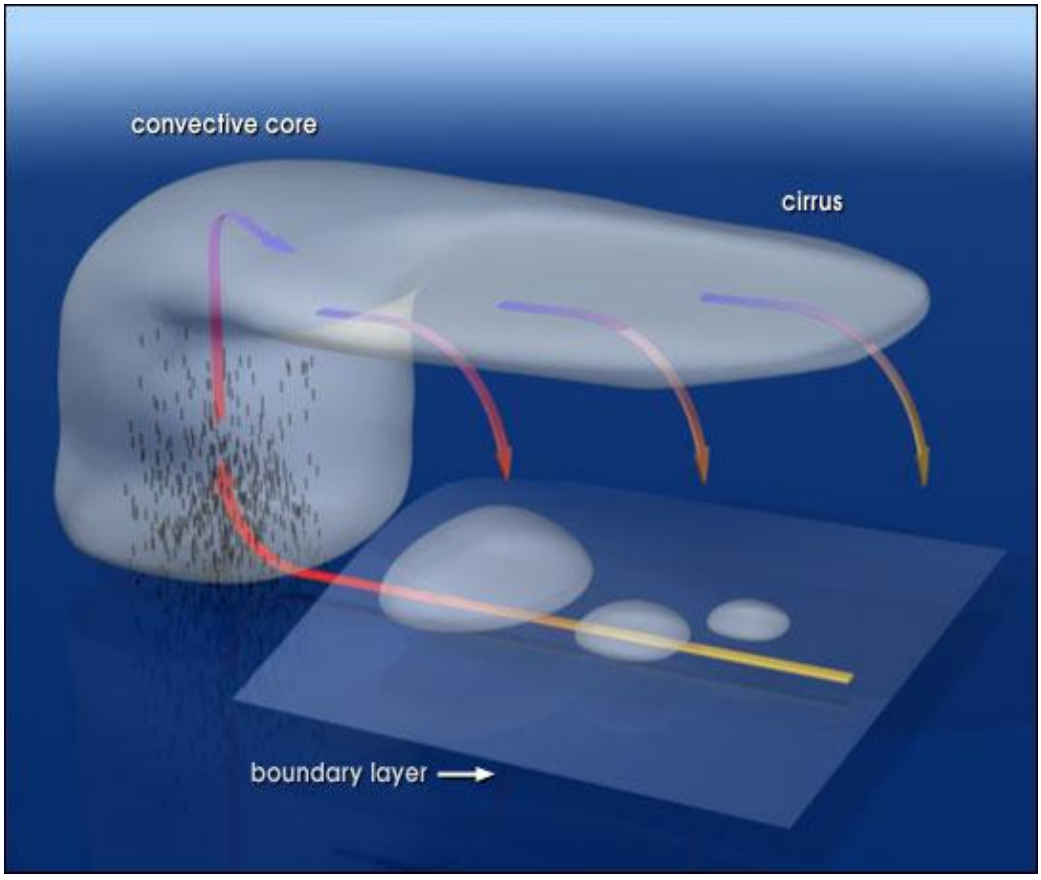

Figure 1.4: Deep tropical convection as initiated by anvil convection and cirrus outflow, copyright Robert Simmons.

Figure 1.5 shows a photo of such convection above the Tiwi Islands, north of Australia. In this case, the tops of the convective towers are known to overshoot into the

stratosphere but much of the anvil shaped outflow resides in the upper troposphere at heights below 15 km. Most of the water is in the form of ice crystals (Whiteway et al., 2004) within cirrus clouds. The cirrus cloud composed outflow can extend hundreds of kilometers away from the convective core. The ice crystals precipitate, sublimate, and humidify the air at lower heights (Held and Soden, 2000).

Figure 1.5: Cumulus cloud convective tower with cirrus outflow constitutes the Hector storm. Outflow is in the direction of the mean background wind and is concentrated at the height of the tropopause, ~15 km.

The research undertaken for this thesis involves the analysis of measurements from the second stage of a two-stage experiment known as EMERALD (Whiteway et al., 2004a).

The EMERALD project, or "Egrett Microphysics Experiment with RAdiation Lidar and Dynamics" was conducted in order to advance understanding of outstanding issues in cirrus cloud dynamics. The first stage of the EMERALD experiment, referred to here as EMERALD-1 was conducted out of Adelaide, Australia in 2001 and involved the study of mid-latitude frontal cirrus cloud systems. The second stage of the experiment, EMERALD-2 was conducted out of Darwin, Australia in 2002 and involved the study of tropical deep convection and dynamics occurring in and around the cirrus outflow region of an anvil cloud. Another campaign with the Egrett aircraft, called the Aberystwyth Egrett Experiment, was carried out in May – June 2000 to study the dynamics and chemistry of the tropopause region over Wales, UK (Whiteway et al., 2003). While this thesis chronicles the data analysis for the EMERALD-2 campaign, examples of unique dynamical measurement scenarios from both EMERALD-1 and the Aberystwyth Egrett Experiment are included in the thesis for comparison purposes.

The EMERALD-2 campaign was conducted from November – December, 2002, out of Australia's capital of its Northern Territory, the city of Darwin, located at 12.45^{o}S, 130.83^{o}E. This location was chosen because of the regularity and depth of the convective system (Fig 1.5) that occurs over the Tiwi Islands, 50 km north of Darwin (Fig. 1.6) during the pre-monsoon period in November and December. Just about every day during November and December, a very substantial mesoscale (100 – 1000 km) convective system (MCS) occurs over the Tiwi Islands while there is no other convection in the surrounding area. The storm is so regular and large that it is well known by the name of Hector as previously mentioned in this Chapter. The EMERALD-2 objectives were to

position the aircraft within the anvil outflow from deep tropical convection for in situ measurements. This is relevant in being the location where water vapour first enters the TTL. Apart from larger scale[1], radiatively forced vertical motions, water vapour is also distributed through smaller scale dynamics within the anvil. This includes the remnant turbulence already in the outflow from Hector's convective cores, the turbulence driven by latent radiative heating/cooling, at the bottom and top of the cloud, wave motions and other coherent structures observed in the cirrus outflow. Flight legs therefore were arranged below, through, and slightly above the outflow in order to obtain measurements of basic meteorological parameters, cloud particle microphysics, radiation in the far infrared, water vapour, and air motions.

Despite regular occurrences of MCS in the maritime continent each year, hazardous flying conditions due to increased turbulence from strong convective instability in the area make it difficult to collect in situ aircraft based data with which to study the dynamics of such storms. Consequently, a limited number of such measurements exist (eg., Steiner, 1966; Lilly and Lester, 1974; Lilly, 1978; Kennedy and Shapiro, 1975; Murrow, 1987; Whiteway et al., 2003; Koch et al., 2005; Lu and Koch, 2008; Wroblewski et al., 2007). In fact, turbulence adversely affecting aviation found to be occurring on 'aircraft scales' of 200 m – 1 km (Lane et al., 2012), as a result of large scale convection, has become a popular recent topic of aviation safety literature and pilots are advised to avoid MCS, such as Hector, by at least 100 km (Lane, media

[1] According to the American Meterological Society, (AMS,) the synoptic scale (also known as large scale or cyclonic scale) is a horizontal length scale of the order of 1000 kilometres (about 620 miles) or more.

communication, Sydney morning Herald, 2012).

Figure 1.6: The Tiwi Islands, Bathurst and Melville island, pictured with Northern Australia's city of Darwin out of which the EMERALD 2 campaign was conducted. Figure courtesy of Australian Geographic.

Even though this thesis analyzes 12 year old data, to present day (to the author's knowledge,) EMERALD-2 is still the only campaign which has returned sufficiently small scale resolution measurements with which to study local instability occurring within the anvil outflow region.

The EMERALD campaign and in particular its second stage, EMERALD-2 were unique in providing high-resolution, small-scale measurements to study instabilities within the anvil outflow. These high-resolution, in-situ measurements are the base for the analysis of the dynamical measurements in the outflow region with turbulence probes installed onboard an aircraft. Employing these data, the thesis focuses on the analysis of

the dynamical measurements in the outflow region with the turbulence probes installed on the Egrett aircraft.

My research involves the characterization of a dynamical system (namely tropical deep convection in the region of MCS cirrus anvil outflow) leading to a better understanding on the role of small-scale dynamical processes, like gravity waves in the TTL and the coupling of the troposphere with the atmosphere above, as well as serve as input to and validation of global circulation models. As such, the motivation of the research is basic knowledge generation that could lead to the facilitation of improved global climate models. The results and conclusions presented in this thesis shed light on the small scale dynamical processes not previously understood or investigated. My research examined wave-like activity observed in measurements and concentrated on ascertaining that gravity waves do, in fact, exist within the outflow along with other wavy, coherent structures such as Rayleigh-Bénard convective rolls.

Further, by comparing turbulence measurements from both the Aberystwyth Egrett Experiment (taken in clear air) and the EMERALD-1 campaign (taken in midlatitude cirrus) to the turbulence measurements taken in the outflow for EMERALD-2, a unique spectral investigation of turbulence generated in different dynamical scenarios is conducted for the first time from in-situ airborne measurements at unprecedented small scale resolution to within 4 meters. This comparison provides means to investigate the unique characteristics of the anvil outflow turbulence. The objective of this comparison was to determine whether anvil outflow turbulence possesses unique characteristics. The end result was that turbulence occurring in the cirrus anvil outflow region of an MCS was

found to display distinctive spectral properties, varying with distance away from the storm's convective core. Closer to the core of main convection, turbulence was observed to be more isotropic (horizontal and vertical motions approximately equipartitioned) while with increasing distance from the storms' convective core along the outflow, turbulence flattened out in a pancake-like manner, displaying a 2d character with air motions being mainly focussed in the horizontal, consistent with Lilly's theory of "stratified turbulence" (see Lilly, 1983).

By way of overview, Chapter 2 presents a short theoretical background on relevant principles and concepts fundamental to understanding experimental results. Chapter 3 provides detailed information on the measurement and analyses methods. Chapter 4 presents the experimental findings on the dynamics of cirrus outflow anvil and the interpretation in terms of three main dynamical phenomena: gravity waves, Rayleigh-Bénard convective rolls, and turbulence. Finally, Chapter 5 summarizes the findings and proposes research questions to be answered by future experimentation.

Chapter 2: Background

2.1. Atmospheric Structure

The Earth's atmosphere is stratified, or layered. Four main atmospheric layers are defined to exist according to the unique temperature gradients displayed in each. From the surface to space, these layers are the troposphere, the stratosphere, the mesosphere and the thermosphere. Depth and vertical temperature structures of each atmospheric layer are illustrated schematically in Figure 2.1.

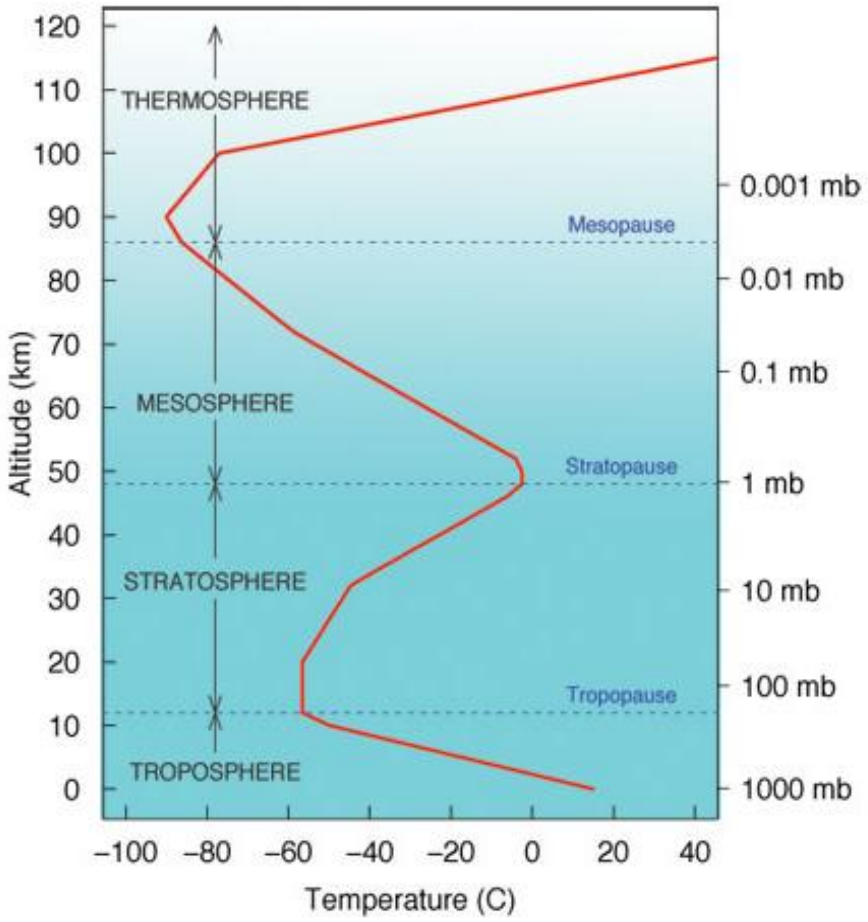

Figure 2.1: Four main atmospheric layers with associated temperature and pressure profiles. Taken from Professor Steven Wofsy, lecture notes, 2006, published online.

Pressure decreases with increasing height from the surface while temperature stratification in each layer is dictated by characteristic radiative and dynamical processes occurring within that layer. This thesis mainly concerns gravity waves and turbulence in the upper troposphere and tropopause region above the tropics.

2.1.1. The Tropopause

The tropopause occurs at heights as low as 8 km at the poles and up to 18 km in the tropics (Hoinka, 1998). At the tropopause, the temperature gradient changes from negative in the troposphere to positive in the stratosphere and can be recognized locally by a temperature minimum. The World Meteorological Association (WMO) specifies the altitude of the tropopause as occurring at the lowest height where the lapse rate (rate of decrease in temperature) decreases to 2°K/km or less (Holton et al., 1995).

The troposphere and stratosphere hold the largest atmospheric concentrations of water and ozone, respectively and the transition region between them, or tropopause, is characterized by a sharp temperature inversion (Birner et al., 2002). Directly below the tropopause, radiative cooling occurs due to emission of infrared radiation by water vapour and cirrus clouds. This cooling diminishes abruptly with height through the tropopause since there is much less water in the stratosphere. The density of ozone increases sharply with height through the tropopause with associated heating by absorption of UV radiation in the lower stratosphere (Gettelman, 2002). Consequently,

there is a tendency to form a sharp temperature inversion (positive gradient) at the tropopause. The main difference between the troposphere and stratosphere lies in the relative stability of each layer.

Atmospheric stability is defined as the ability of an air parcel to resist vertical motion. A stable atmosphere is thus one in which vertical motions are inhibited. Conversely, an unstable atmosphere is defined as an atmosphere in which vertical motions are enhanced. The upper troposphere is nearly unstable, while the lower stratosphere is very stable (Gettelman et al., 2011). Stability and its importance in relation to the UTLS will be discussed in further detail in Section 2.2.

2.1.2. Stratosphere – Troposphere Exchange (STE)

The transport between the troposphere and stratosphere of such constituents as water vapour, ozone, radiatively active aerosols, urban pollutants, and products of biomass burning is of great importance to atmospheric chemistry and climate (Folkins et al., 1997; Fueglistaler et al., 2009). For instance, the transfer of anthropogenic pollutants from the troposphere to the stratosphere plays a vital role in the chemistry of ozone depletion (Solomon, 1999).

On global scales, STE is governed by the Brewer-Dobson circulation. The Brewer Dobson circulatory process can be likened to an extra-tropical pump which acts to move air en masse upward and poleward, away from the equator and down toward the poles (Fig. 2.2). This thesis concentrates on the smaller scale processes within the Tropical

Tropopause Layer (TTL). Consequently, further discussion of global scale transport mechanisms is not pursued here.

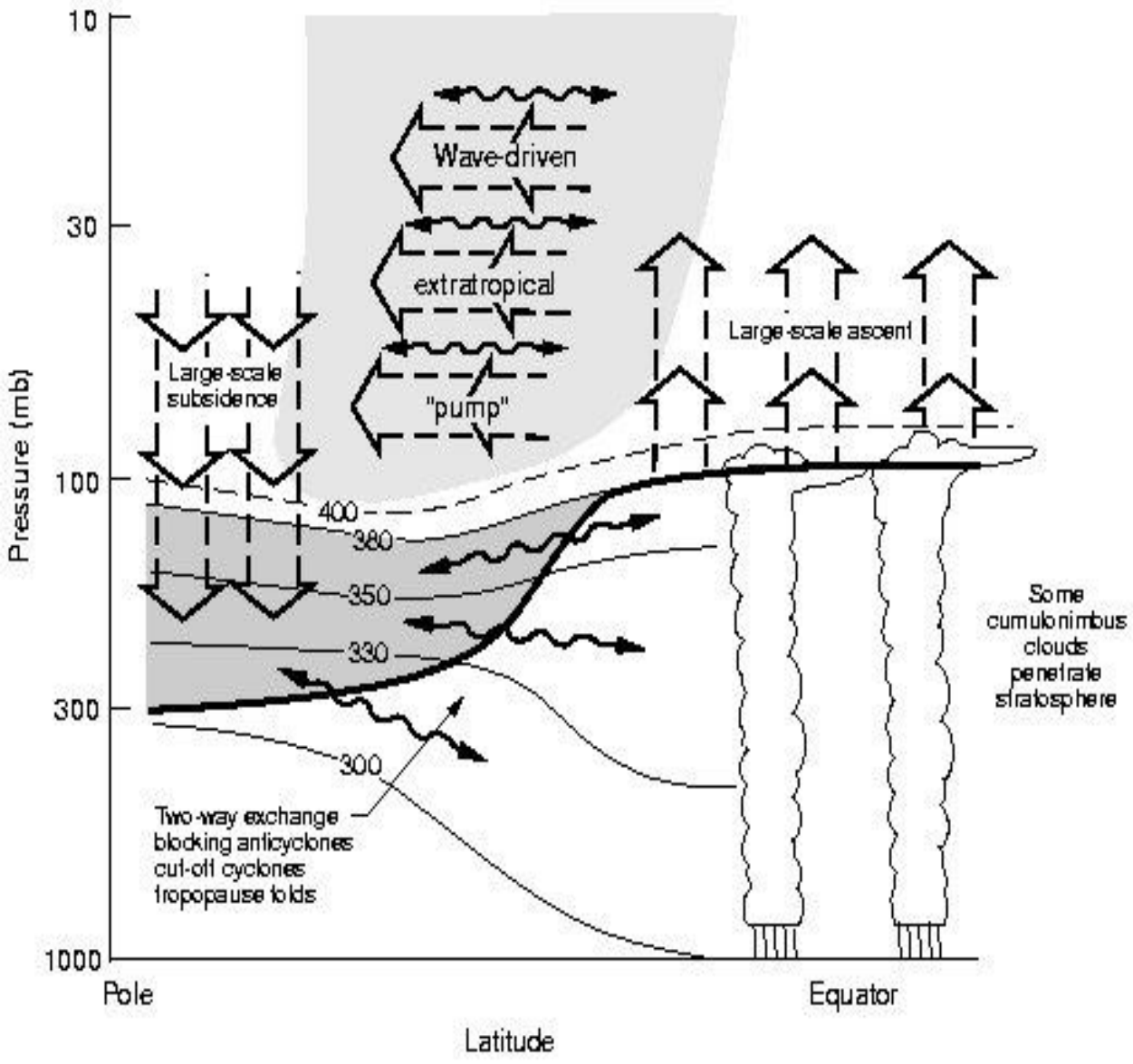

Figure 2.2: Simplified schematic representative of global scale STE taken from Holton et al., 1995. The tropopause is marked by the thick black line. Thin black lines represent isentropes (surfaces of uniform temperature) in ^{o}K. Broad arrows denote global scale circulation processes while wavy arrows denote meridional transport via eddy motions.

2.2 Atmospheric Properties

The most basic properties of any planetary atmosphere are pressure, density, and temperature. These are related by the ideal gas law which states

$$p = \rho RT \,, \tag{2.1}$$

where p, ρ, T represent pressure, density and temperature, respectively and R is the ideal gas constant which is 287.058 J/(kg•K) for dry air.

The force of gravity causes pressure to decrease with height. When there is balance between the downward force of gravity and the upward pressure gradient force, the change in pressure with height is given by the hydrostatic equation

$$\frac{\partial p}{\partial z} = -g\rho \,, \tag{2.2}$$

where g = 9.81 m/s² is the acceleration due to gravity. Combining the ideal gas law and the hydrostatic equation, the barometric equation provides pressure as a function of height

$$p(z) = p_0 e^{-\frac{z}{H}} \,. \tag{2.3}$$

Where H = RT/g is referred to as the scale height. It is the vertical distance required for atmospheric pressure to decrease by a factor of e=2.71828 (base of natural logarithm).

The next basic property of an atmosphere pertains to the buoyant stability of the air. Air stability depends on temperature gradient and has a strong influence on the character of the dynamical motions (Atticks and Robinson, 1983). The atmospheric layers presented in Fig. 2.1 can be characterized in terms of stability. The transfer of infrared radiation from the surface of a planet and through the atmosphere will result in temperature decreasing with height with a gradient that is unstable due to buoyancy where density increases with height (Lindzen, Chou, and Hou, 2001). This instability is removed when convection occurs and heat is transported upward. At the top of the troposphere, the air temperature would become constant with height in the absence of other heating or cooling mechanisms. For Earth, the temperature increases in a region above the troposphere due to the absorption of solar radiation by the ozone molecule (Crutzen, 1974; Folkins et al., 2005). The increasing temperature results in a strong force of buoyancy which resists vertical motion such that the air becomes stratified, hence the term "stratosphere." Above the stratosphere at altitudes greater than 50 km, the effect of ozone is less prominent and the temperature decreases with height through the mesosphere. At heights above 80 km, solar radiation absorption by molecular oxygen is significant and temperature increases with height through the thermosphere (Sahai et al., 2012).

2.3 Vertical Motions and Atmospheric Stability

When a parcel of dry air rises and expands, the work done against the surroundings is drawn from the internal kinetic energy of the molecules such that the

temperature decreases with height . As dry air ascends adiabatically (i.e. with no heat being added to or removed from the system), the temperature will decrease at the dry adiabatic lapse rate

$$\Gamma_d = \frac{dT}{dz} = \frac{g}{c_p}, \tag{2.4}$$

where c_p represents the specific heat capacity of dry air at temperature, *T*, eg. at *T* = 300°K, c_p = 1005 J/kg•K . The dry adiabatic lapse rate is approximately 9.8°K/km in the troposphere.

This is very important for considerations of buoyant stability (Alexander, Tsuda and Furumoto, 2008; Hartmann et al., 2001a; Folkins, 2002). For example, if the temperature of the background environment is decreasing at a rate of less than g/c_p, then an air parcel that is displaced upward will have a lower temperature than its surroundings and the force of buoyancy will be directed back toward the original position. If, however, the background temperature decreases at a rate of greater than g/c_p, an air parcel displaced upward will have a temperature that is warmer than its surroundings. The force of buoyancy will be directed upward, away from the original position, and the parcel will continue to rise. Thus, the atmosphere is unstable to vertical motions where the rate of decrease in temperature with height is greater than g/c_p. This is known as convective instability (Ludlam and Scorer, 1953).

The more typical scenario in the troposphere is that the air contains water vapour which leads to significant consequences (Folkins and Martin, 2005; Gettelman et al., 2002a). When air rises and cools adiabatically, it may reach a point where the water vapour pressure equals the saturated vapour pressure (relative humidity = 100%) and the water vapour within the air condenses into cloud droplets. Latent heat is released when water condenses, adding thermal energy locally. Consequently, the process is not strictly adiabatic. The rate of change of temperature with height for air that is saturated with respect to water is referred to as the saturated or wet adiabatic lapse rate and is given by,

$$\Gamma_s = \frac{dT}{dz} = \frac{\Gamma_d}{1+\left(\frac{L}{c_p}\right)\left(\frac{dw_s}{dT}\right)}, \tag{2.5}$$

where L is the latent heat of condensation and w_s is the saturation mixing ratio, or maximum amount of water that air can hold at a specified temperature and pressure.

The wet adiabatic lapse rate can be as small as $4\,^{\circ}\mathrm{K}$ / km in the tropics but is typically (6 – 7) $^{\circ}\mathrm{K}$ / km. Within a cloud where the air can be assumed to be saturated, the wet adiabatic lapse rate is more relevant for considerations of stability. Cloudy air, therefore can be considered unstable when the background lapse rate is greater than the wet adiabatic lapse rate.

For much of the measurements presented in this thesis, the environment was the thick anvil outflow cloud where the wet adiabatic lapse rate would be more applicable than the dry adiabatic lapse rate. In the area of interest to this thesis within the tropical

upper troposphere, temperatures range from approximately -50°C to -70°C. This corresponds to wet adiabatic lapse rates of (8.5 – 5.5)°K / km.

2.3.1 Potential Temperature

When considering atmospheric dynamics, it is useful to have parameters that are conserved, remaining unchanged with vertical motions. The most basic conserved thermodynamic parameter is potential temperature. Potential temperature, denoted θ, is the temperature that an air parcel would have if compressed adiabatically from its original pressure and temperature to mean sea level pressure (approximately equivalent to 101.325 kPa). It is given by the equation,

$$\theta = T\left(\frac{p_0}{p}\right)^{\frac{R}{c_p}} \tag{2.6}$$

where T is temperature (°K), R is the ideal gas constant for dry air valued at 287.058 (J / kg•K), p_0 is the reference pressure taken at standard mean sea level, and p is the pressure at the altitude of interest.

As previously stated, potential temperature is a conserved quantity for adiabatic motions. The dry adiabatic lapse rate described above corresponds to potential temperature that is constant with height. Thus, the atmosphere is unstable to vertical motion when the potential temperature is decreasing with height and stable when the

potential temperature is increasing with height. Turbulent mixing will act to eliminate gradients in conserved quantities. A well mixed layer will therefore have constant potential temperature, i.e. zero vertical gradient. Within a cloud where the air is saturated, the cooling due to upward motion will result in condensation or deposition of water vapour onto droplets or ice crystals and the process is not adiabatic due to the release of latent heat. The opposite occurs for downward vertical motion. In this case the potential temperature is not conserved.

Within a cloud, the relevant conserved parameter is the equivalent potential temperature. This is the potential temperature of a parcel of air after all of the moisture within it is condensed out and the latent heat released. Equivalent potential temperature can be expressed as

$$\theta_e = \theta \exp\left(\frac{L w_s}{c_p T}\right), \tag{2.7}$$

where L, w_s are as previously defined. The criterion for instability is then that the vertical gradient of equivalent potential temperature is negative for unstable air and positive for stable air. Within a thick anvil outflow cloud where there is intense turbulent mixing, it can be expected that the equivalent potential temperature will be approximately constant with height.

2.3.2 Buoyancy Oscillations or Instability

The vertical acceleration of a displaced parcel of air balanced by the buoyancy force can be written as

$$\frac{d^2(\partial z)}{dt^2} = -N^2(\partial z), \tag{2.8}$$

where

$$N^2 = \frac{g}{\theta}\frac{d\theta}{dz} = \frac{g}{T}\left(\frac{dT}{dz} + \frac{g}{c_p}\right). \tag{2.9}$$

N is called the Brunt-Väisälä frequency, or buoyancy frequency, and is the frequency at which an air parcel will oscillate vertically about its equilibrium in stable conditions. The general solution is of the form

$$(\partial z) \propto \exp(iNt). \tag{2.10}$$

The value of N^2 reveals static stability conditions of the local environment. Specifically, an environment can be characterized as either convectively stable, unstable or neutral. In an environment that is stable, the force of buoyancy is directed toward the equilibrium position and this occurs when

$$N^2 > 0, \left\{ \frac{d\theta}{dz} > 0, \left\{ \frac{dT}{dz} > \frac{-g}{c_p} \right. \right. . \tag{2.11}$$

For the case in which N^2 is positive, the environmental lapse rate is less than the dry adiabatic lapse rate. A parcel of air in such an environment will resist vertical motion and consequently, the environment is said to be stable. Equation 2.10 then represents sinusoidal oscillations.

A neutral environment in which an air parcel will tend to stay at the level where it is displaced occurs when

$$N^2 = 0, \left\{ \frac{d\theta}{dz} = 0, \left\{ \frac{dT}{dz} = \frac{-g}{c_p} \right. \right. . \tag{2.12}$$

In an environment that is convectively unstable (i.e. a rising air parcel continues to rise unimpeded,) the buoyancy frequency will be negative such that

$$N^2 < 0, \left\{ \frac{d\theta}{dz} < 0, \left\{ \frac{dT}{dz} < \frac{-g}{c_p} \right. \right. . \tag{2.13}$$

In this case, the argument of the exponential in equation. 2.10 is a real number, and the vertical displacement grows exponentially.

2.4 Atmospheric Gravity Waves

Atmospheric gravity waves can be visualized by imagining ripples in a pond formed by the dropping of a stone. In the case of the atmosphere, air is the fluid through which wave motions propagate. These atmospheric waves are known as "gravity waves" as they only form in stably stratified air where buoyancy serves as the restoring force (Hines, 1960; Nappo, 2002). Unlike water waves which can be visually observed, gravity waves propagate through transparent air and cannot, in themselves be 'seen' except in some cases of saturated air where temperature variations are large enough to induce condensation, effectively demarcating gravity waves through clouds. Though optically invisible, much like ripples in water, gravity waves exhibit a wide range of behaviours including but by no means limited to partial reflection (eg. Sato et al., 2012), transmission (eg. Dunkerton and Butchart, 1984), and propagation along curved trajectories (see Equation 2.10.) Experimentally, gravity waves are detectable by fluctuations in field variables, such as vertical velocity, temperature and turbulent kinetic energy (Fritts and Alexander, 1989; Fritts and Vincent, 1987; Klostermeyer and Ruster, 1984). As the definition of gravity waves can be taken to mean buoyancy driven oscillations, the variation of scales at which gravity waves can occur or at the very least affect, is vast, virtually stretching from the micrometeorological to the synoptic. For this particular study gravity wave scales involve wavelengths of approximately (2 – 5) km.

The intention of this section is to introduce the properties of atmospheric gravity waves which will inform the analysis and interpretation of measurements reported in

Chapter 4. Many textbooks (e.g. Beer, 1975; Gill, 1982; Holton, 2004; Nappo, 2002) contain derivations of gravity wave properties from first principles and the equations of motion. These derivations are not repeated here. Instead the reader is presented with the author's heuristic derivation of basic gravity wave properties that are relevant to the analysis and interpretations in Chapter 4. The gravity wave equations presented herein are derived for a two-dimensional, irrotational case with constant background wind in the u direction. Wave phase speed is relative to the background wind, or, assuming zero background wind in a reference frame stationary to the ground.

Gravity waves involve motions along streamlines that are slanted from the vertical as depicted in Figure 2.3.

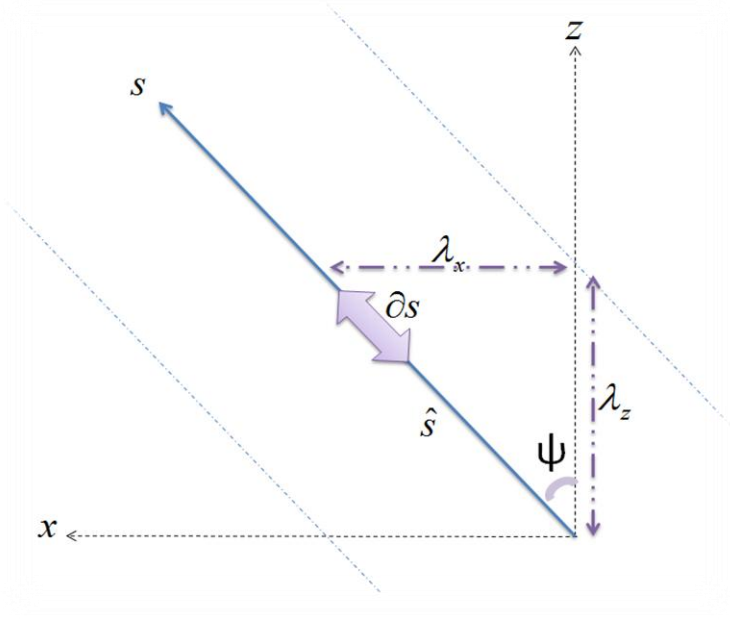

Figure 2.3: Illustration of gravity wave motion along slanted streamlines.

The perturbations in wind , u', v', w' denoting zonal (positive east, negative west), meridional (positive north, negative south) and vertical (positive up, negative down) wind components and temperature (θ') for a two dimensional gravity wave can be written as a complex exponential of the form

$$u', v', w', \theta' = Ae^{i(kx+mz-\omega t)} \tag{2.14}$$

where k and m represent the wave's horizontal and vertical wave numbers, $\frac{2\pi}{\lambda}$, with λ representing wavelength.

The properties of gravity waves can be derived from a solution to the equations of motion and this can be found in standard text books (eg. pages 257-260 of Gill (1982) as previously stated. A heuristic derivation of the gravity wave properties will be provided here that is helpful in visualizing the wave motions. Consider the actual parcel motions induced by the wave along lines of constant phase which are oriented transverse to the direction of wave propagation (as depicted by the vector $\hat{s}$ in Fig. 2.3.) The component of the buoyancy force on the parcel directed back along the path of motion, i.e. back along the $\hat{s}$ direction, can be written:

$$-N^2 \cos\psi(\delta z) = N^2 \cos^2\psi(\partial s)\,. \tag{2.15}$$

The resultant frequency of oscillation back along the tilted streamline is therefore

$$\omega = N \cos\psi \,. \tag{2.16}$$

Expressing the tilt angle, ψ (see Fig. 2.3) in terms of horizontal and vertical wavelength components *k* and *m*, respectively,

$$\cos\psi = \frac{\lambda_z}{\sqrt{\lambda_x{}^2 + \lambda_z{}^2}} = \frac{k}{\sqrt{k^2 + m^2}} \,. \tag{2.17}$$

Substituting Equation (2.17) into Equation (2.16), the dispersion relation is

$$\omega^2 = \frac{N^2 k^2}{k^2 + m^2} \,. \tag{2.18}$$

In the case of internal gravity waves (i.e. gravity waves propagating within a fluid, in this case the atmosphere, as opposed to surface waves. See Stull, 1976) which are most relevant to this thesis, the horizontal phase velocity, or the velocity at which phase fronts propagate is

$$c_{p_x} = \frac{\omega}{k} = \frac{N}{\sqrt{k^2 + m^2}} \,, \tag{2.19}$$

and energy propagates horizontally at

$$c_{g_x} = \frac{\partial \omega}{\partial k} = \frac{\omega m^2}{k(k^2 + m^2)}. \tag{2.20}$$

This demonstrates that the horizontal phase and group velocities are in the same direction. Examining the orientation of the vertical phase and group velocities, the vertical phase velocity can be written

$$c_{p_z} = \frac{\omega}{m} = \frac{Nk}{m\sqrt{(k^2 + m^2)}}, \tag{2.21}$$

while the vertical group velocity can be written

$$c_{g_z} = \frac{\partial \omega}{\partial m} = -\frac{\omega m}{(k^2 + m^2)}, \tag{2.22}$$

demonstrating that the vertical phase velocity and group velocity are directed oppositely, i.e. $c_{g_z} = -c_{p_z}$, meaning that upward energy propagation is associated with downward phase velocity and vice versa. This is illustrated in Fig. 2.4.

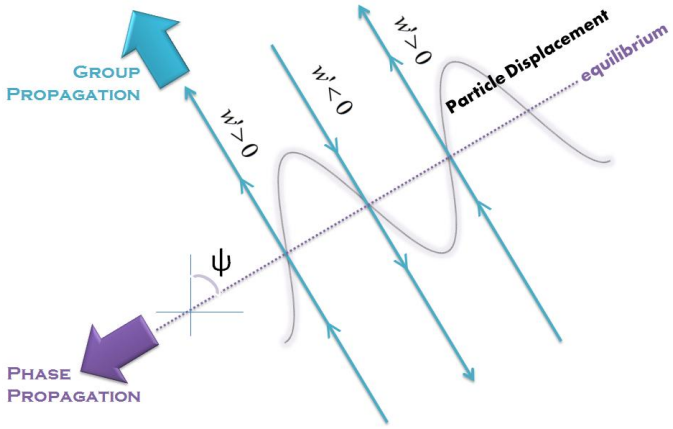

Figure 2.4: Orientation of air motions induced by a gravity wave and the phase and group velocity. Upward group (energy) propagation yields downward phase velocity. Sinusoid represents the particle's displacement.

The direction of propagation is determined by the combination of the signs of the horizontal wavenumbers, *k*, with the vertical wavenumbers, *m*. Recalling for zonal, meridional and vertical components, east, north and up constitute positive while west, south and down constitute negative quantities respectively, group propagation in the four quadrants are defined as follows,

- Up and west: $m > 0,\ k < 0$
- Up and east: $m > 0,\ k > 0$
- Down and west: $m < 0,\ k < 0$
- Down and east: $m < 0,\ k > 0$

Phase velocity and group velocity vectors are orthogonal, such that group velocity is directed along phase lines perpendicular to the wave vector and phase velocity is parallel to the wave vector. Thus, as the phase lines tilt toward the vertical, $\psi \to 90^{\circ}$, the vertical wavelength approaches infinity, *m* approaches 0. Phase propagation occurs horizontally with an oscillation frequency approaching the Brunt-Väisälä frequency, while the group propagation speed is zero. For simplicity, derivations presented here are two dimensional, i.e. in the vertical direction (w) and direction of the background wind flow (u).

Applying the continuity equation for incompressible flow,

$$\nabla \bullet \bar{u}' = 0 . \tag{2.23}$$

Alternately,

$$\frac{\partial u'}{\partial x} + \frac{\partial w'}{\partial z} = 0 . \tag{2.24}$$

Substituting the wave solutions for Equation (2.10),

$$iku' + imw' = 0 . \tag{2.25}$$

This provides a relationship between perturbation velocities and wavenumbers (or wavelengths) as

$$- \frac{w'}{u'} = \frac{k}{m} . \tag{2.26}$$

Depending on the relative signs of k and m, the horizontal and vertical perturbation velocities can be either in phase or 180^o out of phase.

One important property that will be used later in the analysis section is the relationship between the frequency and the relative amplitudes of the horizontal and vertical wind perturbations. The ratio of vertical fluctuation velocity to horizontal fluctuation velocity and the dispersion relation (Equations (2.26), (2.18)) can be used to estimate the frequency of the waves relative to the buoyancy frequency. For example, if $w' = u'$, then $k = m$, and,

$$\frac{\omega}{N} = \frac{k}{\sqrt{k^2 + m^2}} = \frac{1}{\sqrt{2}}. \tag{2.27}$$

2.4.1 Internal Propagating and Evanescent Gravity Waves

The dispersion relation (Equation (2.18)) can be further analyzed in order to determine which frequencies are capable of propagating vertically. Writing vertical wavenumber, m, as follows

$$m = \pm k\left(\frac{N^2}{\omega^2} - 1\right)^{\frac{1}{2}}, \tag{2.28}$$

it is evident that if $\omega < N$, m is a real number and solutions are of form,

$$e^{\pm imz} e^{i(kx-\omega t)}. \tag{2.29}$$

Conversely, if $\omega > N$, m is imaginary. Solutions assume the form

$$Ae^{-mz} e^{i(kx-\omega t)}, \tag{2.30}$$

in which e^{-mz}, will decay exponentially with height. Such waves, therefore, do not propagate vertically. These waves are known as evanescent waves (see, for example, Snively and Pasko, 2008) and propagate only horizontally.

With the vertical wavenumber being imaginary while the horizontal wavenumber is real, Equation (2.26) indicates that the there will be a phase shift of 90° between the horizontal and vertical perturbation velocities for an evanescent wave.

2.4.2 Gravity Wave Momentum Transport

Gravity waves transport momentum and they consequently exert a force on the mean flow in the location where the gravity waves are dissipated (Bretherton, 1969; Dunkerton, 1987; Hines, 1972; Lilly, 1972). While gravity waves do not possess momentum per se, momentum transport is achieved by fluctuations at the leading edge of the wave packet removing momentum from the background flow. The removed momentum is replaced with the fluctuations on the trailing edge of the wave packet, hence a dissipating wave will deposit less momentum back into the flow. In this way,

gravity waves transport momentum from the region of their generation to the region of their dissipation.

A quantity known as "wave stress" describes the vertical flux of horizontal momentum in a gravity wave system and for the 2d case is given by

$$\tau(z) = -\rho_0(\overline{u'w'}), \tag{2.31}$$

where ρ_0 represents mean atmospheric density at height *z* and the term $\overline{u'w'}$ is the vertical flux of eastward momentum, i.e. $\overline{u'w'} < 0$ refers to upward transport of westward momentum, whereas $\overline{u'w'} > 0$ refers to upward transport of eastward momentum. A vertical gradient in the quantity τ will therefore result in a momentum exchange with the mean flow in the form of either an acceleration or drag force. For instance, a dissipating wave with $\left|\frac{d\tau}{dz}\right| < 0$ will manifest as a drag on the mean flow such that

$$\frac{F_D}{\rho_0} = \frac{du_0}{dt} = -\frac{1}{\rho_0}\left(\frac{\partial \rho_0 \overline{u'w'}}{\partial z}\right). \tag{2.32}$$

In the case of non-dissipative propagation, $\tau(z)$ remains constant, requiring *u'* and *w'* amplitudes to increase with height in response to the decreasing atmospheric density.

2.4.3 Effect of Background Wind

Waves travelling through a moving fluid possess both intrinsic and apparent frequency. For gravity waves propagating through a constant background wind, the apparent frequency, ω (as measured from a stationary observer fixed at the ground) will be Doppler shifted from the intrinsic frequency, Ω (as measured within the background fluid flow), such that

$$\omega = \Omega \pm \vec{u} \bullet \vec{k}. \tag{2.33}$$

The apparent phase speed is then

$$c_x = \frac{\omega}{k} = \frac{\Omega}{k} + u_0. \tag{2.34}$$

Equation (2.33) can also be expressed

$$\Omega = \omega - u_0 k = k(c - u_0). \tag{2.35}$$

Recalling Equation (2.18), for ($m << k$) and ($0 << \Omega << N$), the dispersion relation then becomes

$$\Omega^2 = \frac{N^2 k^2}{k^2 + m^2} \approx N^2 \frac{k^2}{m^2}.. \tag{2.36}$$

Rewriting Equation (2.36) in the form of Equation (2.35);

$$\omega - ku_0 \approx N\frac{k}{m}. \tag{2.37}$$

Equation (2.37) affords a direct association of background wind speed to vertical wave number, explicitly,

$$m = \frac{N}{(c-u_0)}. \tag{2.38}$$

The associated vertical wavelength is therefore

$$\lambda_z = (c-u_0)\tau_{BV}, \tag{2.39}$$

where u_0 is the component of background horizontal wind velocity in the direction of wave propagation and τ_{BV} is the Brunt-Väisälä period.

At UTLS altitudes discussed in this thesis, wind speed and direction change significantly with height (see Tsuda et al, 2004). A gravity wave may reach a critical height z_c, where the background wind speed is equal to the wave phase speed (Fig. 2.5). From Equation (2.39), the vertical wavelength approaches zero as the wave approaches the critical level. For a given amplitude, the wave induced gradients in wind and temperature are greater for smaller wavelengths. Thus, at some point below the critical level, the wave will induce unstable wind or temperature gradients and turbulence and mixing will result (Dörnbrack, 1998). The wave energy will be transformed, or

dissipated into turbulence. This is commonly referred to as wave breaking in analogy to waves breaking on a beach.

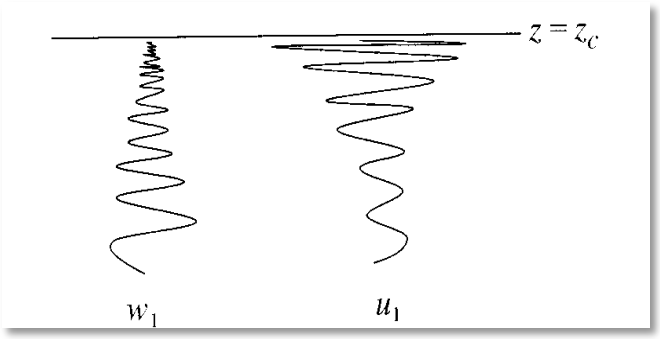

Figure 2.5: Fluctuations in vertical (w) and horizontal (u) wind as a gravity wave approaches the critical level. Figure modified from Nappo, 2002.

2.4.4 Gravity Wave Breaking

A wave may break and generate turbulence either by causing convective instability or by causing shear instability (Hines, 1988; Holton, 1983). The case of wave breaking by convective instability is more likely for the relatively high frequency gravity waves that are the subject of this thesis. Convective instability occurs where the wave lifts more dense air above less dense air. Thus the analogy to an overturning water wave.

From the basic wave geometry and Equation (2.26), the vertical perturbation velocity is in phase with the horizontal perturbation velocity for an internal gravity wave. The air lifted up will also be pushed forward. At large amplitude the wave steepens as the upward displaced air is advected above the downward displaced air. If the horizontal perturbation velocity is greater than the wave phase speed, then the wave crests will be advected over the troughs. In this situation, more dense air is advected over less dense air.

A positive vertical gradient in density is equivalent to a negative vertical gradient in potential temperature, the criterion for convective instability. Thus the criterion for wave breaking is,

$$u' > c - u_0 . \tag{2.40}$$

2.4.5 Measurements of Mountain Wave Breaking

It is illustrative to introduce previous measurements of gravity waves with the Egrett aircraft that will be used later for comparison with the measurements in the anvil outflow. During May/June 2000, the Egrett aircraft was flown out of Boscombe Down, England for flights to investigate gravity waves generated by the mountains of Wales. The flight on 11 May 2000 provided a case study of gravity wave breaking (Whiteway et al., 2003).

Air flowing over mountains is displaced upward and downward and this results in buoyancy oscillations in the form of either vertically propagating internal waves or trapped evanescent waves. Being anchored to the mountains, these waves are stationary with respect to the ground. The frequency relative to the ground is $\omega = 0$ ($c = 0$), and from Equation (2.35), the intrinsic phase speed of the wave is equal to the background wind speed

$$\frac{\Omega}{k} = -u_0 . \tag{2.41}$$

The wave will propagate upwind at a phase velocity equal in magnitude but opposite in direction to that of the background horizontal wind. The dispersion relation given by Equation (2.36) can then be written as

$$m^2 = \frac{N^2}{u_0^2} - k^2. \tag{2.42}$$

The required condition for vertically propagating waves ($m^2 > 0$) is $N > u_o k$. The frequency of oscillations forced by flow over terrain must be less than the Brunt Väisälä frequency. This is also equivalent to

$$\lambda_x > u_0 \tau_{BV} \tag{2.43}$$

The mountain ridges with scale larger than $u_0 \tau_{BV}$ will generate vertically propagating waves, whereas more sharply defined topographic features will only generate vertically decaying waves.

On 11 May 2000, such vertically propagating waves were generated by westward flow over the Welsh mountains. Figure 2.6 shows the measurements of vertical wind by the Aberystwyth VHF radar (near the coast of Wales) and also the in situ measurements from the Egrett aircraft over a series of east-west flight legs passing over the radar site.

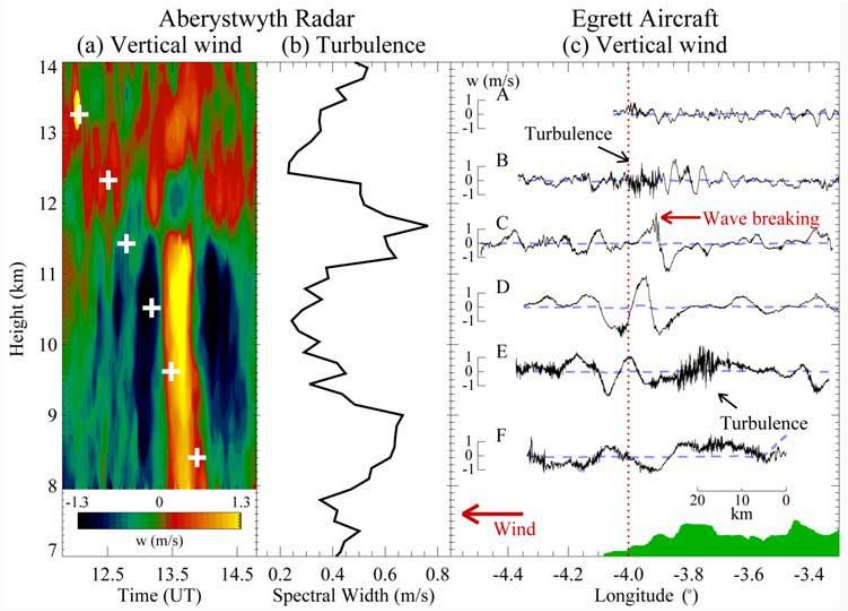

Figure 2.6: (a) Measurements of vertical wind by the Aberystwyth VHF radar. (b) Spectral width of the radar signal (proportional to turbulence intensity) averaged between 12:30 and 01:00 UTC. (c) Vertical wind measured on the Egrett. Each flight leg is placed at its height relative to the vertical scale in (a). The topographic height below the Egrett track is shown in green at the bottom with the same relative vertical scale as in (a). The coast of Wales is at 4.1° longitude; the position of the Aberystwyth radar is indicated by the vertical dotted line at 4.0° longitude. Crosses in (a) indicate the time and height when the Egrett passed directly above the radar. Taken from Whiteway et al., 2003.

Flight legs were undertaken at altitudes of 13.2 km, 12.3km, 11.4 km, 10.5 km, 9.6 km and 8.4 km. These are designated Legs A – F, respectively in Fig. 2.6. Vertical velocity plotted along the flight tracks reveals that the vertically propagating mountain wave leaned eastward with height and had its peak amplitude above the Aberystwyth VHF radar which was located at a longitude of -4°. The wave amplitude increased with height until flight leg C at a height of 11.4 km. The peak amplitude in the perturbation vertical velocity was 2 m/s. It can be determined whether the wave was actually breaking between

flight legs B and C by calculating the perturbation horizontal wind using Equation (2.26) as

$$-u' = \frac{m}{k} w' . \tag{2.44}$$

From the dispersion relation, m is approximately equal to N/u_o. The background horizontal wind was u_o = 10 m/s, so the vertical wavelength was 3 km. With of the horizontal wavelength being observed to be 10 km, the horizontal wave amplitude is 6.7 m/s at flight leg C. Wave overturning occurs where $u' > u_o$, so the wave is not yet overturning at the height of flight leg C. The wave would have started to overturn between flight legs C and B (heights 11.4 km and 12.5 km). Turbulence is present in flight leg B and it appears to commence on the crest of the wave in flight leg C. Also, the radar detects substantial turbulence (increased spectral width in the signal) in the height range of 11km to 12 km.

2.4.6 Phase relations expected for gravity waves

The basic measurements to be analysed in this thesis consist of temperature, pressure, and the three components of wind velocity. The measurements are interpreted using traditional Reynold's decomposition of fluid dynamical phenomena which involves separating a fluid flow into its time averaged background state and fluctuating components, i.e. perturbations that are induced relative to the background conditions. The perturbations are usually observed as oscillations and the different phenomena have unique relationships between the perturbations in temperature, and wind.

For gravity waves, the phase difference between temperature and vertical wind oscillations is straightforward. Where buoyancy is the resorting force, the maximum vertical wind will occur where the parcel is passing through its equilibrium position, and the vertical velocity will be zero at the maximum displacement. The temperature perturbation is proportional to the displacement and opposite in sign. Thus maxima in temperature perturbation occurs at the zero vertical wind perturbation. The oscillation in vertical wind perturbations shifted by 90^o in phase from the temperature perturbation.

The relationship between vertical and horizontal wind can be determined from Equation (2.26). In the case of a vertically propagating internal wave, with m and k real numbers, the horizontal and vertical wind perturbations are either in phase if m and k have the same sign, or 180 out of phase if m and k have the opposite sign.

If the horizontal and vertical wind perturbations are in phase then m and k have the same sign, and the group propagation direction is either downward and to the east ($m > 0,\ k > 0$) or upward and to the west ($m < 0,\ k < 0$).

If the horizontal and vertical wind perturbations are 180^o out of phase then the group propagation is either downward and to the west ($m < 0,\ k > 0$) or upward and to the east ($m > 0,\ k < 0$).

These phase relationships are illustrated in Fig. 2.7 for an internal gravity wave. In the case of an evanescent wave, m is imaginary and k is real, and the vertical and horizontal wind perturbations are 90^o out of phase.

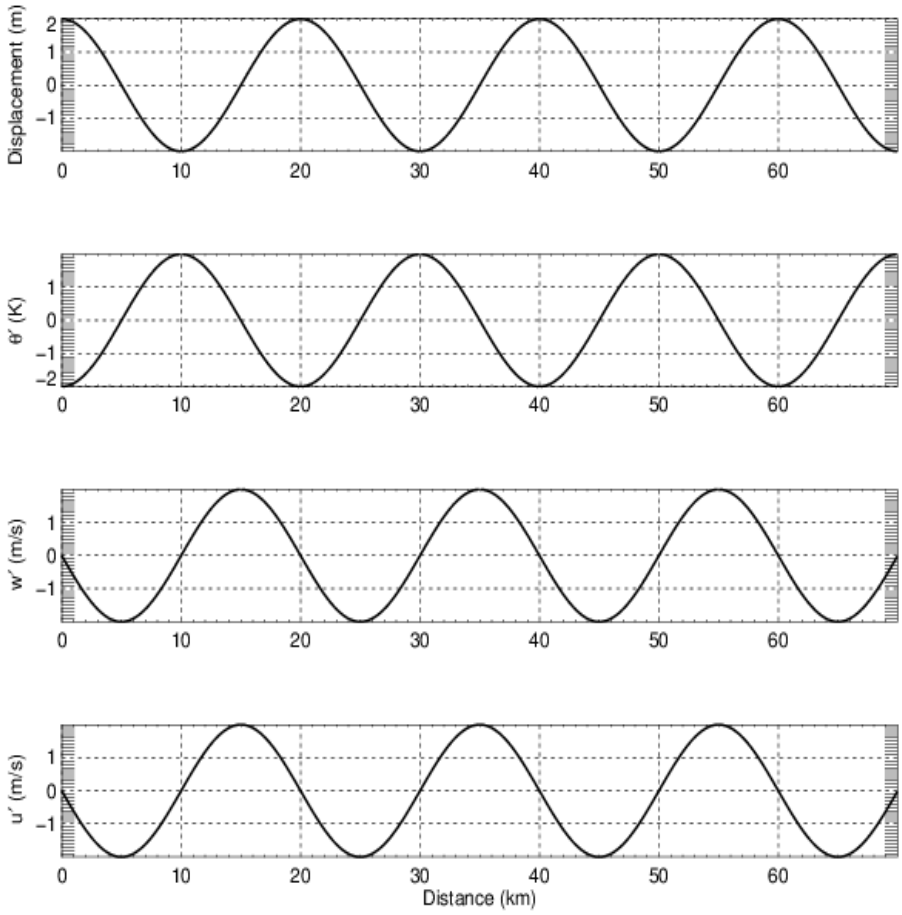

Figure 2.7: Phase relations between fluctuation in displacement, wind velocity and potential temperature. Fluctuations in vertical wind velocity are 90 degrees out of phase with fluctuations in potential temperature.

2.5 Rayleigh-Bénard Convection (Rolls)

Shear and convective instability within a flow can result in counter rotating rolls that are aligned with their axis parallel to the shear (Weckwerth et al., 1997). As illustrated in Fig 2.8, the relatively warm air moves upward while the cool air descends so that the rolls act to transport heat vertically and eliminate the unstable temperature gradient (Weiss & Ahlers, 2011). The vertical wind and temperature perturbations are in phase. The horizontal wind perturbations (if not flying through the center of the rolls) are

shifted by 90^{o} in phase from the vertical wind. These phase relationships for convective rolls as shown in Fig. 2.9 are distinctly different from the phase relations exhibited by gravity waves (Fig 2.7) and thus provide a means to discriminate between the separate phenomena.

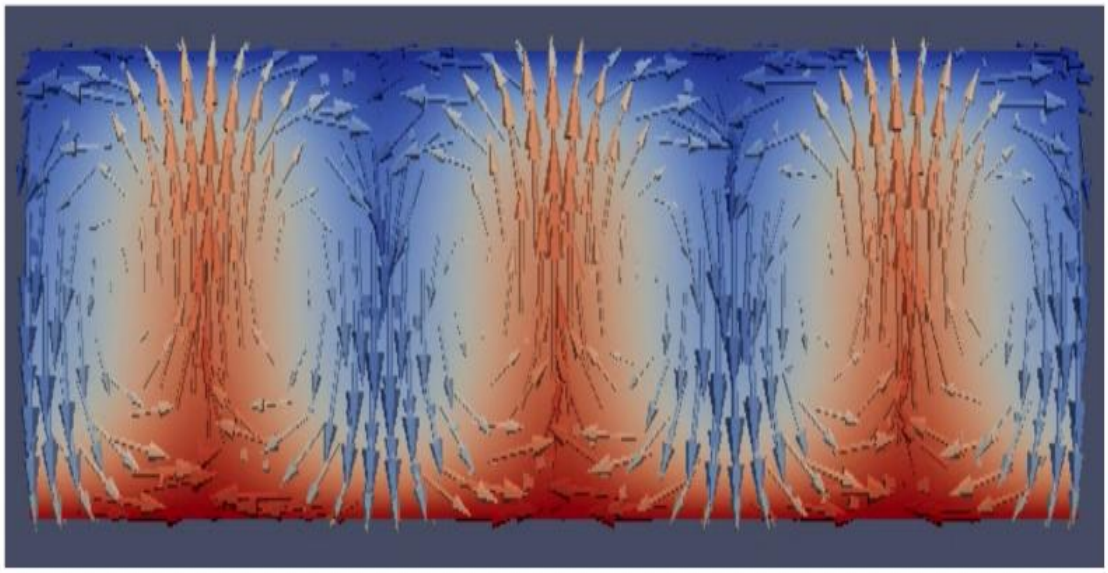

Figure 2.8: Numerical simulation of Rayleigh-Bénard convection with three rolls. Blue indicates relatively cool fluid, while red indicates relatively warm fluid. Figure taken from Alexei Stoukov, ENSEEIHT (École nationale supérieure d'électronique, d'électrotechnique, d'informatique, d'hydraulique et des telecommunications.)

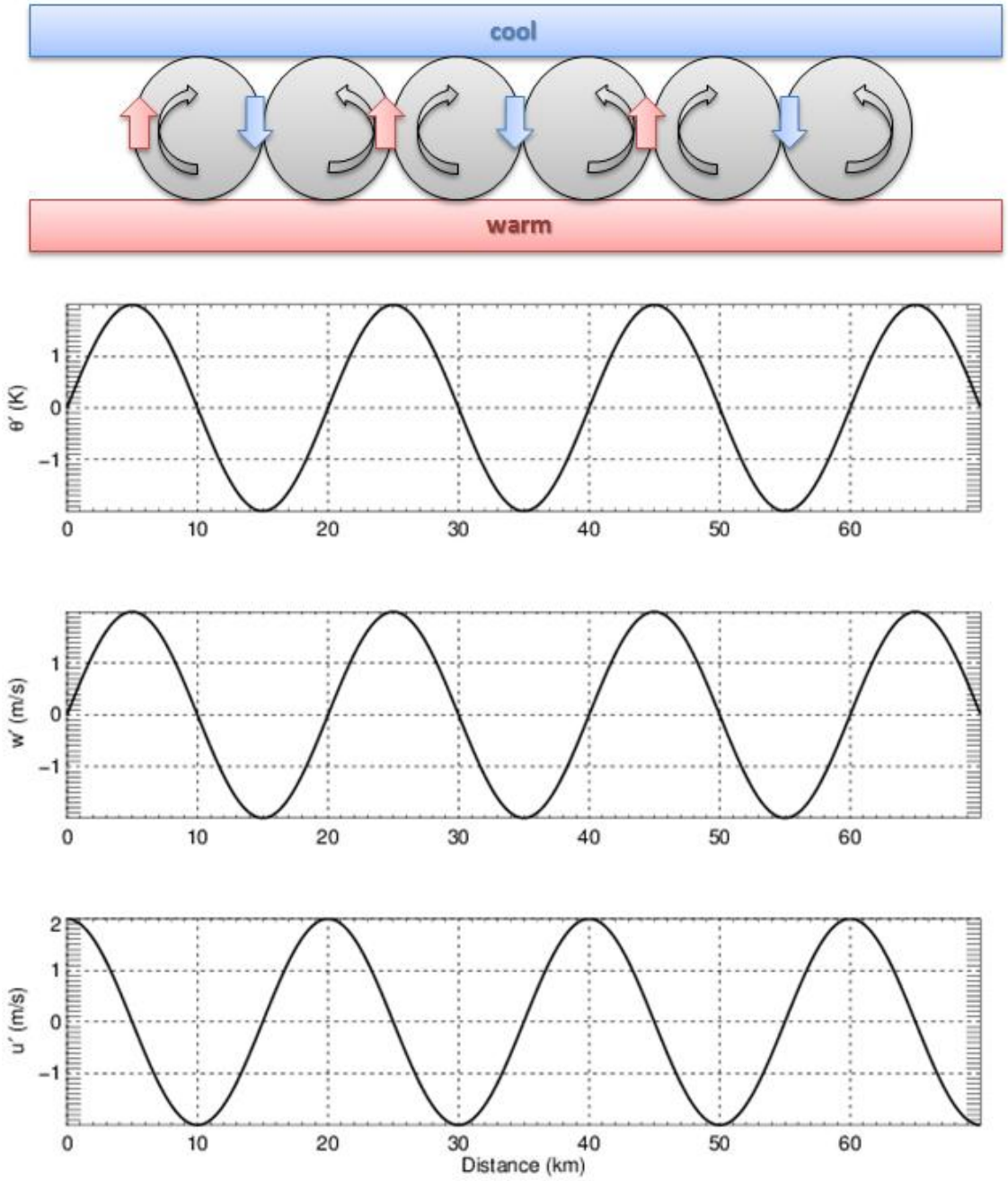

Figure 2.9: Phase relations for Rayleigh-Bénard convection showing three convective rolls. Fluctuations in vertical velocity are in phase (0^o shift) with potential temperature fluctuations.

2.5.1 Rankine Vortex

Another type of vortical motion that was considered can be represented by a Rankine vortex (Giaiotti and Skel, 2006). The Rankine vortex was modeled and subjected to wavelet analysis methods (see Chapter 3) to determine the nature of coherent features being observed by characteristic phase shift relations between perturbations in vertical velocity and potential temperature. Phase relations were unclear and consequently, the Rankine vortex was not considered further. Its description is included here for completeness.

A Rankine vortex resembles solid body rotation such that the angular velocity is constant out to the edge of the vortex, and the tangential velocity thus increases linearly with distance from the centre of the vortex. The velocity tapers off exponentially beyond the defined edge of the vortex. The mathematical description is as follows,

$$v_\phi(r) = \begin{cases} \Omega r / 2\pi R^2 \\ \Omega / 2\pi r \end{cases} \qquad (2.45)$$

$$r \le R,$$
$$r > R.$$

where v_ϕ is the tangential velocity, Ω is the solid body rotation rate and R is the radius of the vortex. Figure 2.10 shows that the vertical displacement increases linearly with distance from the centre of the Rankine vortex.

The deviation in potential temperature is proportional to the vertical displacement and thus has maxima at the outer edges of the vortex. If the background atmosphere has stable stratification (potential temperature increasing with height) then the positive temperature deviation will occur on the side of the vortex with air moving downward. Negative temperature perturbation occurs at the side of the vortex with air moving upward. The perturbations in vertical wind and temperature are thus 180^o out of phase for a Rankine vortex in stable stratification. If the background atmosphere is convectively unstable then the phase relationships are the same as for the Rayleigh-Bénard convective rolls.

Again, w' and θ' are in phase (0^o phase shift). If the aircraft were to fly through the vortex displaced in height from the axis of the vortex, u' would be 90^o out of phase with w'. It should be noted again that wherever there are vertical displacements, these vertical displacements will displace background shear and accordingly, interpretations based on horizontal wind fluctuations are complicated by the displacement of vertical shear. The correlation between fluctuations in vertical wind velocity and potential temperature is more reliable for delineating between rolls, vortices and waves.

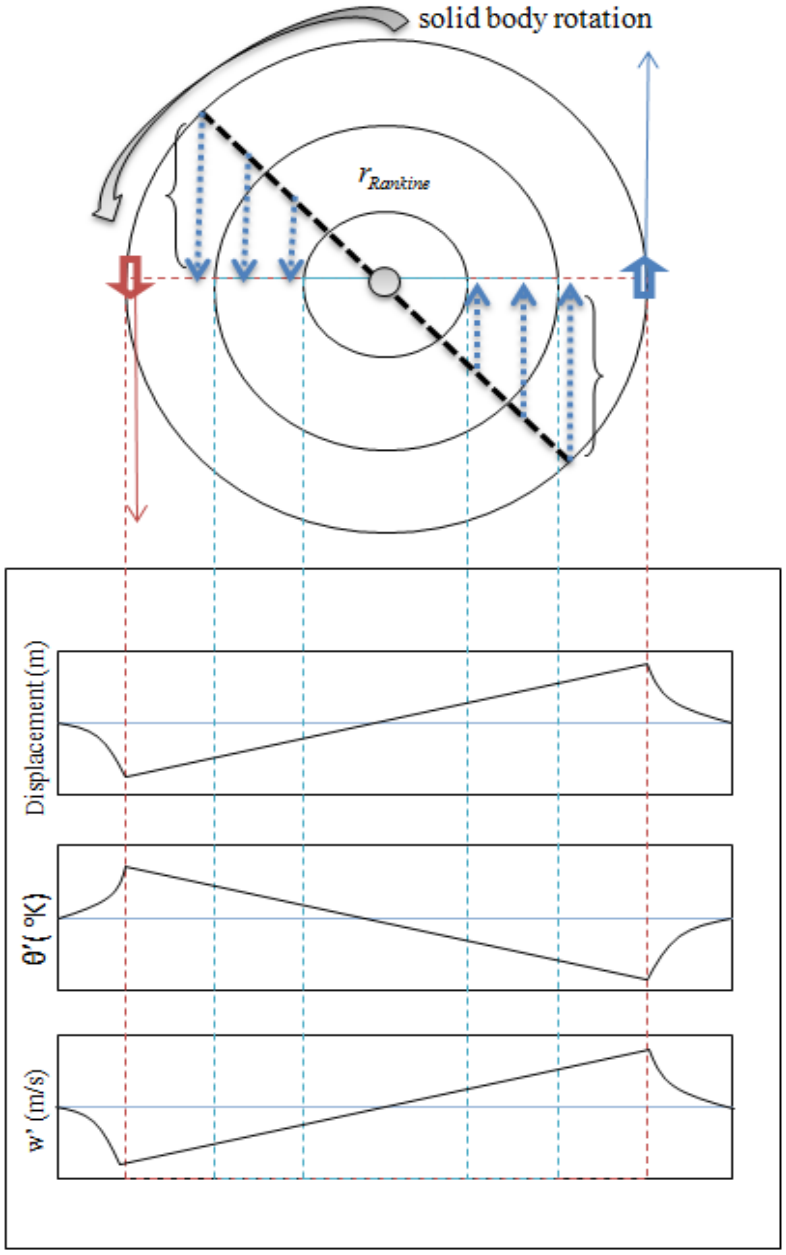

Figure 2.10: Phase relations for a rankine vortex.

2.6 Turbulence

Turbulence is a region within a fluid where it has become destabilized, breaking down into random and rotational disturbances such that the flow is no longer laminar but chaotic. Further discussion on the nature of turbulence and its mathematical treatment can be found in several seminal textbooks on the subject, i.e. Batchelor (1956), Lumley and Panofsky (1964), and Tennekes and Lumley (1972.) The intent of this section is to familiarize the reader with basic turbulent quantities and characteristics which are subsequently used in the interpretation of experimental results. Consequently, instead of offering rigorous definitions, I summarize here the most important properties of turbulence as relevant to the measurements presented in Chapter 4:

1. Turbulence behaves stochastically, i.e. turbulence is chaotic and highly dependent on the initial conditions of the system. For this reason, the time evolution of turbulent processes cannot be well predicted and often requires the use of statistical analysis methods.
2. Turbulent motions facilitate an energy cascade from larger to smaller scales (Hodges, 1967). Large eddies decay into progressively smaller eddies. Ultimately at the smallest scales, kinetic energy is converted to heat through viscous dissipation.
3. Turbulence is dissipative and requires continuous energy input to the system in order to overcome kinetic energy loss due to viscous shear stresses and buoyancy. The need for continual energy input is one characteristic which distinguishes turbulence from other small scale

atmospheric phenomena such as broad spectrum gravity waves (Tennekes and Lumley, 1972.)

4. Turbulence is diffusive. Examining the Lagrangian path of a parcel of fluid in a turbulent flow reveals that the parcel wanders progressively farther from its initial position, exchanging significant heat, momentum and mass with other parcels. For this reason, turbulence facilitates vigorous, irreversible small scale mixing.

In the case of the atmosphere, especially at UTLS altitudes, the threshold at which a sheared flow transitions from laminar to turbulent is indicated by the Richardson number. The Richardson number (Ri) is a dimensionless quantity describing the ratio of buoyant to shear forces and is given by the expression:

$$Ri = \frac{N^2}{\left(\frac{du}{dz}\right)^2} \tag{2.46}$$

It can be expected that turbulence generation will be sustained if the mechanical shear forcing overcomes the damping by buoyancy, i.e. at a Richardson number of approximately unity (Hines, 1971). The critical Richardson number (Ri_C) is defined as the value of Ri at which laminar flows transition to turbulence and has the empirical value $Ri_C = 0.25$. In assessing vertical profiles of the atmosphere, areas of turbulence typically correspond to $Ri_C \leq 1$ (Hines, 1971; Martin, 1985).

2.6.1 The Spectrum of Turbulence

Atmospheric turbulence possesses a universal kinetic energy spectrum spanning multiple scales. Each scale regime has a distinctive characteristic spectral slope. From the perspective of energetic processes occurring, the spectrum of turbulence can be divided roughly into three regions: (A) a source region, (B) a transfer region, and (C) a sink region. Progressing from smaller to larger wave numbers (larger to smaller wavelengths) in the first, or source region (denoted 'A' in Fig. 2.11), energy is introduced into the system by a generation mechanism through convective or shear instability.

The second region ('B' in Fig. 2.11) is known as the inertial subrange in which there is a transfer of energy by a non-linear processes from smaller to larger wavenumbers (larger to smaller wavelengths.) The third and final region, ('C' in Fig. 2.11) is known as the dissipation subrange and encompasses the Kolmogorov microscale and dissipation of energy as heat.

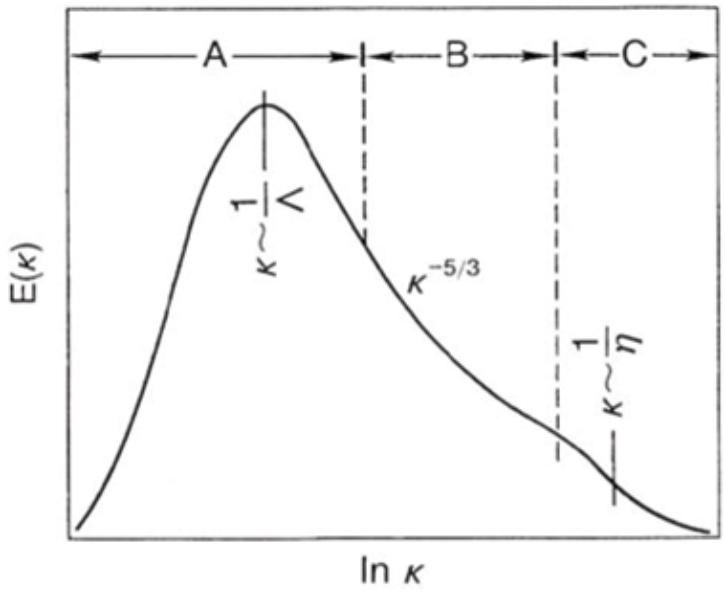

Figure 2.11: Turbulent energy spectrum, E(**κ**), associated with range of wavenumbers, **κ**. Taken from Kaimal and Finnigan (1994). Region (A) is where energy is produced, region (B) is the inertial subrange and region (C) is the dissipation range where kinetic energy is lost as heat. The symbols Λ and η represent the integral length scale of turbulence and the Kolmogorov microscale length, respectively.

The inertial subrange is the most familiar turbulent regime and exists at the scales where turbulence is usually considered to be locally isotropic. Dimensional analysis can be used to derive the equation for the power spectrum in the inertial subrange as follows,

$$E(\kappa) = A\varepsilon^{\frac{2}{3}}\kappa^{\frac{-5}{3}}. \tag{2.47}$$

The parameter *A* represents a universal constant which has experimentally been found to have a value of approximately 1.4. ε is the rate of energy dissipation per unit mass from viscous action (Lumley and Panofsky, 1964.) The upper and lower bounds of the inertial

subrange are referred to as the outer and inner scales of turbulence and are denoted L_B and l_0, respectively.

Situated at the border between inertial and buoyancy subranges, the outer scale of turbulence is given by

$$L_B \approx c\varepsilon^{\frac{1}{2}} N^{\frac{-3}{2}}, \tag{2.48}$$

where *c* is a constant of proportionality of experimentally determined values varying between 0.2 and 1.0 (Hocking, 1987). Equation (2.48) illustrates that L_B is dependent solely on the energy dissipation rate and the Brunt-Väisälä frequency. At larger scales lies the buoyancy subrange, a region encompassing motions where stratification becomes important and turbulence is considered to take on a quasi-two dimensional in character.

At the small scale end of the inertial subrange, there is the viscous subrange where viscosity becomes significant and leads to the eventual dissipation of turbulent energy into heat. The scale at which this occurs is called the Kolmogorov microscale, η, and is given by

$$\eta = \left(\frac{\nu^3}{\varepsilon} \right)^{\frac{1}{4}}. \tag{2.49}$$

Where *v* represents the fluid's viscosity.

Chapter 3: Measurements and Analysis Methods

The research presented throughout this thesis is an analysis of airborne in situ and laser remote sensing measurements to study the characteristics of atmospheric dynamics in the anvil outflow from deep convection in the tropics. The measurements were acquired as part of a project called EMERALD-2: Egrett microphysics Experiment with Radiation Lidar and Dynamics. The field experiment was carried out from Darwin, Australia during the pre-monsoon build up period in November and December of 2002. Case studies from two other connected campaigns, the Aberystwyth Egrett Experiment (2000) and the EMERALD-1 campaign (2001) are presented for comparison purposes.

This chapter provides an overview of the experimental platform as follows:

- describes the Egrett and King Air aircraft,
- details the on-board instrumentation including the lidar system, specifying which instrument data and measurements were analyzed for this thesis,
- outlines design and experimental objectives of the EMERALD-2 campaign in general, and,
- overviews anvil outflow geometry and flight tracks and finally describes techniques of data analysis employed in Chapter 4.

3.1 The Aircraft and Payload

The Egrett aircraft (Fig. 3.1) was designed for reconnaissance with the ability to sustain slow flight at altitudes up to15 km. It has a wingspan of 30 meters and is powered by a single turboprop engine. Air speeds vary between approximately 80 m/s and 100 m/s during science flights.

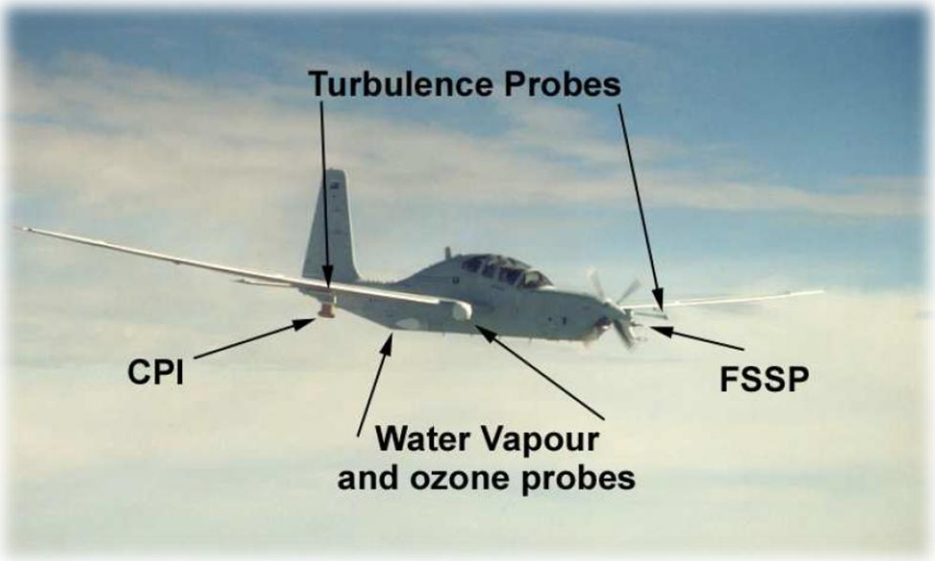

Figure 3.1: The Egrett aircraft outfitted with the suite of instruments for the EMERALD project to measure wind speed, temperature, pressure, water vapour, ozone, far-IR spectra, aerosol, and cloud particle microphysical properties .

The Egrett was outfitted with instruments to measure wind, temperature, pressure, water vapour, cloud particles, IR spectra, ozone, position, orientation and attitude. Instruments for measurements from the aircraft were provided by a collaboration between five institutions as listed in Table 3.1. The project was led by Dr. J. Whiteway from The University of Wales, Aberystwyth (UWA).

Table 3.1: EMERALD-2 instrument payload (aboard Egrett and King Air).

Atmospheric Property	**Instrument**	**Institution***
Wind, Pressure Temperature (Egrett)	Best Atmospheric Turbulence (BAT) probe Rosemount probe	ARA
Ice Microphysics	Forward Scattering Spectrometer Probe (FSSP) Cloud Particle Imager (CPI)	UMIST
Water Vapour	Frost Point Hygrometer Tunable Diode Laser (TDL)	DLR UWA
Far IR Spectra	Tropospheric Airborne Fourier Transform Spectrometer (TAFTS)	IC
Ozone	TE-49C Ultra-violet absorption Spectrometer	DLR
Lidar	532 nm, polarization Lidar	UWA
Aircraft position	Novotel GPS	ARA
Aircraft Attitude	INS	ARA

*Contributions from University of Wales at Aberystwyth (UWA), Airborne Research Australia of Flinders University (ARA), University of Manchester Institute for Science and Technology (UMIST), Imperial College, London (IC), and Deutsch zentrum für Luft und Raumfahrt (DLR).

The King Air (Fig. 3.2) is a twin turboprop engine aircraft. It was outfitted with an upward pointing lidar system, GPS positioning, and an inertial navigation system for aircraft orientation and attitude.

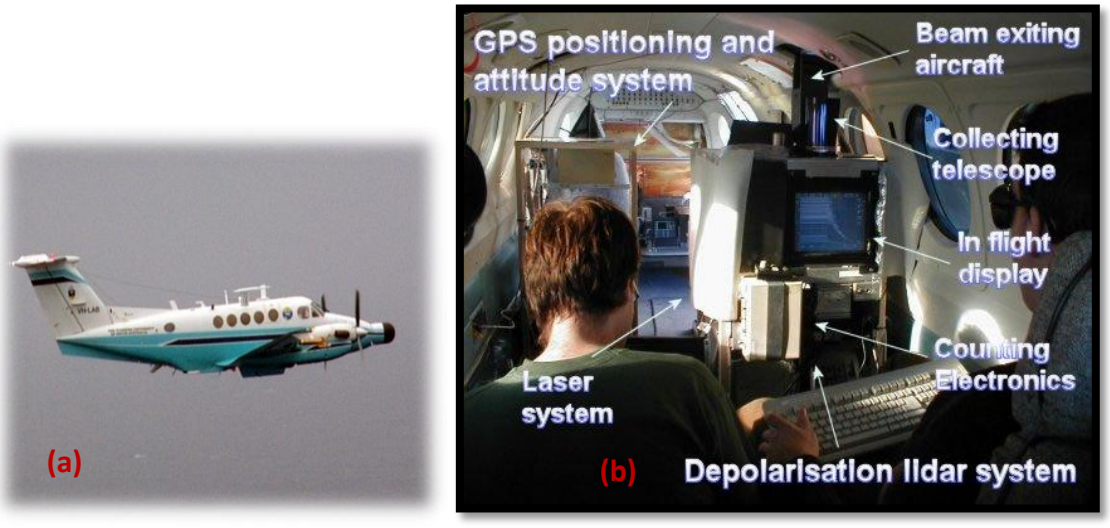

Figure 3.2: The King Air **(a)** external view, **(b)** internal instrumentation and cabin configuration.

The basic experiment design was that in situ sampling was carried out from the Egrett aircraft within the anvil outflow cloud, while the King Air mirrored the Egrett's flight track at lower altitudes. The lidar system aboard the King Air measured the cloud structure that the Egrett was sampling within. This provided a basis for real time decisions on the flight path and also a context for the interpretation of the Egrett in situ measurements. Figure 3.3 shows pictures of the convective anvil outflow from the perspective of the Egrett at the cloud level and from the King Air below the outflow.

Capability to resolve UTLS region wave and turbulent flows to a horizontal resolution of within 4 m was achieved through data collection at a recording rate of 25 Hz. The wind measurements presented have uncertainty with a standard deviation in the horizontal of ±10 cm/s and in the vertical direction of ±15 cm/s, which are small in relation to the amplitude of coherent structure disturbances (typically ~1m/s) of interest in this thesis. Potential temperature was calculated according to Equation 2.6, using pressure and temperature measurements collected from the BAT probe. Error bars are small (consequently not displayed here) and are consistent with Cook, 2004. Systematic errors considered included variation in aircraft height between measurements and hydrostatic correction for pressure. Systematic error effects were found to be negligible in all cases, namely of the order of 0.1% of the measured variations.

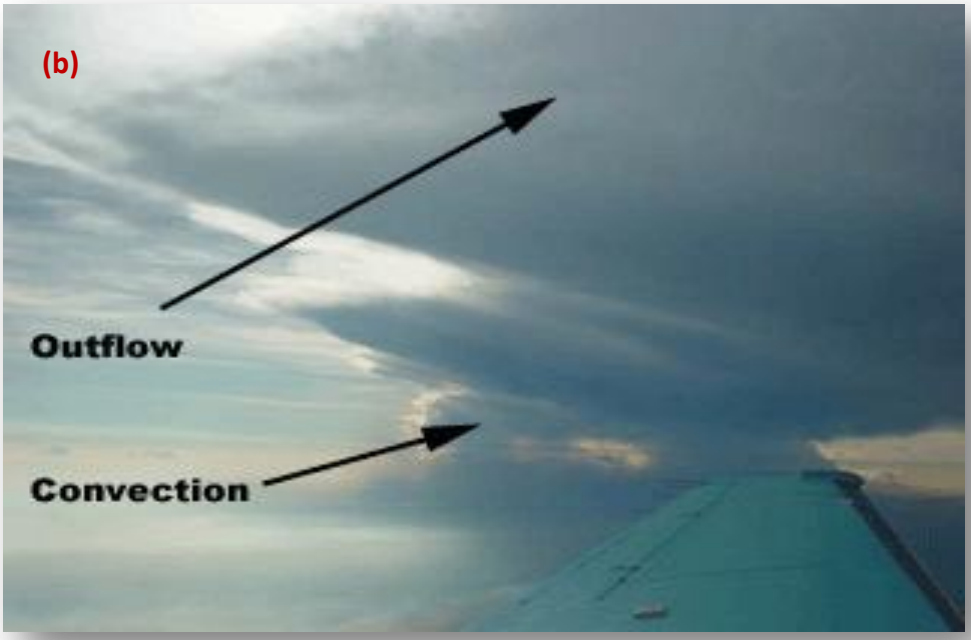

Figure 3.3: Hector's anvil outflow as seen from **(a)** the Egrett (altitude 15 km) and **(b)** the King Air (altitude 5 km.)

3.2 Airborne Measurements of Wind, Temperature and Pressure

Temperature, pressure, and the three-dimensional wind vector were measured using two probes for redundancy, the BAT and Rosemount, one mounted under each wing of the Egrett. The BAT or "Best" Aircraft Turbulence probe (Fig. 3.4(a),) is based on a 15 cm diameter spherical surface with nine holes for pressure measurements. The probe was mounted below the left wing of the Egrett on a 2.5 m boom with the tip protruding approximately 1.5 m beyond the wing's leading edge.

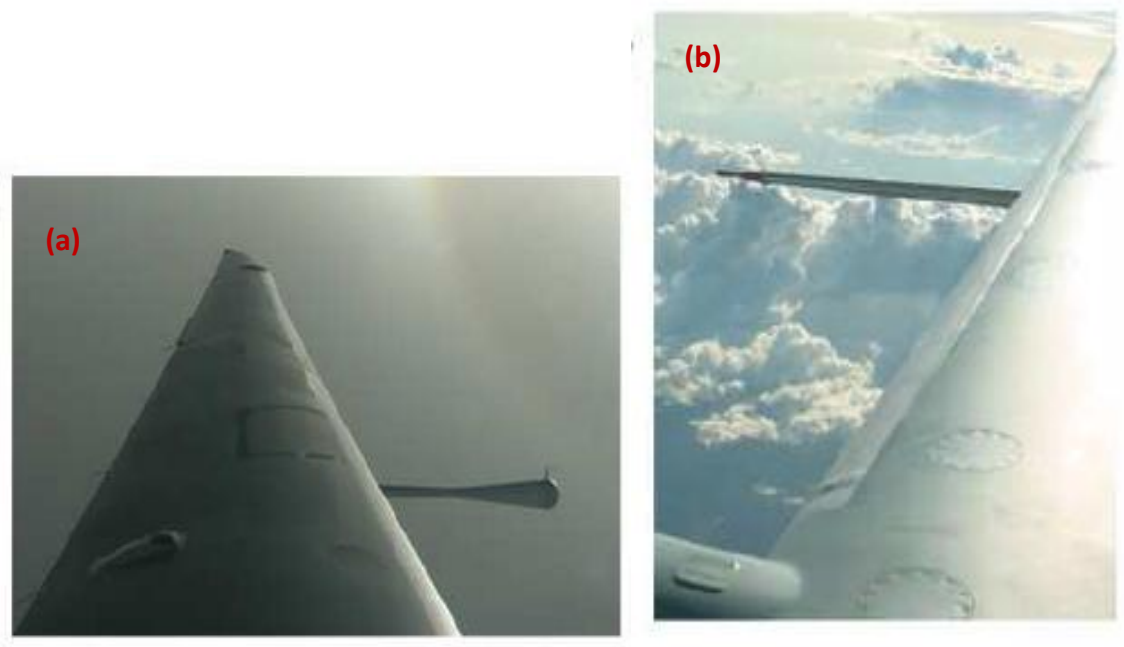

Figure 3.4: **(a)** BAT probe mounted on the left wing of the Egrett aircraft, **(b)** Rosemount turbulence probe mounted on the right wing of the Egrett aircraft.

The Rosemount probe was based on the same concept but with pressure sampled from only five points on a spherical surface that protrudes into the flow. I have presented measurements from the BAT probe except for rare cases in which BAT data was

unavailable. In such cases, the Rosemount probe measurements have been used as a back-up.

The method of determining the three dimensional wind velocity followed that of Crawford and Dobosy (1997). This task was carried out prior to the commencement of this thesis and the work reported here makes use of the final data products. Briefly summarizing, the calculations for the final 3D wind vector involve the summation of two vastly larger scale vectors providing: 1. the wind as measured relative to the sensors, and, 2. the velocity of the sensors measured relative to Earth. Determination of these two vector quantities in turn depends upon motion and orientation of the aircraft over a spectrum of time scales from several minutes to 0.02 seconds.

The wind speed relative to the probe is combined with in situ measurements of aircraft velocity and acceleration in all three dimensions, i.e. along the pitch, yaw, and roll axes, to allow for minute changes in aircraft heading, angle of attack and amount of sideslip. The airspeed relative to the probe is determined by sampling the distribution of pressure over a spherical surface.

3.3 Lidar System

A lidar system was used for measuring the cloud structure. The basic method was to emit pulses of light into the atmosphere and detect the light that is scattered back as a function of time or, equivalently, distance. The lidar used aboard the King Air was based upon an Nd-YAG laser system, making use of the second harmonic output at a

wavelength of 532 nm. The receiving system consisted of a 10 cm diameter telescope with one meter focal length and a field stop radius of 0.5 mm, to yield a field of view (FOV) of 0.5 mrad. Background light was reduced with an interference filter with a bandwidth of 1 nm. A polarizing beam splitter was used to separate the two components of backscatter polarization relative to the emitted light. Two photomultipliers were used to detect the backscattered light and the data was acquired using the method of photon counting.

Figure 3.5 displays the lidar system (a) schematically, (b) in the lab during the testing phase at the University of Wales, Aberystwyth, and (c) ultimately installed on the King Air, awaiting flight. Once installed on the King Air, the upward pointing lidar system was capable of detecting backscatter to distances of up to 30 km above the aircraft's altitude with a vertical resolution of within 30 m (depending on the atmospheric opacity and background light level).

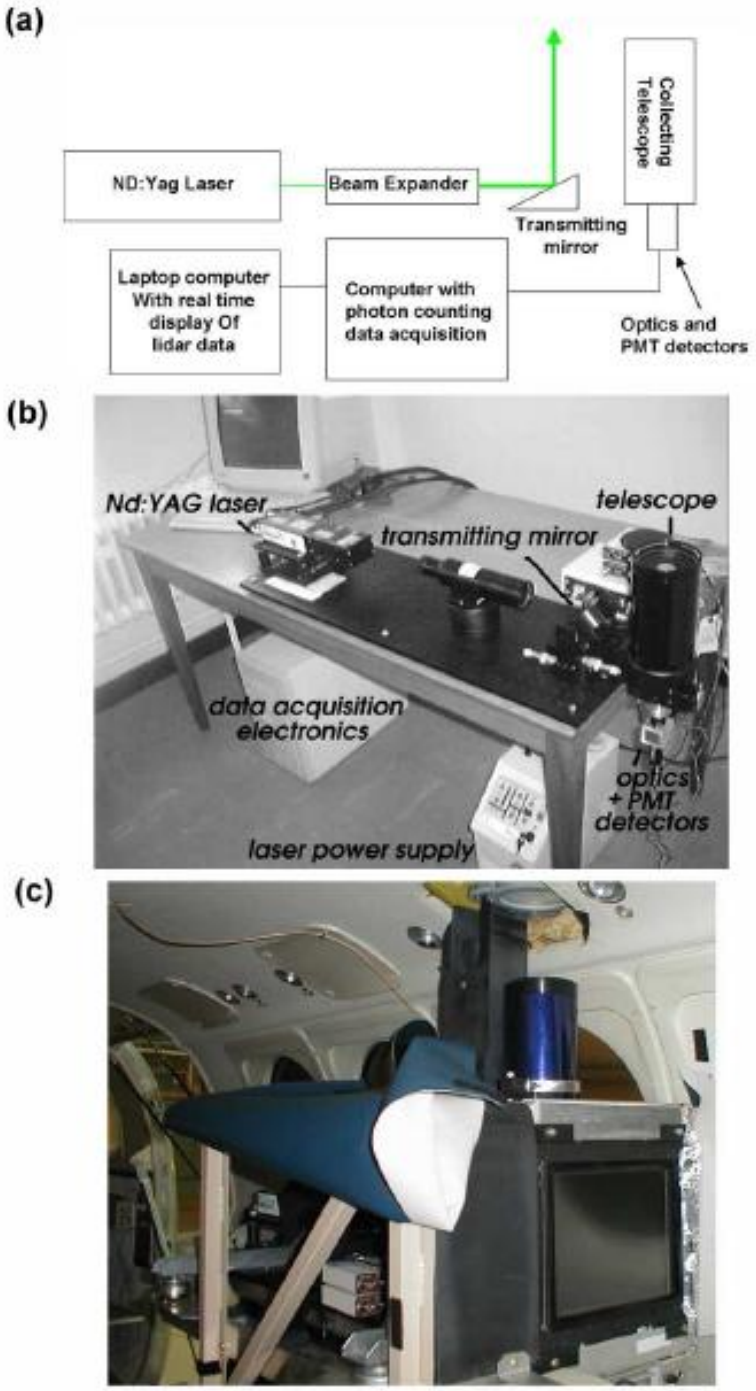

Figure 3.5: (a) Schematic diagram of the lidar employed aboard the King Air for the EMERALD 2 campaign. (b) Lidar system under construction in the lab, (c) lidar system installed on the King Air with upward pointing orientation.

As lidar analysis is not the focus of my research, the lidar contour plots presented in Chapter 4 are included in this thesis only in order to provide a spatial frame of reference as to where dynamical features of interest occur with respect to the geometry of the cirrus anvil outflow, i.e. with respect to the cloud base. Consequently, no scales in terms of backscatter coefficients are provided as this information is inapplicable given that the outflow is too dense for the laser beam to penetrate. Table 3.2, below, provides the lidar system's specifications.

Table 3.2: EMERALD-2 lidar transmitter specifications

Wavelength	532 nm
Pulse Energy	34 mJ
Near Field beam diameter	2.5 cm
Pulse Width	5.7 sec
Divergence	0.1 mrad
Repetition rate	up to 20 Hz

3.4 Design of the Experiment

A basic goal of the experiment was to position the Egrett aircraft within the anvil outflow from tropical deep convection and obtain in situ measurements. The plan was to coordinate both aircraft such that the lidar measurements from the King Air could be used to inform the in-flight decisions on flight path and provide a context of the anvil outflow geometry for the analysis and interpretations.

The location of Darwin, Australia was chosen primarily since it is in close proximity to the Tiwi Islands. During the November-December build up period between the dry and wet seasons, an isolated convective event occurs over the Tiwi Islands each

afternoon (Carbone et al., 2000). Convection is initially triggered in the sea breeze fronts. Collision of the gust fronts from individual cells then enhances the overall event to produce a major storm over the Tiwi Islands that extends to the tropopause (Beringer et al., 2001; Keenan et al., 1989; Keenan et al., 1990; Skinner and Tapper, 1994).

The science flights for the EMERALD-2 campaign took place at a time period when there was a major convective event over the Tiwi Islands every afternoon. This phenomenon is readily visible from Darwin on a regular basis, and it has been given the name Hector by the local population and aviation community. Photographs of Hector were shown in Fig. 3.3. An example of a cross section of Hector from measurements by the the Darwin C-pol radar is shown in Fig. 3.6. Such radar products were used for initial planning for the flights each day at the Darwin office of the Australian Bureau of Meteorology (BOM). Thus the location of Darwin was chosen since it is a natural laboratory for studying tropical convection (Beringer, Tapper, and Keenan, 2001; Fischer et al., 1997; Holland, 1986; Keenan et al., 1990; Keenan, Ferrier, and Simpson, 1994), the required aircraft support facilities were available at the RAAF base, and Darwin is one of the most instrumented sites in the tropics for meteorological measurements.

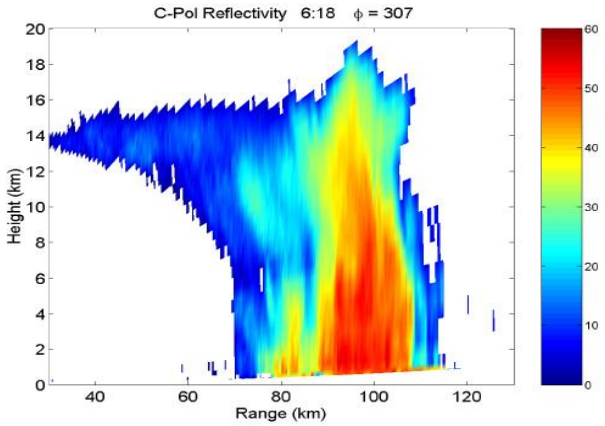

Figure 3.6: CPOL radar reflectivity as measured in a vertical scan of Hector's convective tower and cirrus anvil outflow (dark blue, regions between ~0-70km) This scan was taken looking north near Darwin at 6:18 p.m. local time on November 15, 2001. Figure by Peter May of the Australian Bureau of Meteorology (BOM).

The research presented in this thesis was primarily concerned with the study of turbulence and coherent structures within the anvil outflow from storm called Hector. This primarily involved using the in situ wind, temperature, and pressure measurements from the BAT and Rosemount probes that were mounted under the wings of the Egrett aircraft. Contour images of lidar backscatter from the lower flying King Air aircraft were used to design the flight patterns in real time. In my analysis, contour images were generated to provide context in terms of the geometry of the convective anvil outflow.

3.4.1 Anvil Outflow Geometry and Flight Tracks

The flight of 23 November 2002 is used in this section to illustrate the experiment design relative to the typical geometry of the convective anvil outflow over the Tiwi Islands. The primary objective at the outset of each flight was to have flight legs across

the anvil cloud, transverse to the direction of the outflow. The secondary objective was to obtain longitudinal flight legs along the axis of the outflow.

Prior to launch of the flight, the real time radar images available at the Darwin office of the Australian Bureau of Meteorology were used to view the geometry of the developing convection and outflow (eg. Fig. 3.7). This was used to inform the design of a baseline for the first flight legs. An actual flight pattern was decided in real time during the flight with decisions made by the PI (J. Whiteway) within the King Air aircraft, based on visual inspection of the clouds and the lidar measurements. The images of Hector's convective core from the Darwin C-Pol radar (Fig. 3.7) were also obtained in flight over a satellite telephone link and were used mainly to avoid positioning the aircraft too close to the active core.

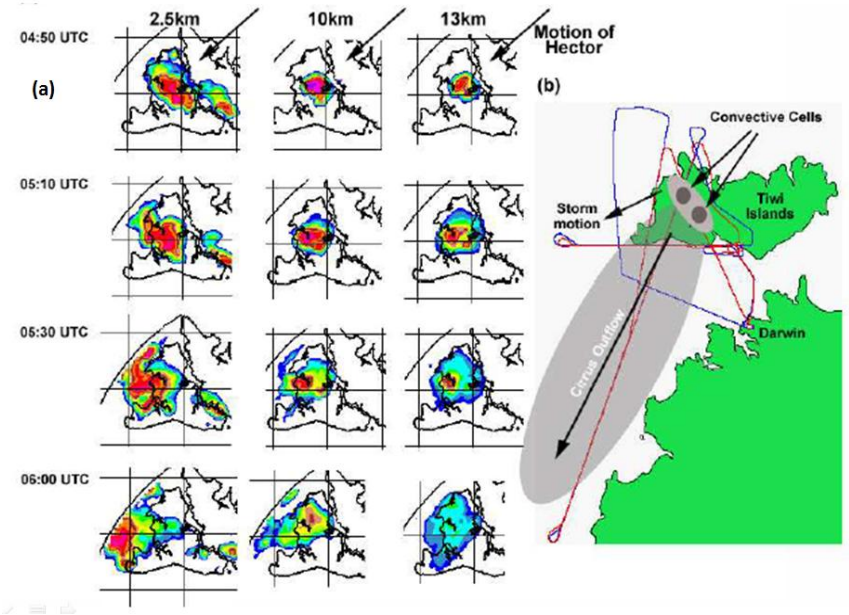

Figure 3.7: (a) Australian Bureau of Meteorology C-pol radar backscatter contours outlining the convective core at different altitude levels and times for November 23, 2002. (b) Flight tracks of the Egrett (red) and King Air (blue) are shown relative to the regional geography and the direction of the cirrus outflow. 06:00 UTC corresponds to 3:30 p.m. local time. Taken from Cook, 2004.

A satellite infrared image from the mid afternoon of November 23 is shown in Fig. 3.8(a) in which it is apparent that an isolated convective core was developing over the Tiwi islands. The satellite IR image from later in the afternoon in Fig. 3.8(b) shows that the convective anvil outflow extended a few hundred kilometers to the south. Figure 3.8(b) also shows the basic flight pattern with legs both across and along the outflow.

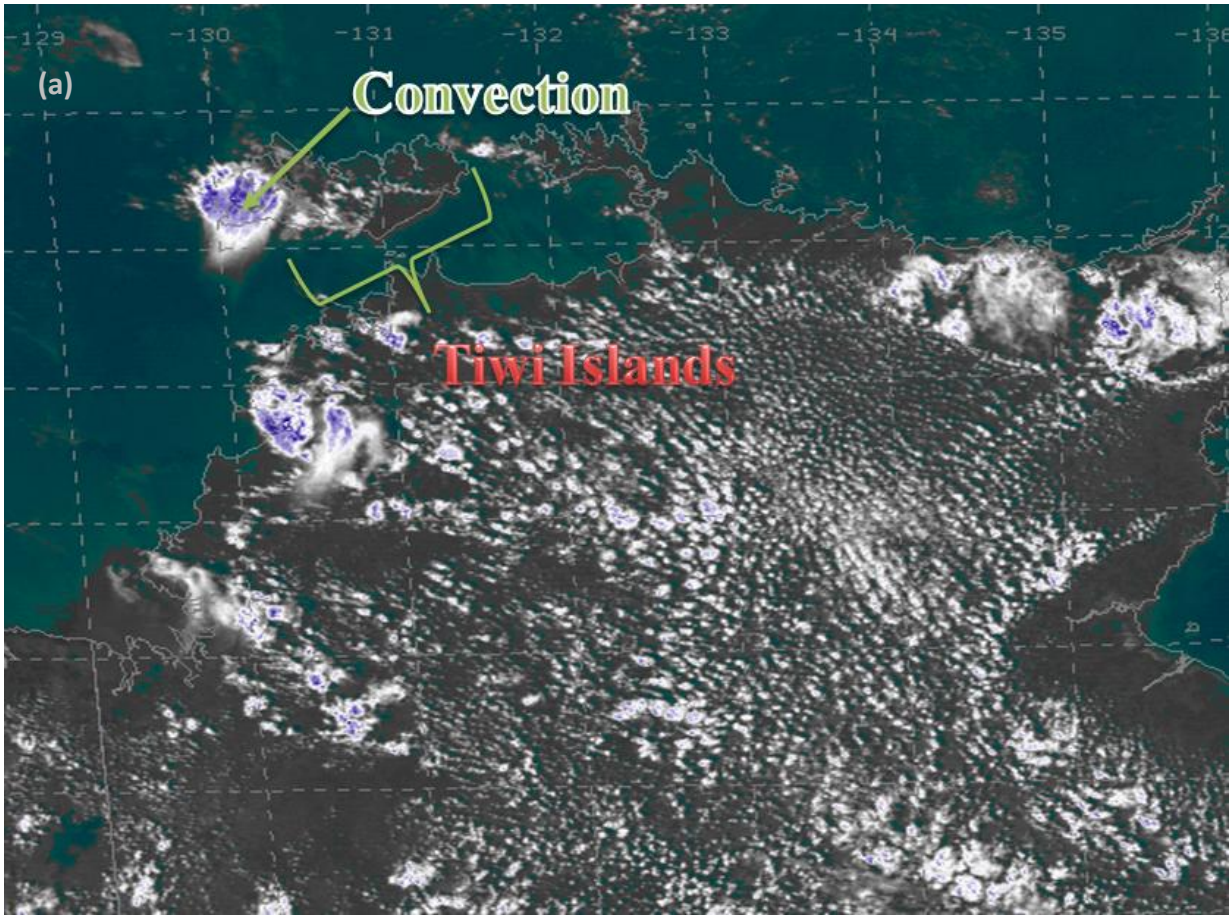

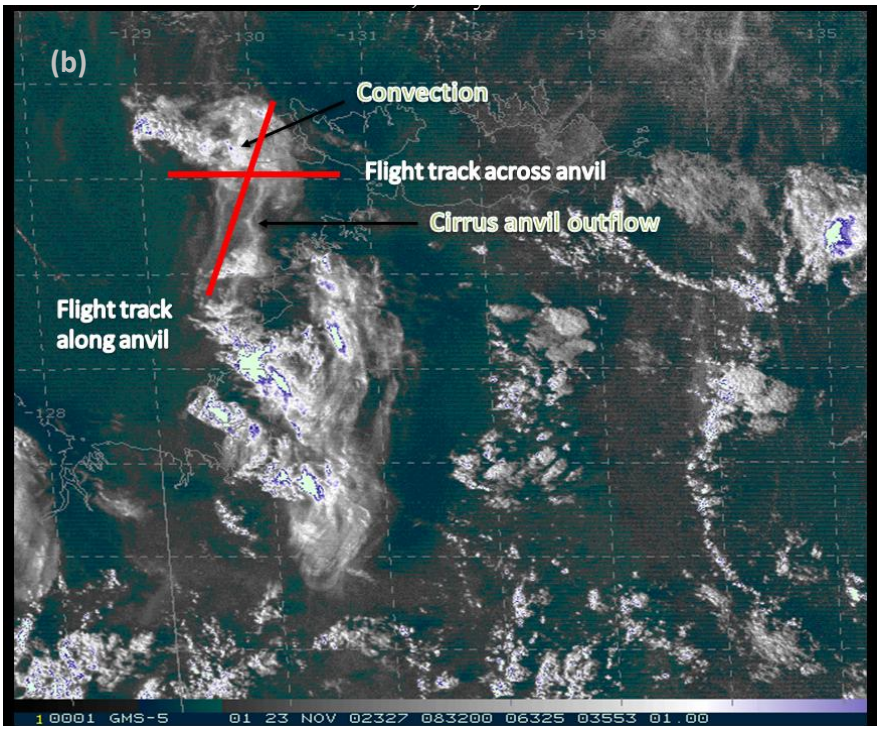

Figure 3.8: Satellite IR imagery from 23 Nov. 2002. **(a)** Early afternoon: developing convection over Tiwi Islands. **(b)** Late afternoon: remnants of convection with cirrus anvil outflow.

Figure 3.9 shows the exact flight pattern for each aircraft from on board GPS positioning. There were four flight legs. Two legs were oriented across the anvil outflow, back and forth, east-west along latitude 11.2^{o}S, and two legs were oriented north-south, southward along the anvil moving away from the convective core, and then northward back toward the core and through its remnants. Table 3.3 summarizes the details of the four presented flight legs undertaken on November 23, 2002.

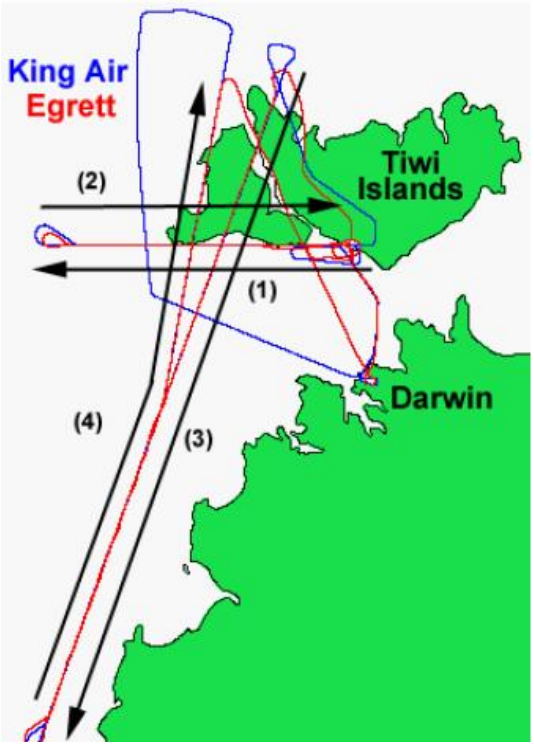

Figure 3.9: Four flight legs on November 23, 2002. Egrett track in red, King Air track in blue. Taken from Cook, 2004.

In order to afford spatial perspective, lidar contour images displaying the outline of the anvil base for the transverse flight legs (1 and 2) are shown in Fig 3.10. In these cases the anvil cloud was so thick that the lidar could not detect a signal for distances of more than 1.5 km above the cloud base since the laser pulses were completely attenuated within the cloud. From the longitudinal flight legs shown in Fig 3.11, the outflow cloud was relatively thin (optically) and the lidar was able to measure through the entire cloud.

Table 3.3: Overview of transverse (1, 2) and longitudinal (3,4) flight legs on Nov. 23, 2002.

Flight Leg	Altitude (km)	Length (km)	EM 2 designation
1	12.64	73.42	a7r1_391
2	13.56	128.47	a7r2_420
3	14.44	296.54	a7r3_saw
4	13.01	197.03	a7r4_saw_b

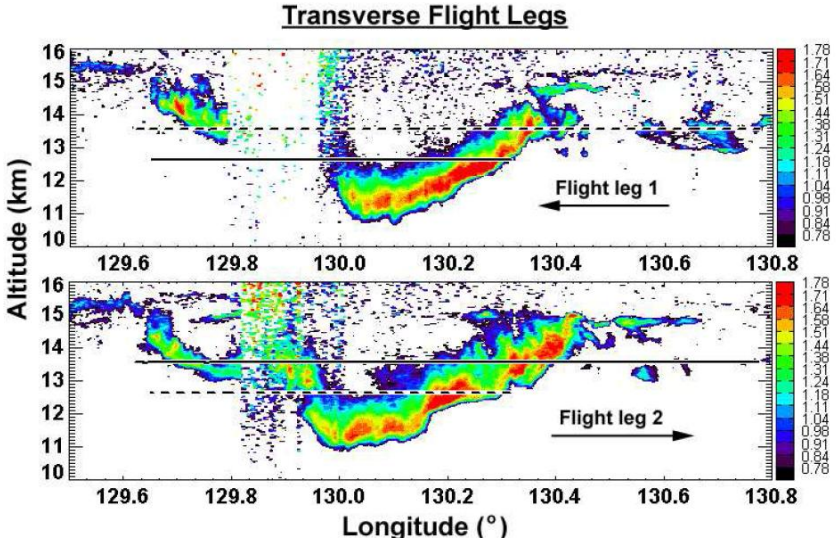

Figure 3.10: Lidar backscatter contour plot of the anvil base showing flight leg altitude and track taken across the outflow for flight leg 1, oriented westward at approximately 12.7 km, and flight leg 2, oriented eastward at approximately 13.6 km. Outflow direction is out of the page, toward the reader. Solid lines represent the flight leg actively shown in the panel while dotted lines show where the other flight leg in the other direction occurred. Taken from Cook, 2004.

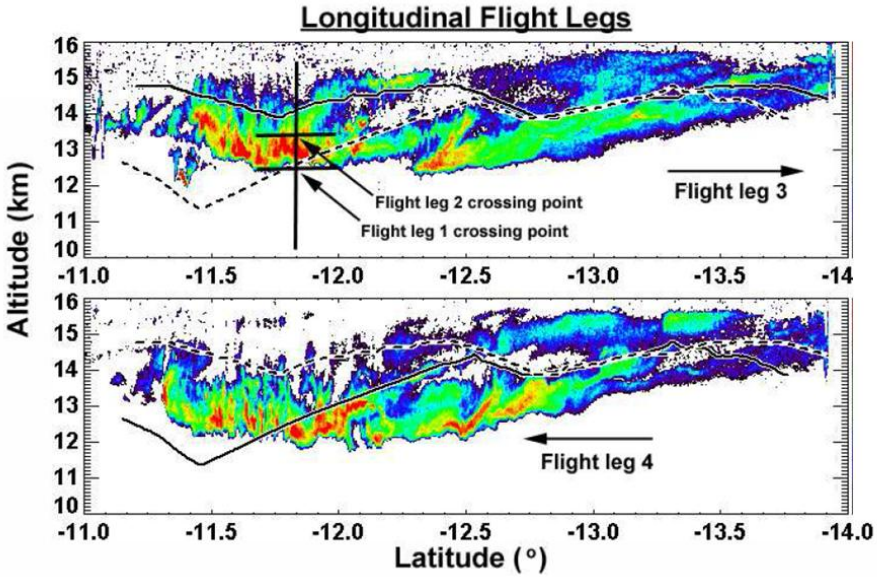

Figure 3.11: Contour plot of lidar backscatter contour from the anvil outflow cirrus cloud. Flight leg 3 was directed southward along the axis of the outflow away from the decayed convective core and flight leg 4 was back along the same ground path, toward the north. Solid lines represent the flight leg actively shown in the panel while dotted lines show where the other flight leg in the other direction occurred. Taken from Cook, 2004.

3.5 Analysis of Wave and Turbulence Fluctuations

Waves and turbulence were observed in the perturbations induced in measured quantities. The sampling frequency of the wind, temperature and pressure measurements was 25 Hz, which corresponds to a horizontal distance of 4 metres between samples at the typical maximum Egrett air speed of 100 m/s. This resolution is sufficient to resolve the spectrum of waves and turbulence with scales ranging from the length of the flight leg (typically 50 km or more) to less than 10 meters.

Perturbations from mean background values in velocity and potential temperature (u',v',w', θ') were calculated by fitting third order polynomial curves to segments of length of 5km that are successively shifted by 1 km. Through sensitivity studies with analytical experimentation, this averaging length was found to afford an optimal trade-off between preservation of variability and over-smoothing of data. The overlapping polynomial fits were averaged and smoothed to obtain a background atmospheric baseline. This smoothed, composite polynomial background curve was subtracted from the original measurements to yield local wind and temperature deviations. An example of the multiple polynomial fitting method (and computation of TKE) is illustrated in Fig. 3.12

From local wind perturbations u',v' and w', turbulence kinetic energy was then calculated according to;

$$TKE = \frac{1}{2}\left(\overline{u'^2 + v'^2 + w'^2}\right), \tag{3.1}$$

with averaging being performed over approximately 1 km. Other derived quantities include the momentum flux, estimated as

$$MF_u = (\overline{u'w'}),$$
$$MF_v = (\overline{v'w'}). \tag{3.2}$$

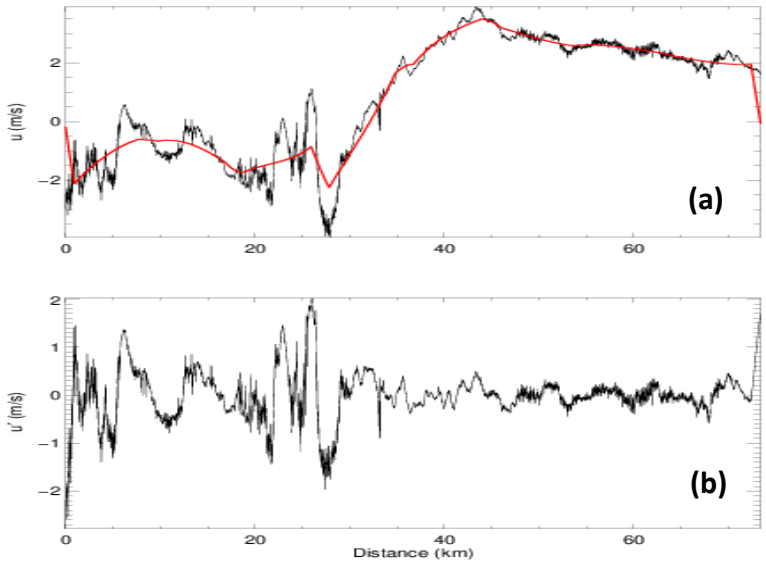

Figure 3.12: (a) example of overlapping third order polynomial fit to obtain perturbed quantities, specifically, zonal wind velocity, u'. The solid black line is the original measurements while the red line is the smoothed, composite polynomial background fit. (b) Perturbed zonal wind velocity (u') as calculated from measurements subtracted from the background fit.

Furthermore, Power Spectral Density (PSD) was computed as the square of the Fourier transform of the perturbed signal, normalized such that the signal variance equals the value of the integral over the spectrum (Parseval's theorem.)

3.6 Spectral Analysis

Spectral analysis of the measured perturbations was performed using the wavelet transform method. Wavelet analysis can be thought of as an extension of Fourier analysis. Wavelet analysis departs from Fourier analysis in that it employs slightly different basis function sets (other than sines and cosines) for signal decomposition. Selected wavelet phase analysis presented in Chapter 4 is utilized only as quantitative confirmation that observed phase shifts in fluctuating quantities such as wind velocity and potential temperature are consistent with those which can be estimated visually.

The software used for the wavelet analysis presented in this thesis is a modification of IDL programs generously made available by Dr. Christopher Torrence and Dr. Gilbert P. Compo on their wavelet analysis website[2]. A thorough demonstration of the original software as applied to climatological data set analysis is presented in Torrence and Compo, 1998. For a rigorous mathematical treatment and derivation of wavelets, the reader is directed to review a myriad of papers and textbooks on the subject such as Gabor, 1946; Morlet, 1983; Chui, 1992; Daubechies, 1992; Farge, 1992; Morlet; and Meyers et al., 1993.

Wavelet analysis was selected for use in this thesis over simple Fourier analysis due to its unique ability to graphically represent the differences between patterns in the data existing at local (i.e. perturbative) versus global (mean states prevailing over some

[2] Wavelet software was provided by C. Torrence and G. Compo, and is available at URL: http://paos.colorado.edu/research/wavelets/software.html .

averaging period) scales for potentially non-stationary processes (i.e. processes in which dominant frequency components may change significantly over time).

Figure 3.13 depicts the different time-frequency windows used in (a) a Fourier transform, (b) a windowed Fourier transform, and (c) a wavelet transform, respectively. Unlike the Fourier and windowed Fourier transforms, the wavelet time-frequency window is dynamic. The window is stretched and translated, i.e. "zoomed" over all values in the frequency-time domain (called the wavelet domain) to match the highest and lowest frequencies present in the signal, affording the production of a well resolved spectrum uncompromised due to scale extremes (eg. neither displaying numerous spuriously generated high frequency peaks nor a broadening of low frequency peaks.) This "zooming in" ability is particular to wavelet analysis and facilitates the localization of short lived, high frequency signals which may occur abruptly in time without the generation of spurious peaks while also efficiently resolving low frequency scale components (Lau and Weng, 1995.) In light of this fact, I have employed wavelet methods throughout Chapter 4 given that the data being investigated contains sharply delineated and / or high frequency features such as isolated waves (see Section 4.3) and rolls (see Section 4.5)

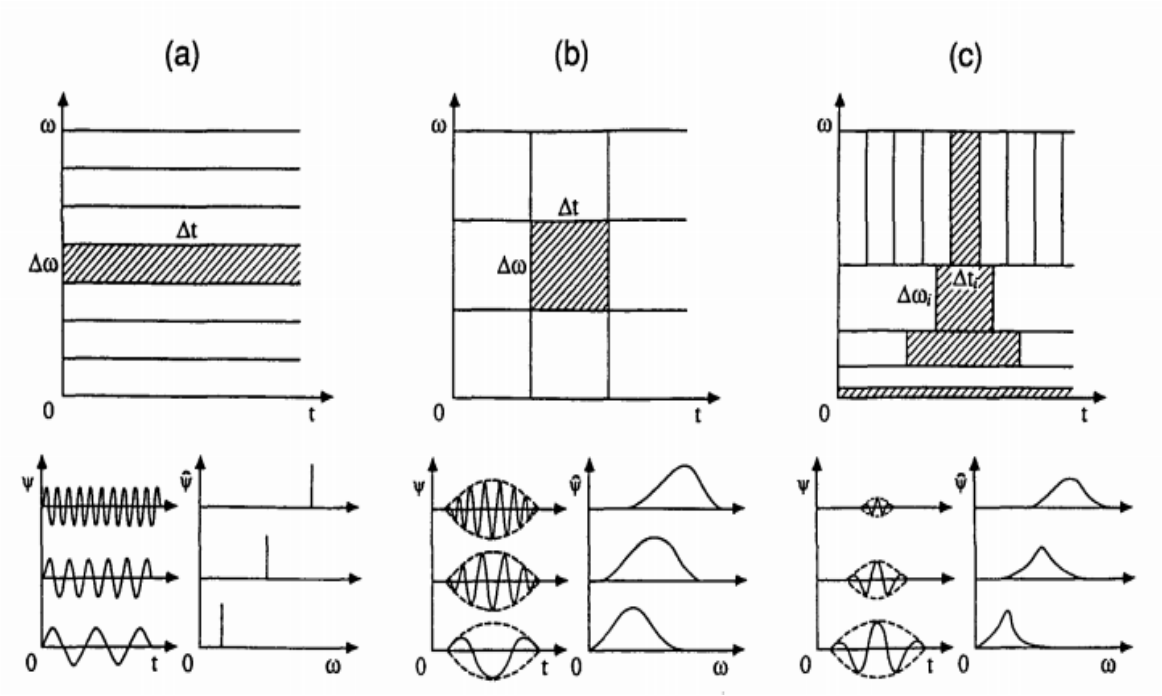

Figure 3.13: Different time frequency windows utilized in **(a).** a Fourier transform, **(b).** a windowed Fourier transform and **(c).** a wavelet transform. Taken from Lau and Weng, 1995.

Morlet wavelets are the most commonly used wavelet function in atmospheric data analysis (Woods & Smith, 2010.) The Morlet wavelet consists of a plane wave modulated by a Gaussian and is given by the expression

$$\psi(\tau) = \pi^{\frac{-1}{4}} e^{i\omega_0 \tau} e^{\frac{-\tau^2}{2}}, \tag{3.3}$$

in which τ is a non-dimensional, spatial parameter and ω_0 is a selected normalization factor.

Sensitivity studies were completed in order to gauge the most suitable wavelet function basis set with which to analyze the data presented in this thesis. Simulated

signals on which the performance of three different wavelet bases[3] were tested included the following;

- a wave field (sine waves) of wavelength 4km,
- a Rankine vortex of characteristic amplitude (about 1 m/s vertical velocity),
- single and multiple Rankine vortices within a wave field, and
- background Gaussian noise of varying intensity.

The continuous, complex valued Morlet wavelet was found to be capable of most narrowly pinpointing the dominant frequencies of a generated wave signature and of validly discerning highly localized phase difference relationships between multiple, generated waves. Consequently, Power Spectral Density (PSD) values presented in Chapter 4 have been calculated using the Morlet wavelet transform, normalized such that mother and daughter wavelets possess the same total energy and units are given in W^3/m^3.

[3] Bases considered for use were the Paul, Morlet and Degree Of Gaussian (DOG, commonly known as "Mexican Hat") wavelets.

Chapter 4: Data Analysis and Results

This Chapter presents the analysis of the measurement data as a series of case studies. Three main phenomena have been identified throughout the anvil outflow: (a) gravity waves, (b) Rayleigh-Bénard convective rolls, and (c) turbulence. The unique characteristics of the anvil dynamics are demonstrated by comparing the 2002 EMERALD-2 measurements to measurements taken with the same instruments (lidar, BAT probe) during the Aberystwyth Egrett Experiment (2000, see Pavelin, 2002) and the EMERALD-1 (2001, see Cook, 2004) campaign. Specifically, the Aberyswyth Egrett Experiment allows for comparison of tropical anvil outflow dynamics with dynamics occurring in mid-latitude jet stream turbulence (June 6, 2000) while the EMERALD-1 measurements were used for comparison with mid-latitude cirrus clouds (September 19, 2001.)

In this chapter, the detailed analysis of a single EMERALD-2 flight comprising of four flight legs (two transverse, two longitudinal) on November 23, 2002 is used to show how each phenomenon has been identified. For this research, a total of 13 flight days worth of data (constituting of order 100 flight legs) were analyzed. Instead of providing a purely statistical overview of the data, results have been presented as a series of case studies to best illustrate the variety of phenomena encountered and the process of analysis and identification of these phenomena in its entirety. After presentation of each November 23rd case, the general results from all EMERALD-2 flights are then described in terms of the three phenomena. Finally, a case study from December 2, 2002 is

presented to further illustrate the dynamics along the base of the outflow and put in perspective where each of the three main phenomena can occur in the outflow region.

Figure 4.1 illustrates the characteristic signals observed in the fluctuating vertical velocity (w') component of wind for each of the three phenomena: isolated waves, rolls and turbulence. Out of the approximately100 flight legs conducted, 33 instances of isolated waves were observed on eight separate days (out of a 13 total flight days). In the case studies presented in this chapter, the occurrence of one or more of these signals within the measurements indicates the presence of a coherent structure. Once the existence of a coherent structure is observed, it is then characterized in terms of phase relationships between fluctuations in variables such as potential temperature (θ') and wind velocity (u',v',w'.)

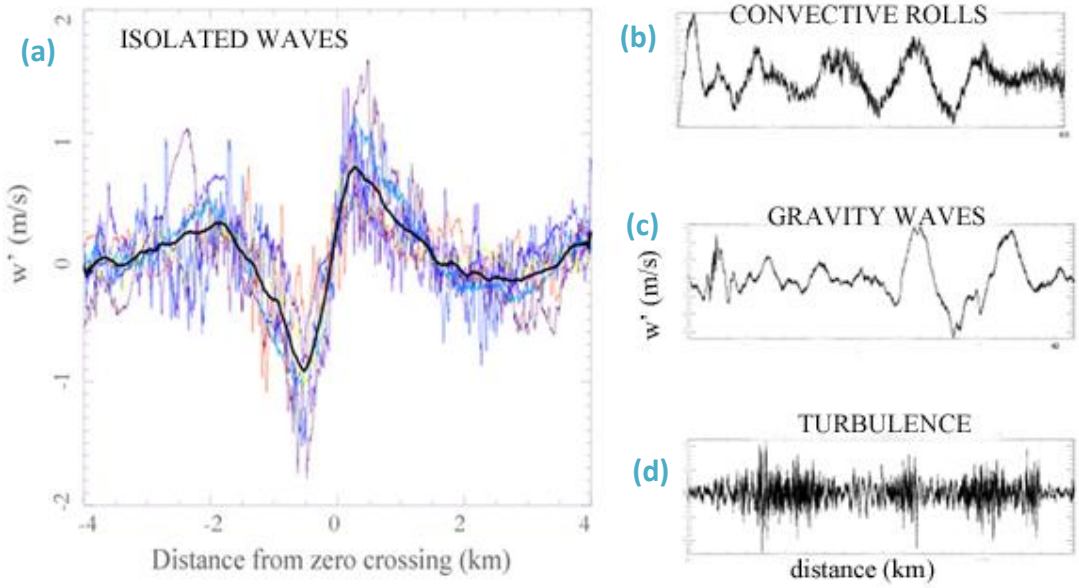

Figure 4.1: Example of coherent structures found in cirrus anvil outflow **(a)** isolated waves: the coloured lines represent actual isolated wave measurements in fluctuation in vertical velocity from eight different flight legs conducted over 13 flight days, showing the robustness of the data collected throughout the campaign. The black line is the averaged, zero aligned (i.e. to the point of x-axis zero-crossing) signal. **(b)** Rayleigh-Benard convective rolls, **(c)** extended waves, and **(d)** turbulence from flight leg 1, Nov. 23, 2002, designated a7r3_391 where the naming convention is as follows: a = day number (up to a total of 13) r = run number on that day, last three digits = internal distance / time index.

4.1 November 23rd, Flight Leg 1: Waves and Rolls across the Outflow

The overall experimental plan and flight path from November 23, 2002 were described in Section 3.4.1. Flight leg 1 was oriented transverse to the anvil outflow at an altitude of approximately 12.6 km. Flight direction was from east to west, spanning approximate longitudes of 130.8° - 129.6°. Figure 4.2 shows the combination of the lidar remote sensing and in situ vertical wind measurements for flight leg 1 on 23 Nov. 2002. A

contour graph of the photon counting signal returned from the vertically profiling lidar backscatter measurements from the King Air aircraft outlines the anvil cloud base. The lidar signal is rapidly attenuated immediately above the cloud base due to the large optical thickness within the cloud but the anvil cloud extends up to a height of about 15.5 km in this case. The red line in Fig 4.2 displays the Egrett flight track for flight leg 1, and this is used as the zero reference for the vertical wind measurements (white line). This provides a view of the spatial distribution of coherent structures relative to the geometry of the anvil outflow.

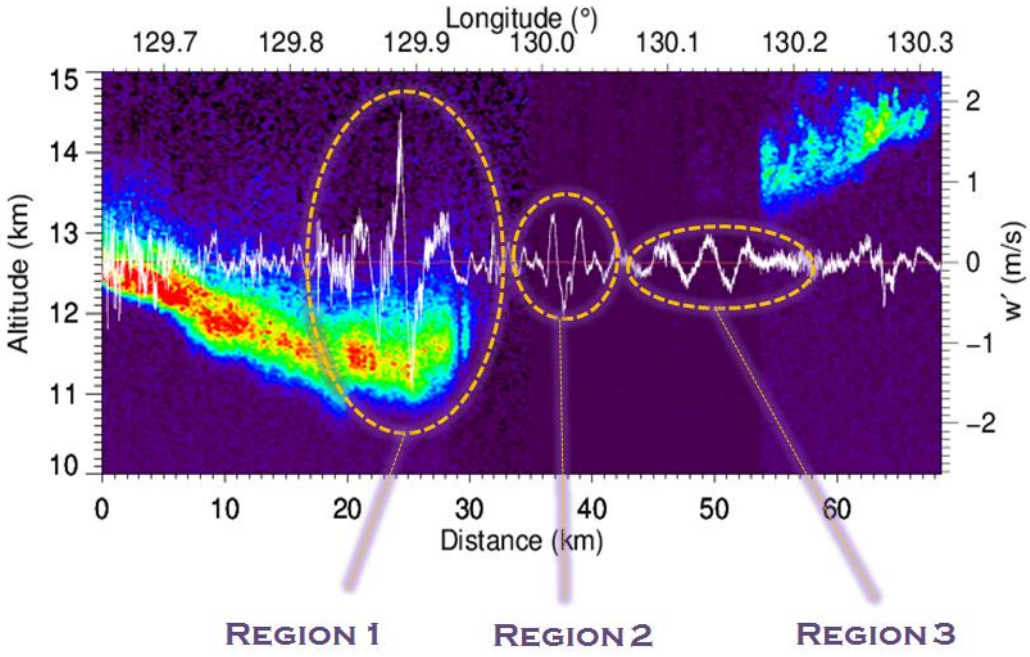

Figure 4.2: Contour of lidar backscatter signal showing the cloud base across the cirrus anvil outflow for flight leg 1 (a7r1_391) on 23 Nov. 2002. The red horizontal line shows the Egrett's flight path (at altitude ~12.4 km) and serves as an x-axis for the overlaid display of in situ vertical velocity measurements (white.) Three regions of interest are circled and labelled.

Three coherent features of interest have been observed for this flight leg. The features were identified as: Region 1: isolated wave, Region 2: gravity wave, Region 3: Rayleigh-Bénard convection rolls. Gravity waves and convection rolls have been discussed in Chapter 2. Sections 2.4 and 2.5 describe expected phase relations between temperature and wind velocity, allowing for one to distinguish between the coherent structures as waves or rolls. Figure 4.3 again displays the three regions in flight leg 1 (without the lidar backscatter contour plot) while presenting simultaneous measurements of potential temperature and wind velocity fluctuation along the flight track in order to gauge phase relationships.

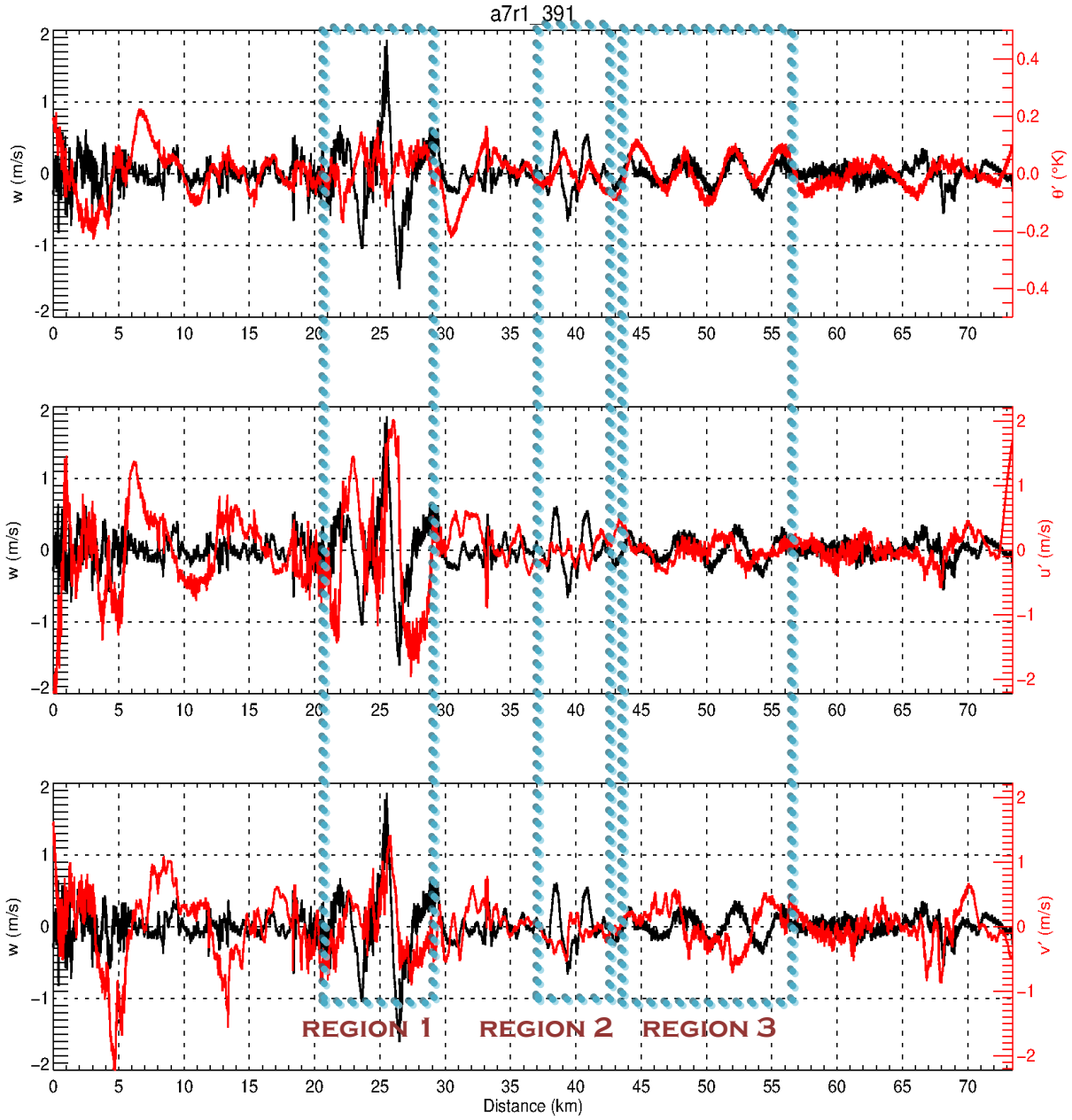

Figure 4.3: Perturbation wind velocities & perturbation potential temperature signals with distance along flight track (km) for flight leg 1 (a7r1_391) with three highlighted regions showing coherent structures of interest. Y-axes on left (black) denotes values of perturbation vertical velocity while y-axes in right (red) denote perturbed quantities of theta, u and v, from top to bottom, respectively.

The phase difference between fluctuations in vertical wind velocity and potential temperature is not consistent across the flight leg. While some phase relationships are visually evident from the measurements alone, others are more complicated due to superposition and the interplay of multiple dynamical processes potentially occurring within the flight leg. For this reason, wavelet spectral analysis was performed in order to provide an alternate view of the measurements and a more objective method to ascertain the relationship between fluctuations in temperature and wind.

A demonstration of analysis by wavelet methods is presented for flight leg 1 (see Section 4.6). Full wavelet figures of other flight legs have been omitted with the exception of selected wavelet spectra derived phase difference contour plots for w' and θ'. These plots are presented when necessary along with the original w' and θ' measurements for the purpose of empirically distinguishing between waves, rolls and turbulence.

4.2 Isolated Waves in Flight Leg 1

Figures. 4.2 and 4.3 reveal a striking wave pattern in vertical velocity localized around 25 km from the start of flight leg 1. The resulting signal is reminiscent of a breaking mountain wave (see Section 2.4.4) Figure 4.4 shows a comparison of EMERALD-2 data with in situ measurements of vertical velocity from one such breaking

mountain wave observed over Wales during the Aberystwyth Egrett Experiment. On an east-west oriented flight leg undertaken on May 11, 2000 at an altitude of approximately 10.5 km, the distinctive cliff ramp structure indicative of wave overturning is clearly visible.

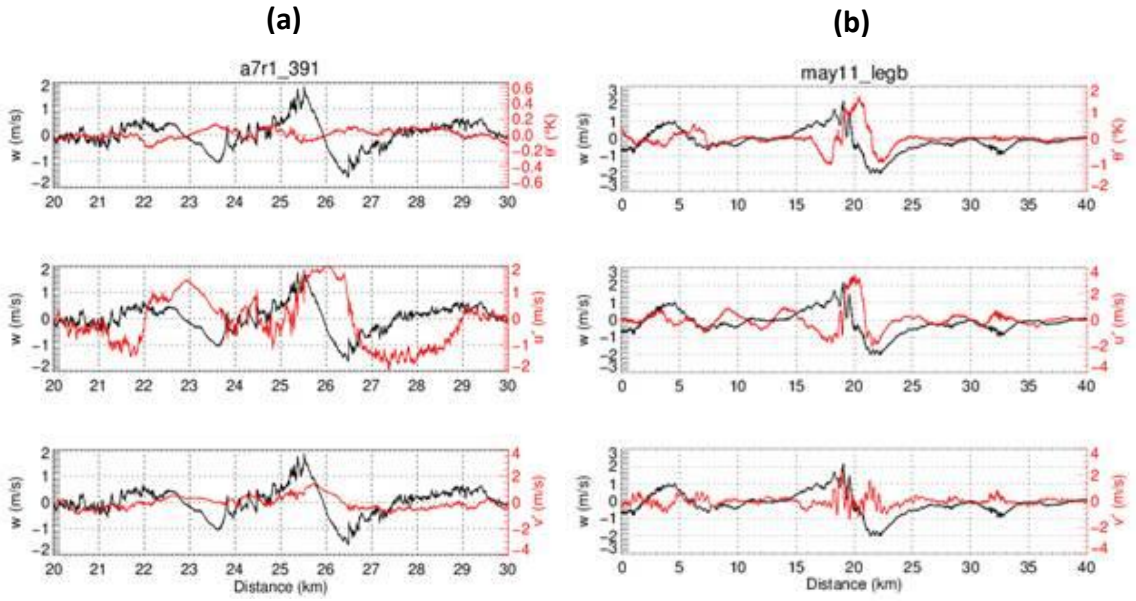

Figure 4.4: (a) measurements of vertical wind, potential temperature and horizontal wind for flight leg 1 of the Emerald 2 campaign, November 23, 2002. **(b)** In situ Egrett measurements of vertical wind compared with fluctuations in potential temperature and horizontal wind velocity for breaking gravity wave observed on May 11, 2000 during the Aberystwyth Egrett Experiment. Egrett altitude is ~10.5 km.

Both May 11 (Fig. 4.4(b)) and November 23 (Fig.4.4(a)) flight legs display analogous, nearly identical cliff regions between 15.5 km – 25.5 km and 25.5 km –26.5 km, respectively, where the wave is attaining maximum amplitude prior to overturning. Because its scale is set by the underlying topography, the mountain wave is seen to be approximately a factor of five times longer in wavelength than the wave observed in the anvil outflow.

The comparison is strongest in the relationship between perturbations in the vertical and horizontal wind velocities. It is seen that in both the May 11 mountain wave and the November 23 anvil outflow isolated wave that a peak in the zonal wind perturbation occurs at the zero crossing in the vertical wind. This is where the vertical displacement is greatest and thus the displacement of horizontal wind shear causes a peak in the perturbation horizontal wind. The wave induced wind perturbation amplitude is therefore difficult to separate from the displacement of vertical shear.

The phase difference between horizontal and vertical wind perturbations is expected to be either 0^o or 180^o for a vertically propagating gravity wave (Section 2.3). The horizontal wind perturbation due to the wind shear advection would have a 90^o or 270^o phase difference from the wave induced vertical wind perturbation. A rough method to obtain the wave induced horizontal wind perturbation amplitude is to take the value at the peak of the vertical wind perturbation. At this point, the vertical displacement due to the wave is zero, so there should be no wind shear effect.

For the Nov. 23 case in Fig 4.4(b), the vertical wind perturbation peak amplitude is 1.4 m/s. The two components of the horizontal wind perturbation are approximately 1.0 m/s at the position of the peak vertical wind. The total horizontal wind perturbation amplitude can then be approximated as $(u^2 + v^2)^{½} = 1.4$ m/s. The ratio of horizontal to vertical wavenumber is then, according to Equation (2.26),

$$\frac{k}{m} = \frac{w'}{u'} = \frac{1.4}{1.4} = 1.$$

(4.1)

The ratio of the wave frequency to the buoyancy frequency from Equation 2.27 is estimated to be

$$\frac{\omega}{N} = \frac{k}{\sqrt{k^2 + m^2}} = 0.71. \tag{4.2}$$

From Equation 2.16, the wave induced perturbations are directed along the phase lines which are tilted at an angle of

$$\psi = \cos^{-1}\left(\frac{\omega}{N}\right) = 45^\circ. \tag{4.3}$$

With the horizontal and vertical wind perturbations being of the same sign, the horizontal and vertical wave numbers are the same sign, and the direction of wave group propagation is either up and to the northeast, or, down and southwest.

The comparison is not so obvious in terms of the relationship between vertical wind and temperature perturbation. In the mountain wave case of May 11, 2000 (Fig 4.4(b)), the peak temperature perturbation occurs at the zero crossing in the vertical wind (maximum displacement) as expected. In the EMERALD-2 isolated wave case of November 23, 2002, there is no such obvious relationship between potential temperature

perturbations and vertical wind. This is interpreted as being a result of wave breaking/overturning. Based on the ramp cliff structure from distances of 23 km to 27 km, the EMERALD-2 case is interpreted as a breaking gravity wave. The ramp section from 23.5 km to 25.5 km is where the wave would be overturning. In such a scenario, the expected relationship between vertical wind and temperature perturbations (see Section 2.4.6) would not be straightforward. Additional analysis of other observed isolated waves in anvil outflow is provided in Section 4.3, showing that the relationship between vertical wind and temperature perturbation was typically similar to mountain waves.

In Region 2 of flight leg 1 on November 23, 2002 (distances between 37 km and 42 km in Fig. 4.3,) two clear peaks of a wave pattern are observed with a wavelength of approximately 2.4 km. An expanded view of the perturbations in wind and temperature measured in this section of the flight is shown in Fig. 4.5. In this case there is clearly a 90^{o} phase shift between the wave induced perturbations in vertical wind and temperature. The peaks in the temperature perturbation occur at the zero crossing of the vertical wind. As was discussed in Chapter 2 (Sec. 2.4.6), this is consistent with a gravity wave. The perturbations in the horizontal wind components are not directly correlated with the vertical wind. There is no significant amplitude in the horizontal wind at the wavelength in the vertical wind (2.4 km). According to Equation 2.26 of Chapter 2, if the horizontal wind fluctuation amplitude is zero, then the vertical wavenumber is zero, and the wave frequency is equal to the Buoyancy frequency (Brunt-Väisälä frequency.) The wave perturbation motions are along phase lines that are not tilted from the vertical. This is a pure buoyancy wave with displacements only in the vertical direction.

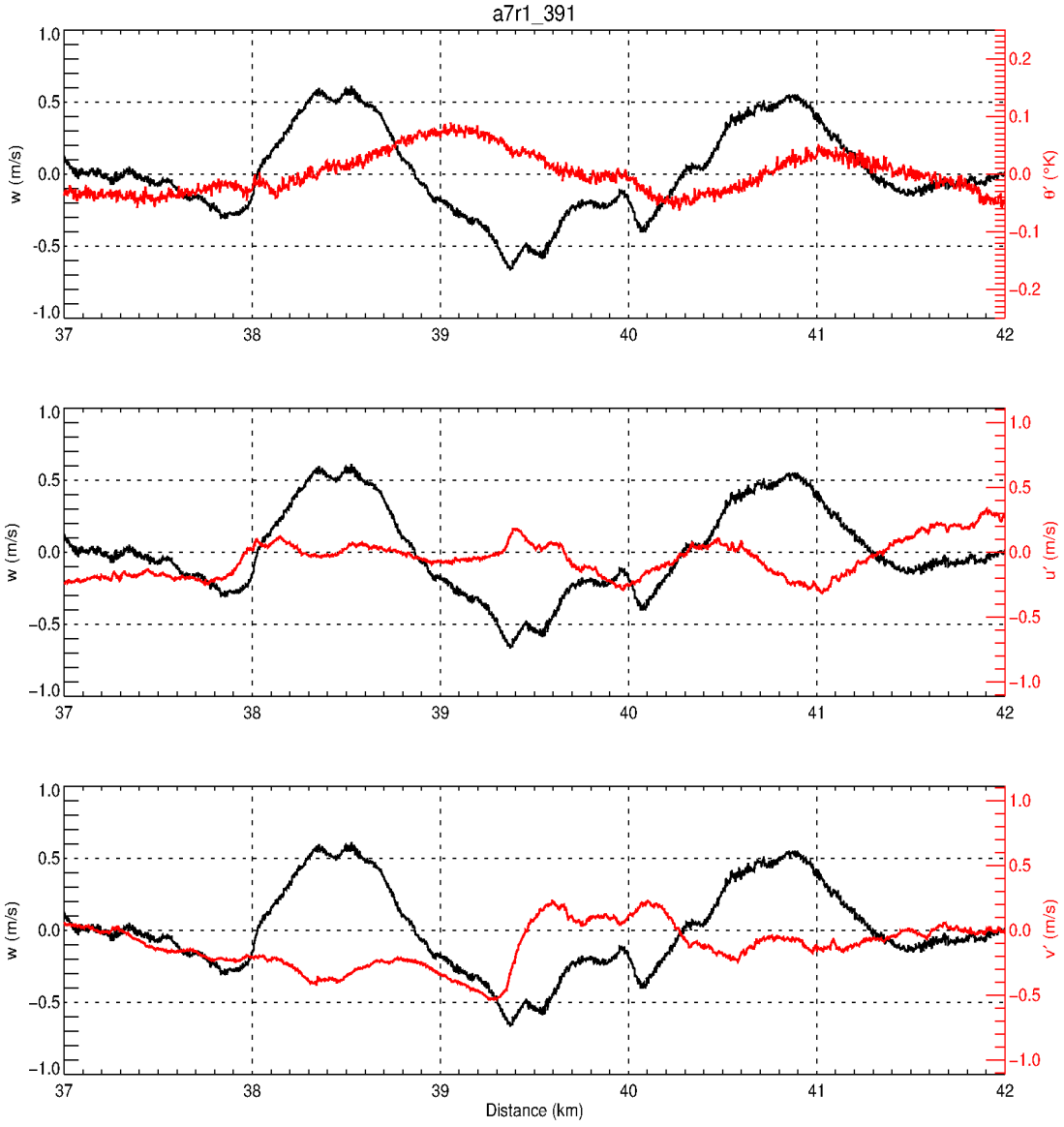

Figure 4.5: Detail of region 2 (37 km -42 km) of 23 Nov. Flight leg 1 (a7r1_391.) Fluctuations of vertical velocity (black) are over plotted against, from top to bottom, fluctuations in potential temperature, zonal, and meridional wind velocities.

4.3 General Analysis of Isolated Waves

In the more than one hundred flight legs conducted for EMERALD 2 over thirteen days, isolated wave signatures in vertical velocity were observed in many of the Egrett's transverse runs. Figures 4.6 to 4.9 present a selection of some of the clearest isolated waves that were most easily distinguished from the turbulent background. Details of specific flight days and legs analyzed, including the distance range throughout which the isolated waves were observed are given in Table 4.1. The observed wave parameters and derived wave frequency relative to the buoyancy frequency (ω/N) are listed in Table 4.2. The determination of wave frequency follows the analysis carried out in the previous section (Sec. 4.2) for the November 23rd case.

In the eleven cases listed, the horizontal wavelength projected along the flight direction varied in the range of 1.0 km to 2.9 km. The vertical wind amplitude was in the range of 0.5 m/s to 1.4 m/s. Three of the six cases had a vertical wind amplitude of 1.0 m/s. The horizontal wind amplitude has a significant uncertainty due to the vertical advection of wind shear by the wave. The approximate values were in the range of 0 m/s to 2.0 m/s. The wave frequency derived from the ratio of vertical to horizontal wind amplitudes ranged from $\omega/N = 0.45$ to $\omega/N = 1$. In three out of six cases the wave frequency was essentially equal to the Brunt-Väisälä frequency and accordingly, the waves would be vertical buoyancy oscillations.

Table 4.1: Properties of selected transverse flight legs exhibiting distinct isolated wave signatures.

EM 2 Leg Designation	Altitude (km)	Length (km)	Region of Interest (km)
Nov. 13: a2n1_400	12.92	139.93	95-105
Nov. 15: a3n2_448	14.43	158.91	65-75
Nov. 21: a5up1_cc	9.84	83.72	42-50
Nov. 21: a5r1_301	9.72	114.46	44.5-47.5
Nov. 21: a5dn1	4.56	80.58	13-21
Nov. 22: a6r3_381	12.31	80.21	15-21
Nov. 22: a6r5_updn	14.63	30.01	0-2
Nov. 22: a6r6_447	14.45	47.67	16-21
Nov. 23: a7r1_391	12.64	73.43	22-29
Dec. 2: a13r5_230	7.44	66.36	26-32
Dec. 2: a13r6_216a	6.96	38.33	31-37

Table 4.2: Basic properties in isolated waves encountered during EMERALD 2.

EM 2 Leg Designation	λ_x (km)	w (m/s)	$(u^2 + v^2)^{1/2}$ (m/s)	ω/N
Nov. 13: a2n1_400	2.7	0.6	0	1
Nov. 15: a3n2_448	3.6	0.9	0.7	0.79
Nov. 21: a5up1_cc	3.0	0.9	4.03	0.98
Nov. 21: a5r1_301	1.0	1.0	2.0	0.45
Nov. 22: a6r3_381	2.2	1.0	0.7	0.58
Nov. 22:a6r5_updn	1.5	1.2	1.6	0.75
Nov. 22: a6r6_447	2.1	1.0	0.3	0.81
Nov. 23: a7r1_391 (a)	2.9	1.4	1.4	0.71
Nov. 23: a7r1_391 (b)	2.4	0.5	0	1
Dec. 2: a13r5_230	2.3	1.5	2.83	0.71
Dec. 2: a13r6_216a	4.8	0.9	1.39	1

With the exception of the previously presented isolated wave case on November 23 (Sec. 4.2) where phase relations are not straightforward (interpreted as wave breaking), all isolated wave cases considered herein display a 90^o phase shift between fluctuation in vertical velocity and potential temperature. This is illustrated in Figures 4.6 – 4.9 which present a series of composite plots for each isolated wave example. Each figure shows the vertical wind perturbation velocity over-plotted against potential temperature, zonal

and meridional velocities. In each case, a wavelet co-spectral analysis indicates that the phase difference between vertical wind and temperature perturbations was approximately 90° at the relevant wavelength and position. Further wavelet analysis is presented and discussed in detail later in this chapter in Section 4.6

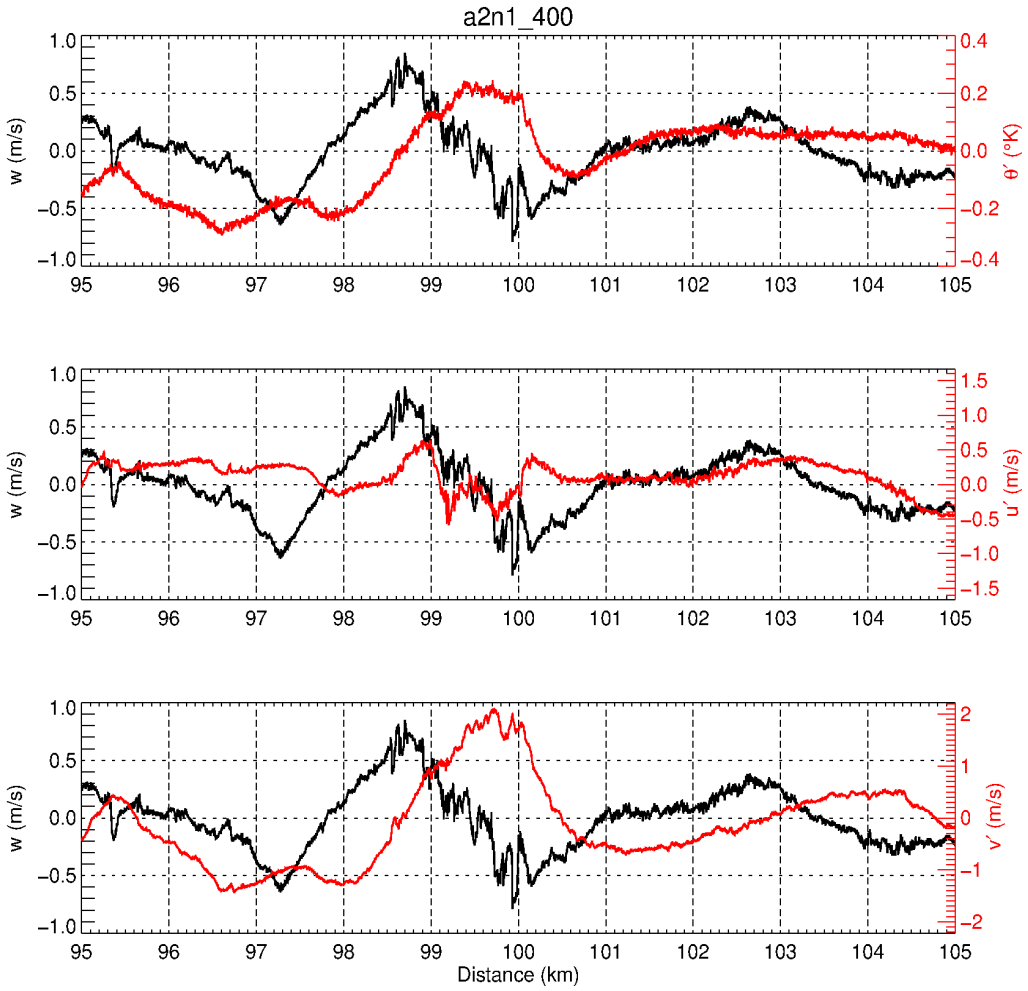

Figure 4.6: Fluctuations of vertical velocity (black) are over plotted against, from top to bottom, fluctuations in potential temperature, zonal, and meridional wind velocities for transverse flight leg a2n1_400 on 13 Nov., 2002.

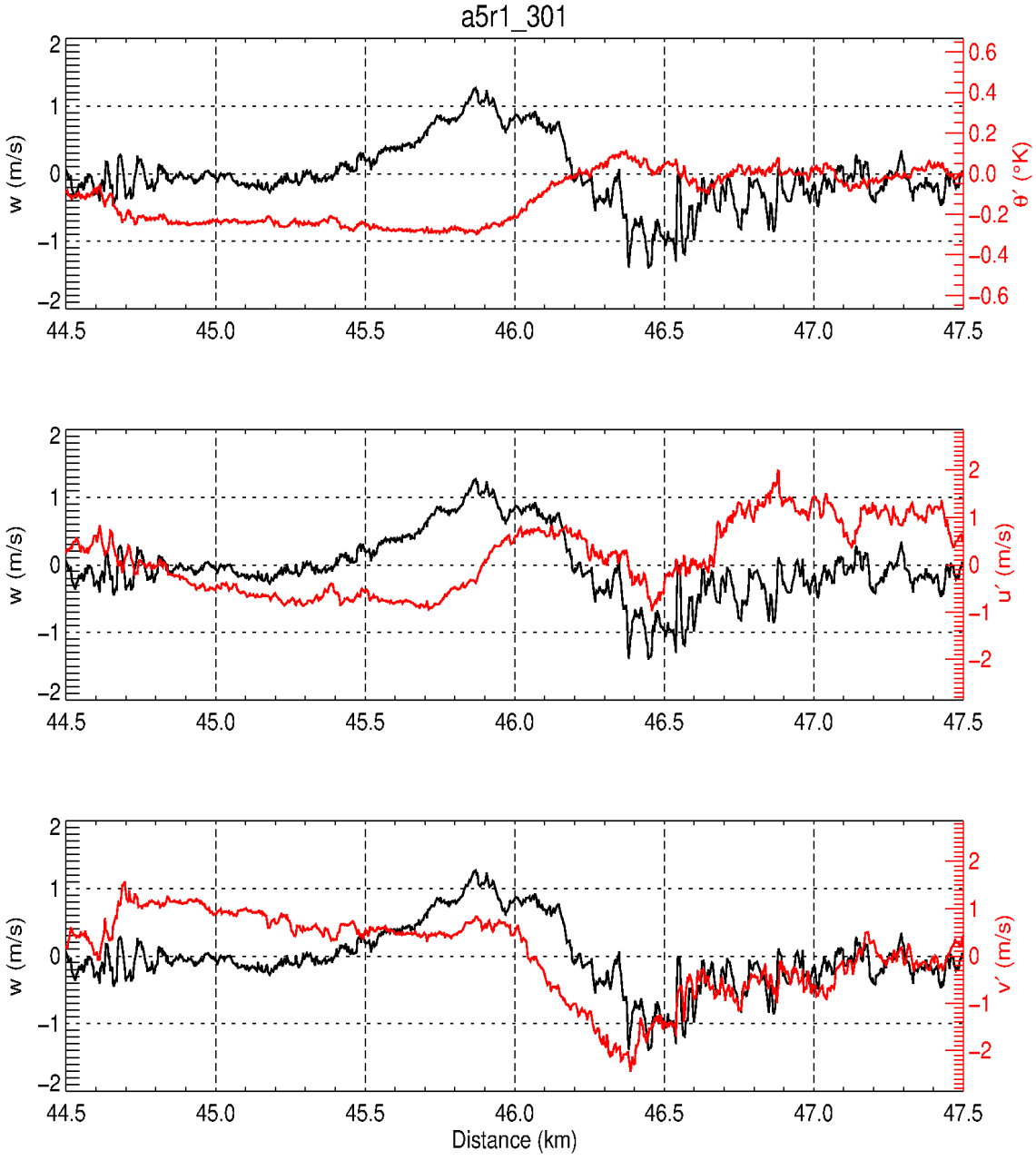

Figure 4.7: Fluctuations of vertical velocity (black) are over plotted against, from top to bottom, fluctuations in potential temperature, zonal, and meridional wind velocities for transverse flight leg a5r1_301 on 21 Nov. 2002.

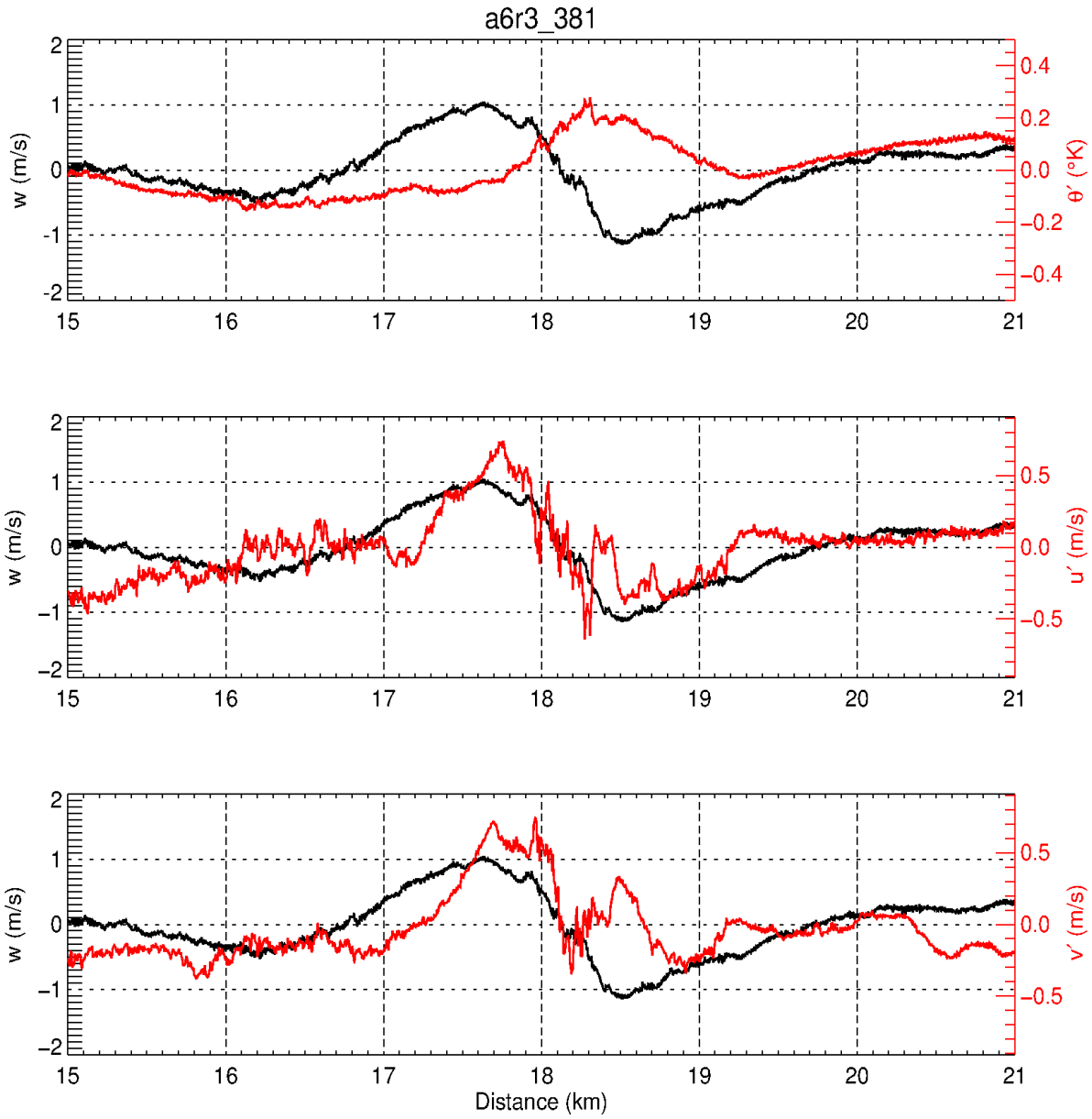

Figure 4.8: Fluctuations of vertical velocity (black) are over plotted against, from top to bottom, fluctuations in potential temperature, zonal, and meridional wind velocities for transverse flight leg a6r3_381 on 22 Nov., 2002.

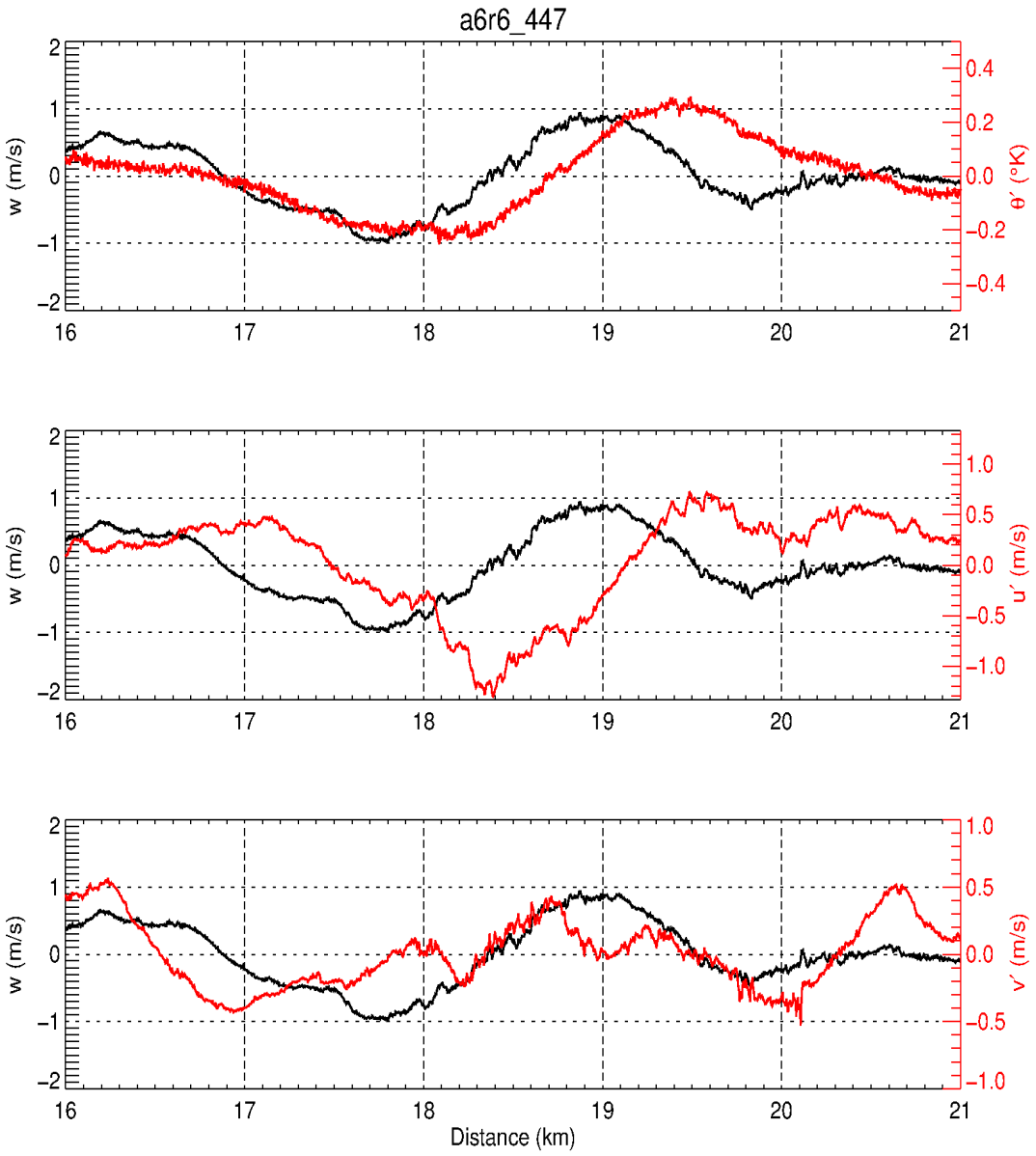

Figure 4.9: Fluctuations of vertical velocity (black) are over plotted against, from top to bottom, fluctuations in potential temperature, zonal, and meridional wind velocities for transverse flight leg a6r6_447 on 22 Nov., 2002.

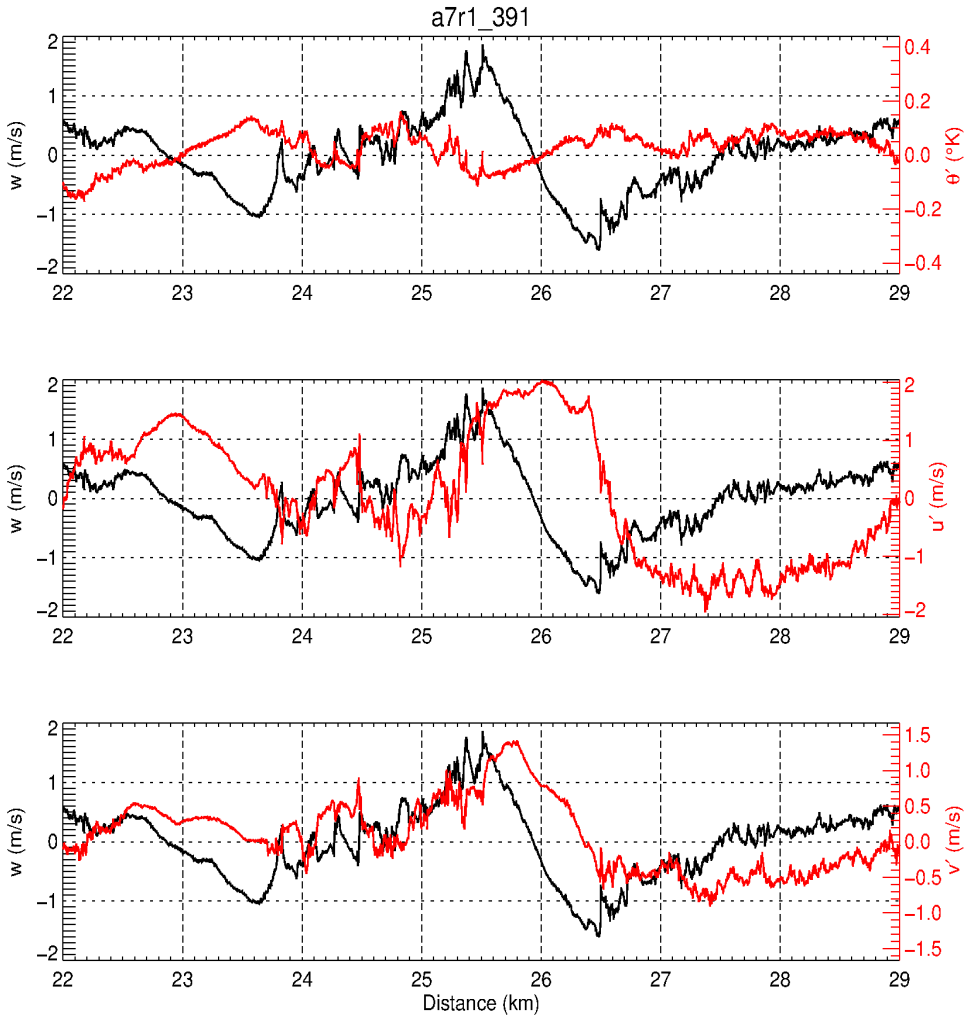

Figure 4.10: Fluctuations of vertical velocity (black) are over plotted against, from top to bottom, fluctuations in potential temperature, zonal, and meridional wind velocities for transverse flight leg a7r1_391 on 23 Nov., 2002.

A series of papers authored by T.P. Lane et al. (eg. Lane, Reeder and Clark, 2001; Lane et al., 2003; Lane, 2008; Lane and Moncrieff, 2008) present numerical simulations of convectively generated gravity waves. While the simulations conducted are for the most part focussed on larger scale, stratospheric gravity waves, there exists some overlap in

properties between the isolated waves presented in this thesis and the broad spectra of waves produced in the simulations by Lane et al. Fig. 4.11 (Lane et al., 2001) shows a distribution of intrinsic frequency (ω) over horizontal wavenumber (k). The region which coincides with isolated waves reported upon in this chapter is highlighted in red.

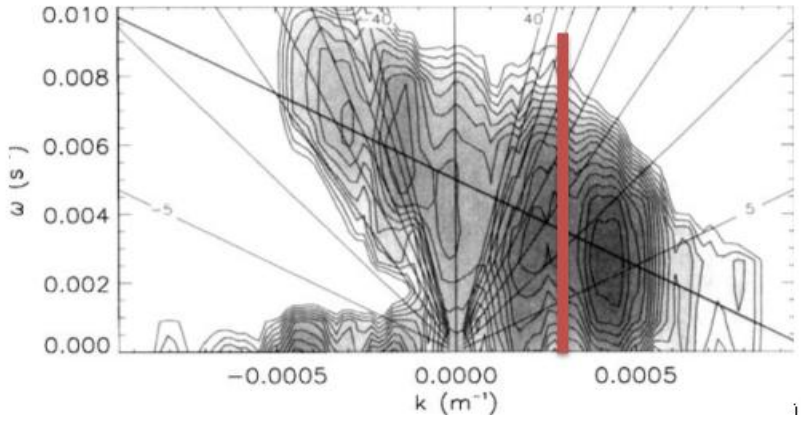

Figure 4.11: horizontal wavenumber spectrum from Lane et al, 2001. Red line marks the range in which isolated wave observations fall. The spectrum is normalized with logarithmic contours. Only the largest 1.5 orders of magnitude are shown. Darker contours represent higher spectral power while lighter contours represent lower spectral power. Contours of horizontal phase speed at c=5 m/s contour interval are also shown.

4.4 Extended Waves and Rayleigh-Bénard Convective Rolls in Flight Leg 1

There was a third waveform encountered in the Nov 23 flight leg shown in Fig 4.3 and this was identified as Region 3. An expanded view of Region 3 is shown in Fig 4.10. Here, there is clearly a wave pattern in the perturbations of wind and temperature. In this case, the perturbations of vertical wind and temperature are in phase. Section 2.5 illustrated that this is consistent with rolls associated with Rayleigh-Bénard convection.

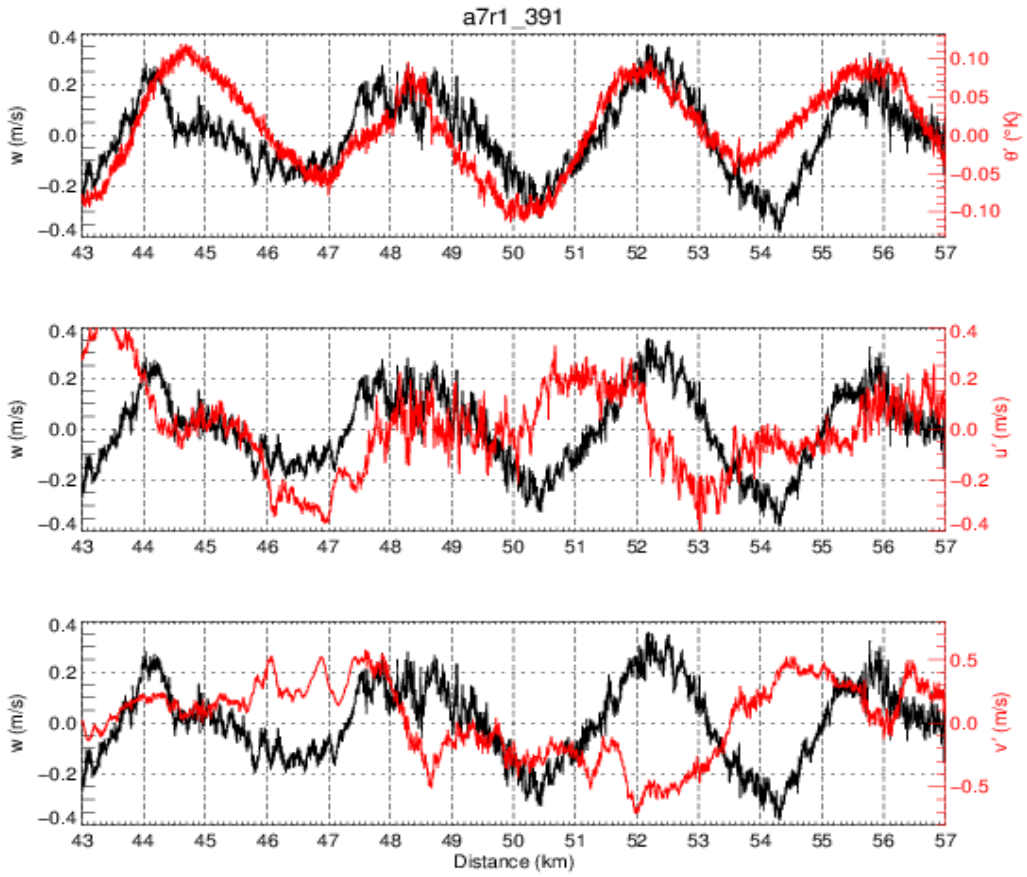

Figure 4.12: Detail of region 3 (43 km - 57 km) of 23 Nov. Flight leg 1 (a7r1_391.) Fluctuations of vertical velocity (black) are over plotted against, from top to bottom, fluctuations in potential temperature, zonal, and meridional wind velocities.

Rolls would be aligned north-south, parallel with the direction of the outflow and the orientation of the vertical shear. If the aircraft did not pass though the centre of the rolls then there would be perturbations in the horizontal wind, mainly in the east-west direction (the u' component). It is seen that this is the case in Fig 4.12. It is also expected that for rolls, the maxima in the horizontal wind perturbation would coincide approximately with the zero perturbation in vertical wind and this is the case at distances

of 50 km to 54 km along the flight track. The wavelength of 4 km in the vertical wind perturbation corresponds to a diameter of 2 km for the rolls.

4.5 General Analysis of Convective Rolls

In this section, I present four of the clearest examples of convective rolls from the entirety of flight legs of the EMERALD-2 campaign. As detailed in Section 2.5, for a convectively overturning roll or vortex type motion, it is expected that vertical velocity and temperature fluctuations will be in phase. Table 4.3 presents flight leg properties and details for the selected roll cases along with a region of interest in which extended wave-like coherent structures appear. In order to distinguish between rolls and waves, phase analysis is employed.

Table 4.3: Properties of selected transverse flight legs exhibiting distinct signatures of Rayleigh-Bénard convection (rolls).

EM 2 Leg Designation	Date (2002)	Altitude (km)	Region of Interest (km)	Wavelength (km)	Roll Diameter (km)
a2n1_400	Nov. 13	12.92	0-60	5.0	2.5
a2n2_448	Nov. 13	14.43	0-60	4.0	2.0
a6r1_391	Nov. 23	12.64	43-57	4.0	2.0
a8n1_302	Nov. 25	9.78	25-45	3.0	1.5

As in Section 4.3, Figs 4.13-4.15 present a comparison of fluctuations in horizontal wind and potential temperature with fluctuation in vertical velocity.

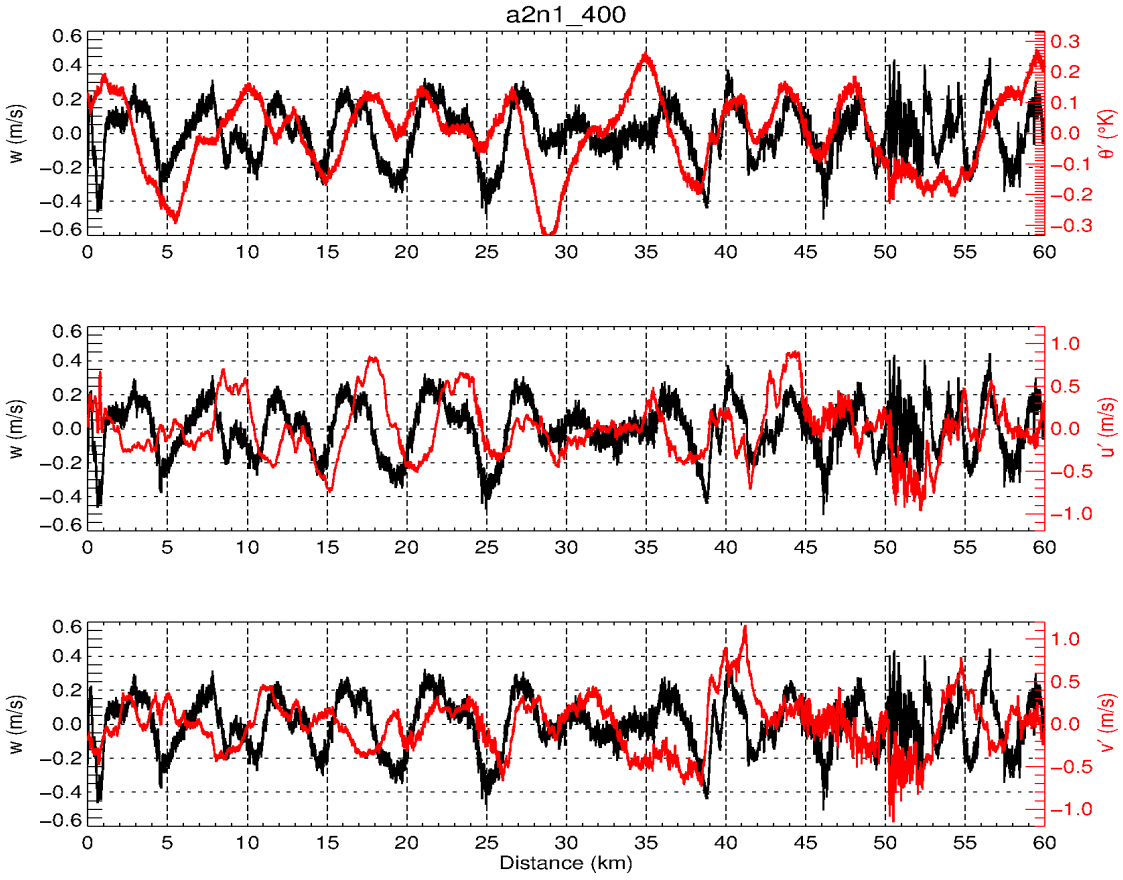

Figure 4.13: Fluctuations of vertical velocity (black) are over plotted against, from top to bottom, fluctuations in potential temperature, zonal, and meridional wind velocities for transverse flight leg a2n1_400 on 13 Nov., 2002. w' and θ' are indicative of rolls (in phase) between 40km – 50km.

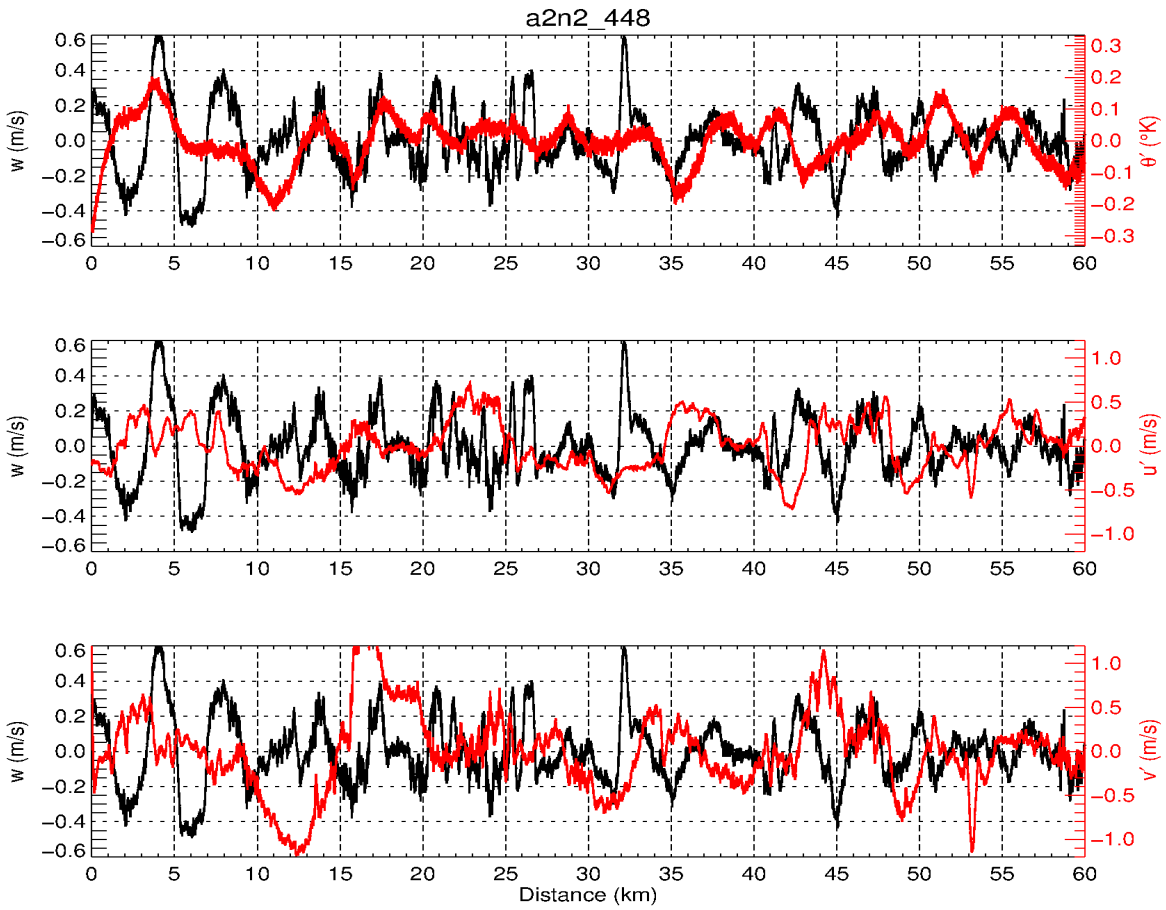

Figure 4.14: Fluctuations of vertical velocity (black) are over plotted against, from top to bottom, fluctuations in potential temperature, zonal, and meridional wind velocities for transverse flight leg a2n2_448 on 13 Nov., 2002. w' and θ' are indicative of rolls (in phase) between ~15km – 21km.

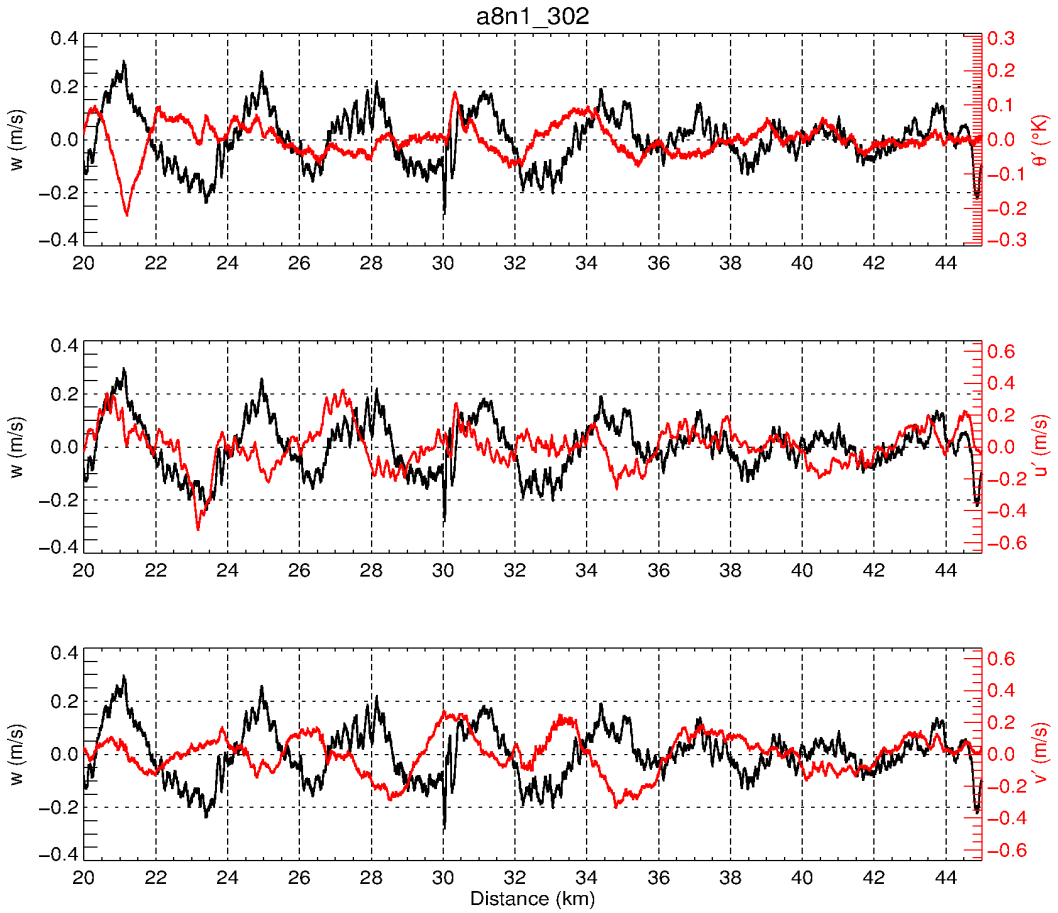

Figure 4.15: Fluctuations of vertical velocity (black) are over plotted against, from top to bottom, fluctuations in potential temperature, zonal, and meridional wind velocities for transverse flight leg a2n2_448 on 13 Nov., 2002. w' and θ' are indicative of rolls (in phase) between ~25km – 45km.

In Figs. 4-13 – 4.15, it is apparent that the phase relations between θ' and w' are not always consistent across larger distances. For instance, in Fig. 4.13, phase is offset by 90° between distances from approximately 8 km -20 km, whereas a 0° phase shift is apparent between 30 km - 40 km. Similarly, in Fig. 4.14, the phase shift is 0° between 14 km- 20 km and 90° between 42 km - 52 km. Finally, Fig. 4.15 is more difficult to

distinguish, appearing to display a 90^{o} phase shift between distances of 28 km – 36 km, while displaying no phase shift between approximately 39 km - 43 km.

4.6 Wavelet Analysis of Coherent Structures

In this subsection, I present a sample result from the wavelet based spectral analysis method used to interpret measurements contained within this chapter. The four panel wavelet analysis shown in Figure 4.16 from top to bottom, displays: (a) the original time series measurements, (b) the Morlet wavelet power spectral density as distributed over the wavelet domain, (c) cospectral power for fluctuations in vertical velocity and potential temperature, and, (d) phase difference analysis between fluctuations in vertical velocity and potential temperature.

This kind of wavelet analysis was performed for multiple legs on EMERALD-2 flight days of November 19,21,22,23,25 and December 1 and 2. While the wave parameters and phase relations were readily apparent in the line plots for the measurements of flight leg 1 of Nov. 23rd , spectral analysis via wavelet methods proved advantageous for interpreting dynamical cases in which phase relations were not readily evident such as where there was a mix of intense turbulence and coherent structures.

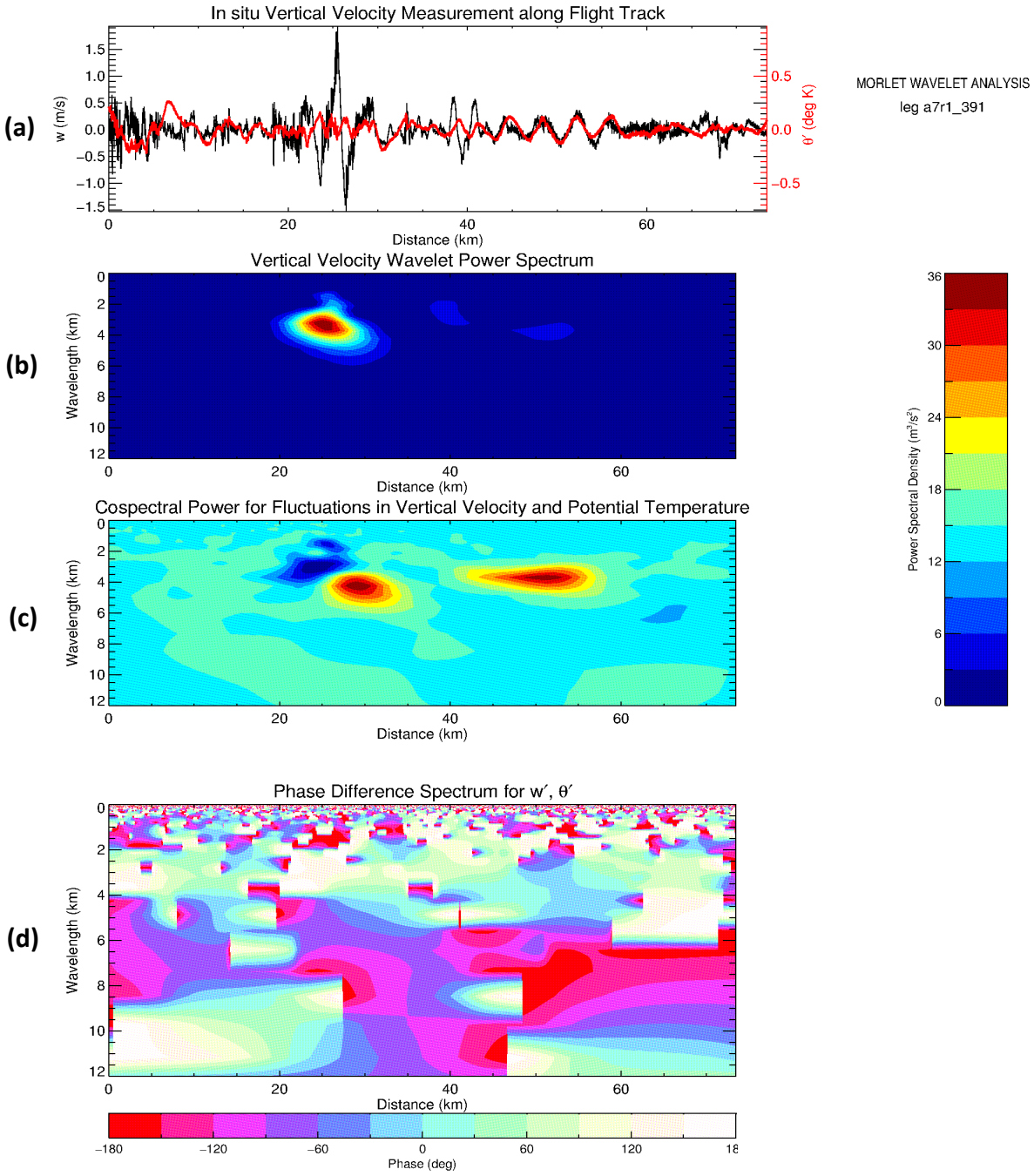

Figure 4.16: Morlet wavelet analysis panel for flight leg 1, Nov 23, 2002. **(a)** fluctuations in vertical velocity (w') as measured along the flight track. **(b)** wavelet domain showing the wavelet transform of fluctuation in vertical velocity, **(c)** cospectral wavelet analysis between w' and θ', and **(d)** wavelet based phase difference analysis between w' and θ'.

The wavelet analysis in Fig. 4.16 was performed for the entirety of flight leg 1 and shows the wavelet transform taken over the entire flight leg. Given that all EMERALD-2 flight legs were sufficiently long compared to the length of the individual coherent features being investigated within them, the traditional "Cone of Influence", or COI, typically shown on wavelet diagrams to indicate regions in which the power spectrum may be distorted due to edge effects is not included. While the COI was calculated, for the purposes of this research where wavelengths and phase relations are apparent upon visual inspection, the COI did not need to be rigorously considered and the wavelet phase diagrams displayed in this chapter are being used only as a confirmation tool.

Maximum contours in Fig. 4.16(b) corresponding to the appearance of the isolated wave at a distance of 25 km along the flight track reveal that power is concentrated between wavelengths of 2 km – 4 km with maximum power spectral density (PSD) in the vertical wind spectrum having a value of 35.58 m^3/s^2 at a wavelength of approximately 3.25 km. The wavelet contour plot displays slight elevations in PSD of up to 11.7 m^3/s^2 in Region 2 (37 km – 42 km) and Region 3 (45 km – 57 km) where the vertical velocity displays wave-like patterns.

The cospectral analysis between w' and θ' measurements for flight leg 1 shown in Fig. 4.16(c) does not offer a clear result in Region 1 (20 km – 30 km) where there was no easily determined consistent relationship between wind and temperature fluctuations. In Region 2 (37 km – 42 km) there is a peak in the cospectral power at wavelengths of 2 km – 3 km with a phase difference of approximately 90^o (see Fig. 4.16 (d)). In Region 3 (45 km – 57 km) the peak in cospectral power (Fig. 4.16(c)) occurs in the wavelength range

of 3 km – 4 km, with a phase difference (Fig. 4.16(d)) of approximately 0^{o}. These results are consistent with what is seen in the line plot of vertical wind and temperature fluctuations along the flight track (Fig. 4.16(a)).

To demonstrate the utility of using wavelet generated phase difference contour plots to determine phase relations between w' and θ', Figs. 4.17 and 4.18 show three examples of distinguishing between isolated waves (w', θ' phase shift = 90^{o}) and rolls (w', θ' phase shift = 180^{o}.) Figure 4.17 displays three previously discussed instances of isolated waves alongside the corresponding wavelet generated phase difference contour diagram. The orange dot (location highlighted by a large black arrow) indicates the w' zero crossing point at which phase difference is read off the graph. Similarly, for the more extended roll structures in Fig. 4.18, the dashed black box indicates the region corresponding to the rolls over which the phase is read off the graph.

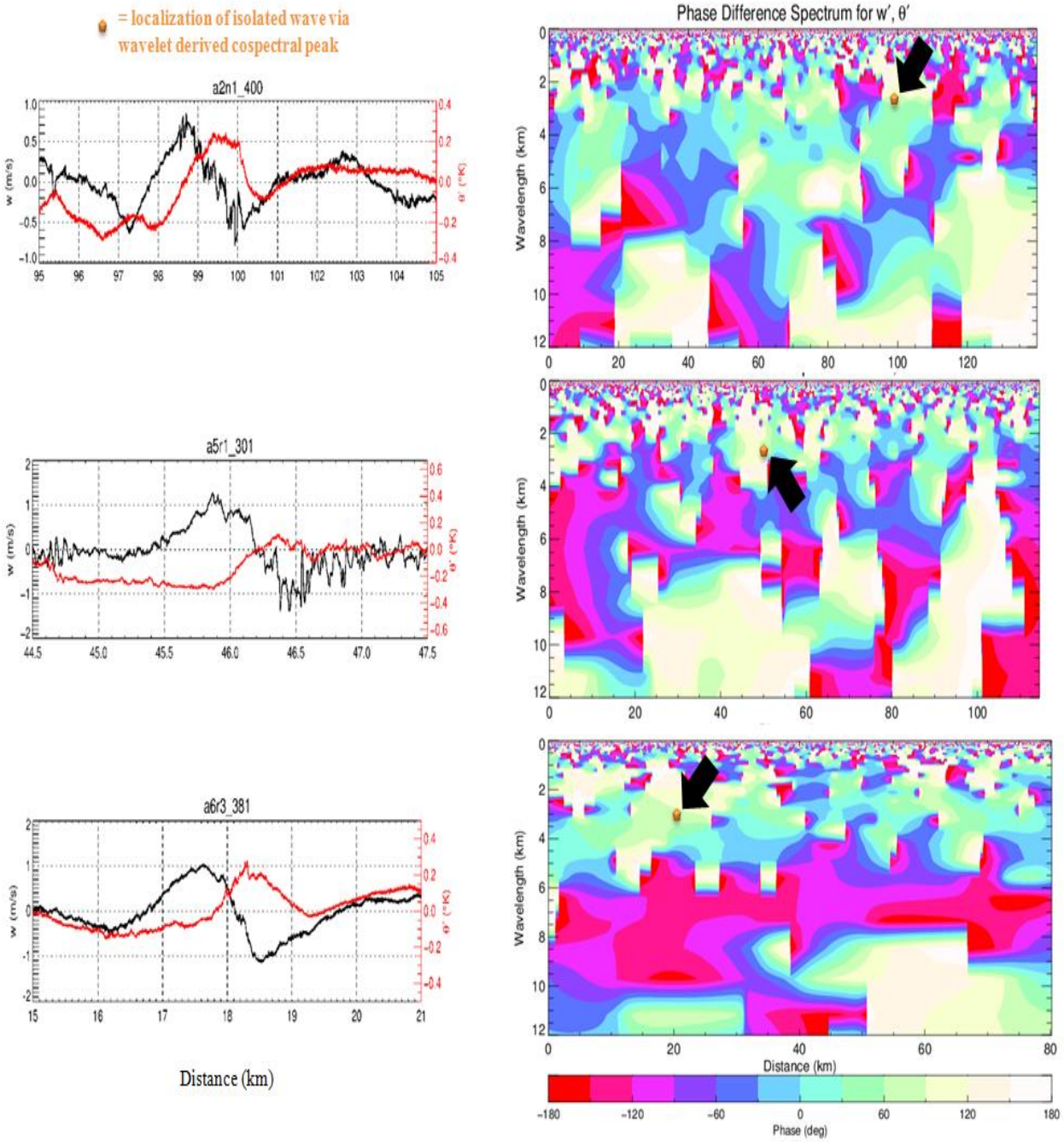

Figure 4.17: Demonstration of using wavelet based phase difference contour diagrams to ascertain phase shift between fluctuations in vertical velocity and potential temperature for three cases of isolated waves. Measurements along the flight track are shown on the left while the corresponding phase difference plot is shown on the right. The region at which the phase difference is read is indicated marked by an orange dot, indicated by a large black arrow.

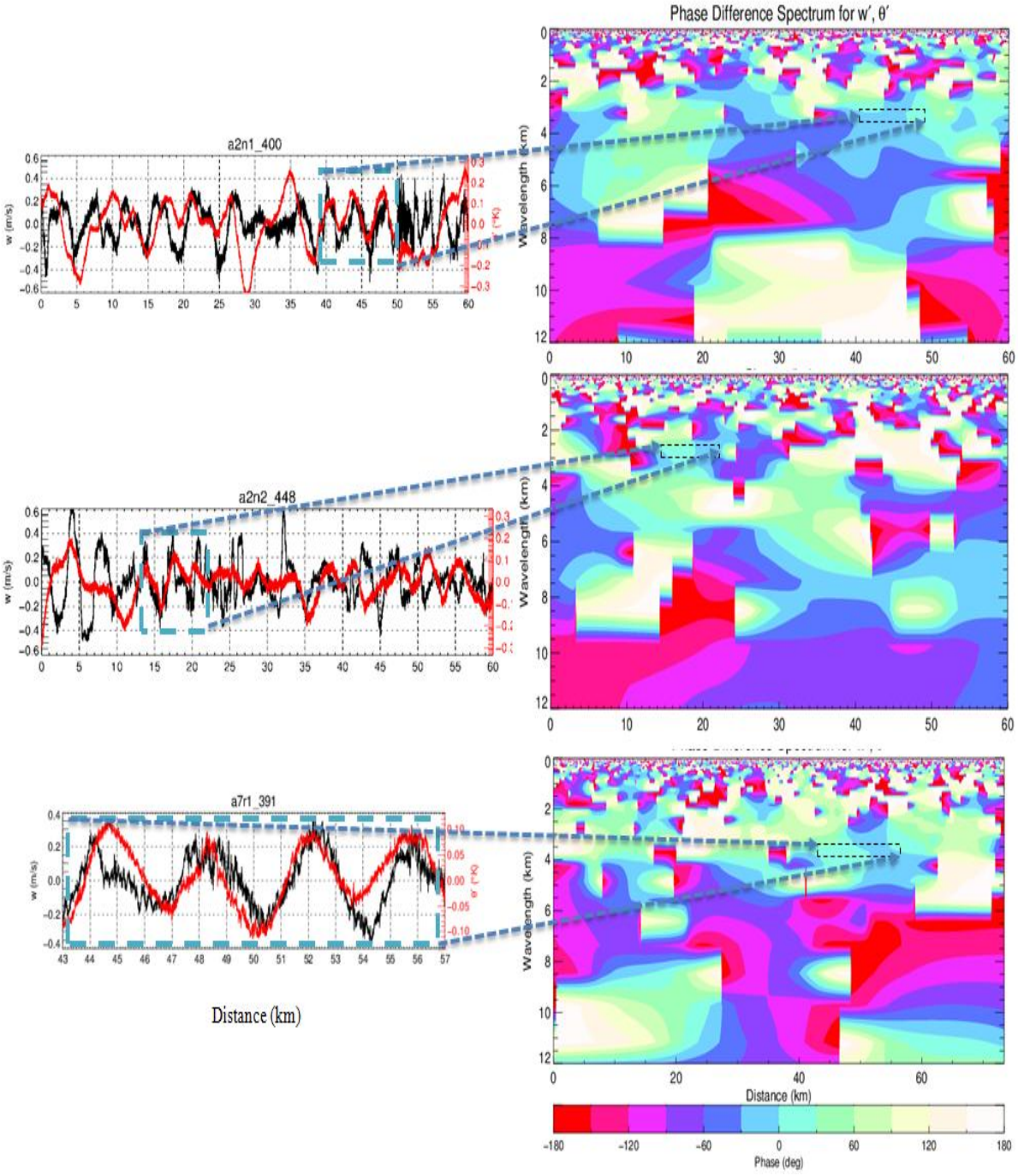

Figure 4.18: Demonstration of using wavelet based phase difference contour diagrams to ascertain phase shift between fluctuations in vertical velocity and potential temperature for three cases of rolls. Measurements along the flight track are shown on the left while the corresponding phase difference plot is shown on the right. The region for which the phase difference is read is indicated by a dashed black box.

In accordance with typical presentation shown for Fourier analysis, Fig. 4.19 shows a separate log-log plot of the wavelet determined PSD of horizontal and vertical wind fluctuations as a function of vertical wavenumber (and wavelength) for the entirety of flight leg 1. The PSD for the horizontal wind perturbations is the sum of the PSDs for the zonal (u') and meridional (v') wind perturbations. The dashed line represents the log-log 5/3 slope that is typically observed in turbulence (Kaimal and Finnegan, 1994). The spectrum from the measured time series of each component of the wind fluctuations approximately follows the -5/3 slope from wavelengths of 5 km to 50 meters.

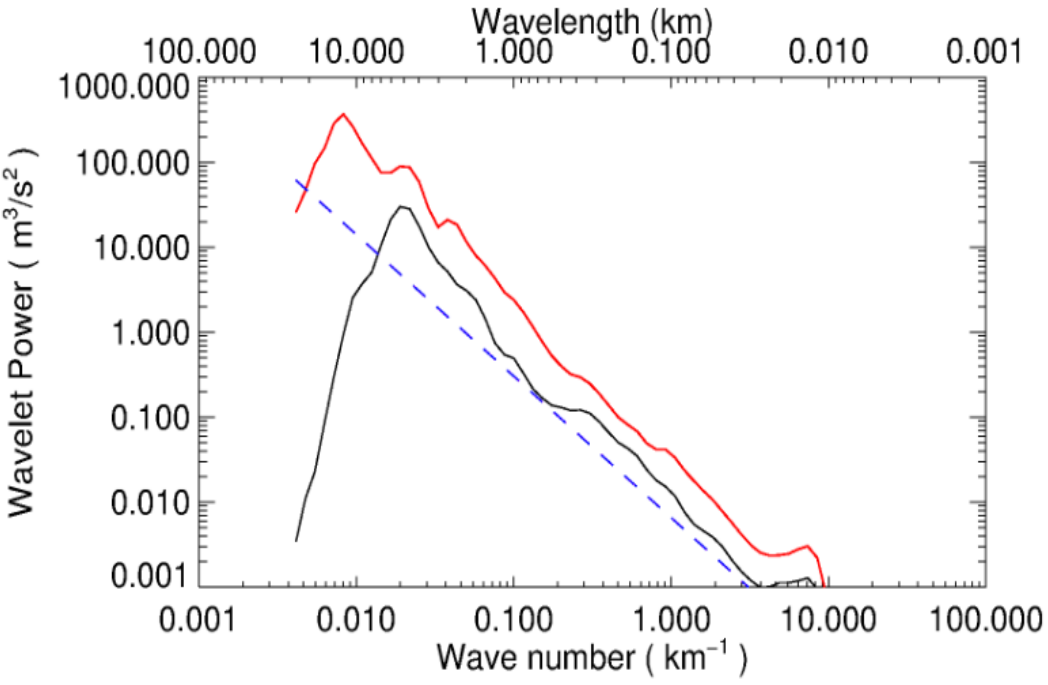

Figure 4.19: PSD for flight leg 1. Fluctuations in vertical wind velocity (w') is shown in black while fluctuations in horizontal wind velocity (u') is shown in red. Dashed blue line represents -5/3 slope.

4.7 Flight Leg 2: Turbulence and Coherent Structures

Flight leg 2 on November 23 was oriented transverse to the anvil outflow, back along the track of flight leg 1, from west to east, but at a higher altitude of 13.56km. Figure 4.19 displays the combination of the lidar backscatter signal and in situ vertical wind measurements for this leg.

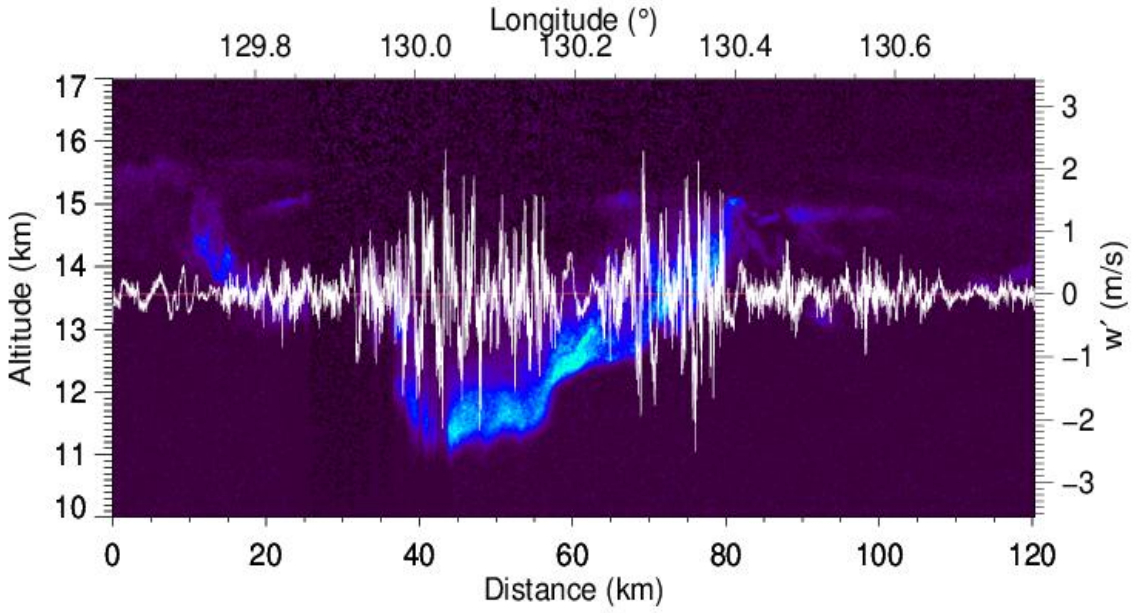

Figure 4.20: Lidar backscatter signal contour outlining the anvil cloud's base with superimposed (white) fluctuations in vertical velocity (white) along the Egrett flight track (red.)

Evident in Figure 4.20 are two patches of intense turbulence with maximum vertical wind gusts of approximately 2.4 m/s encountered inside the outflow cloud. The most substantial vertical velocity fluctuations appear periodic, suggesting the presence of a coherent structure amidst the turbulent background. Figure 4.21 provides a greater

resolution view of the wind and temperature fluctuations along the flight track. In this case, it is more challenging to discern a phase relationship between the vertical wind and temperature fluctuations. The vertical wind and potential temperature fluctuation signals are seen to be lagging (55 km – 65 km) in phase (47 km – 52 km) and leading one another (35 km – 45 km) at different points throughout the flight leg. Thus, wavelet spectral methods were applied to quantify phase relationships.

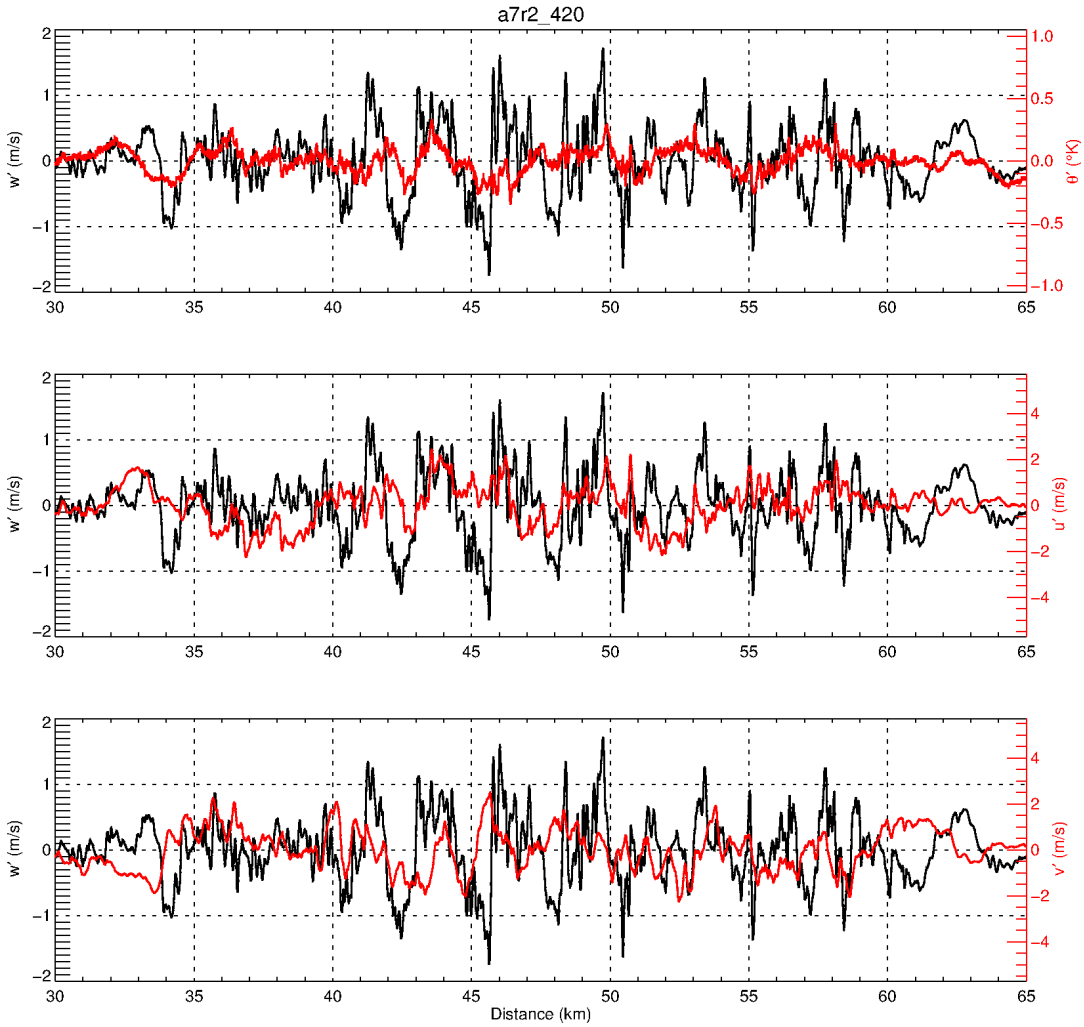

Figure 4.21: Fluctuations of vertical velocity (black) are over plotted against, from top to bottom, fluctuations in potential temperature, zonal, and meridional wind velocities for transverse flight leg a7r2_420 on 23 Nov., 2002.

4.8 Spectral Analysis of Turbulence and Coherent Structures in Flight Leg 2

Figure 4.22 presents results of continuous wavelet spectral analysis for the entire flight leg 2 as a function of wavelength. Section 4.6 outlines what each panel represents in these wavelet analysis figures. Fig. 4.22(b) reveals maximal power in vertical wind

occurring at wavelengths of 2 km – 3 km. Fig. 4.22(c) shows that maximum co-spectral power is concentrated at an approximate wavelength of 5 km. Fig. 4.22(d) reveals that the corresponding phase for the co-spectral maximum power falls near to 0^{o} phase difference band. Thus, if these fluctuations are coherent structures, it is not likely that the mechanism was a gravity wave. The phase relationship is more suggestive of either convective rolls or random turbulence.

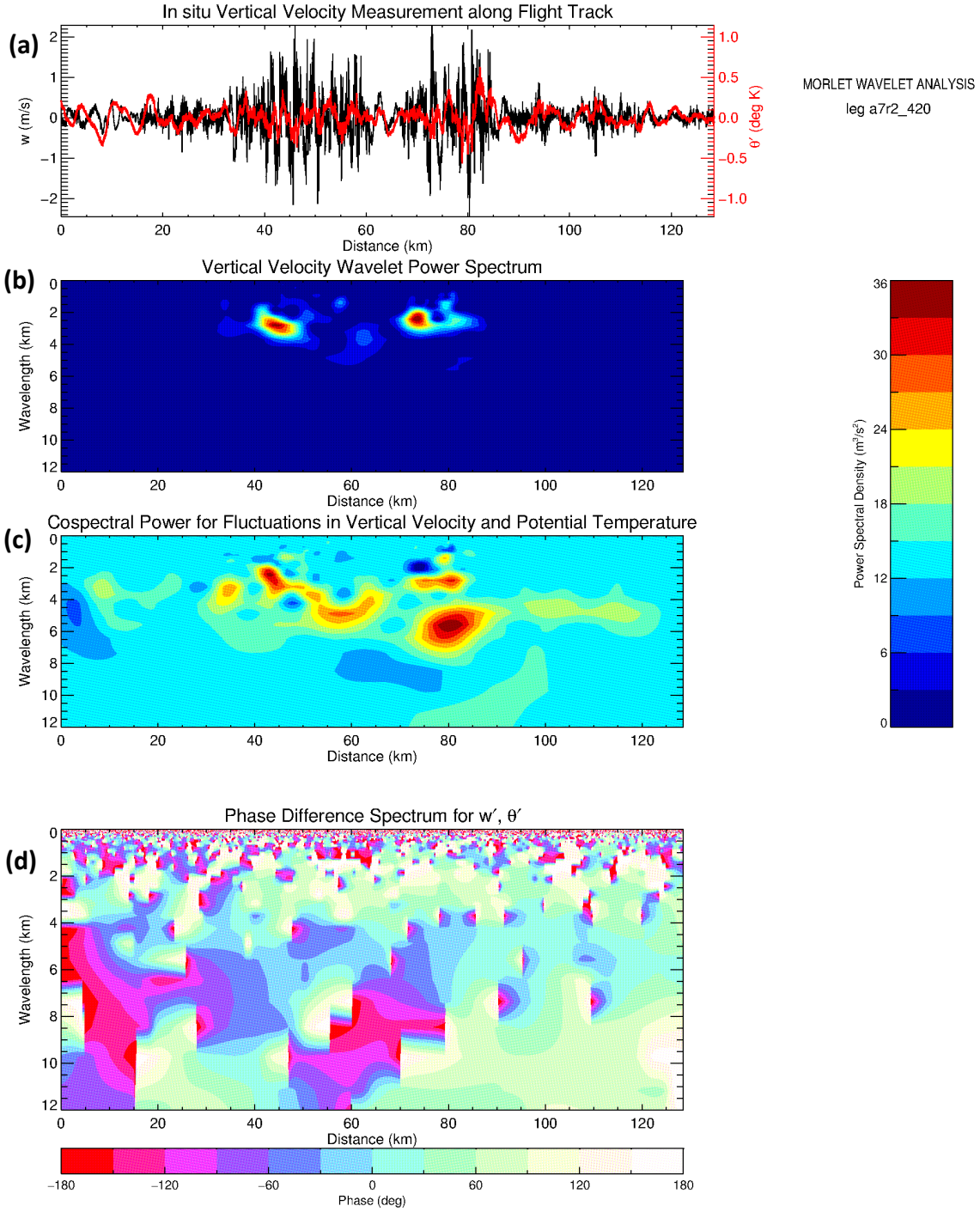

Figure 4.22: **(a)** fluctuations in vertical velocity along flight leg 2 (a7r2_420) between 30km-65km. **(b)** wavelet contoured power spectrum. **(c)** w'θ' wavelet contoured co-spectrum for region of flight track. **(d)** wavelet based phase difference spectrum for w'θ'.

The PSD of horizontal and vertical wind perturbations from flight leg 2 on November 23 are shown in Fig 4.23. These exhibit the characteristic log-log -5/3 slope that is well known for turbulence. The ratio of the power spectral densities of the vertical and horizontal wind perturbations is also shown in Fig. 4.23. Spectral ratio, or "SR," is henceforth defined as the value of the ratio of the vertical wind spectrum divided by the total horizontal wind spectrum and is calculated as PSD[w'] / (PSD[u']+PSD[v']). For the November 23 flight leg 2 case the SR varies from 0.6 to 0.8 in the inertial sub-range of turbulence: scales smaller than 500 m. If the spectral power was distributed equally between the three components of wind, then the SR would have a value of 0.5. There is thus a disproportionate amount of energy in the vertical fluctuations. The ratio is less than 0.4 for the larger scales that are associated with gravity waves and coherent structures.

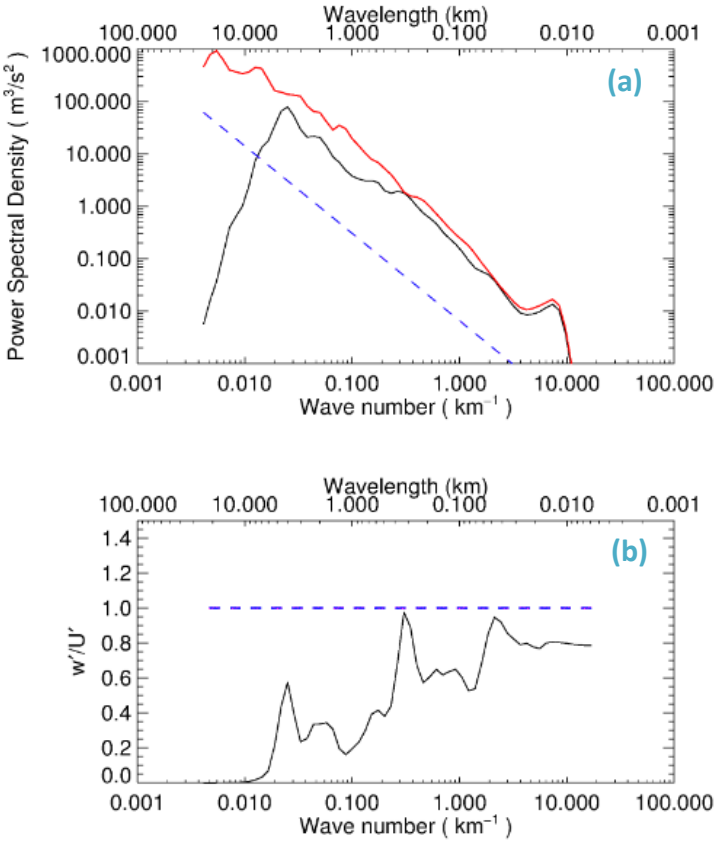

Figure 4.23: **(a)** PSD for vertical (black) and horizontal (red) wind velocity fluctuations. -5/3 slope is denoted by blue dashed line . **(b)** Spectral ratio, SR, of vertical to horizontal PSDs, i.e. PSD[w']/(PSD[u']+PSD[v']). SR = 1 denoted by blue dashed line.

The PSD of the turbulent fluctuations inside the anvil outflow is unique in comparison with similar measurements of substantial turbulence in different meteorological settings. One specific example is clear air turbulence (CAT) encountered in the Aberystwyth Egrett Experiment in May – June 2000. Figure 4.24 presents both PSD and SR ratios from the June 6, 2000 CAT case (Fig. 4.24(a)) and EMERALD 2's flight leg 2 (Fig.4.24(b).) CAT over Wales was generated by shear instability (Pavelin et al., 2001; Whiteway et al. 2004). Both spectra in Fig. 4.13 exhibit the log-log -5/3 slope

as expected, but the ratio of the vertical to horizontal wind spectra is larger for the EMERALD-2 case than the CAT case. For CAT, the SR is less than 0.3 at scales smaller than 500 m. This is much smaller in comparison with the SR in the anvil outflow which has a minimum value of approximately 0.5 at these scales.

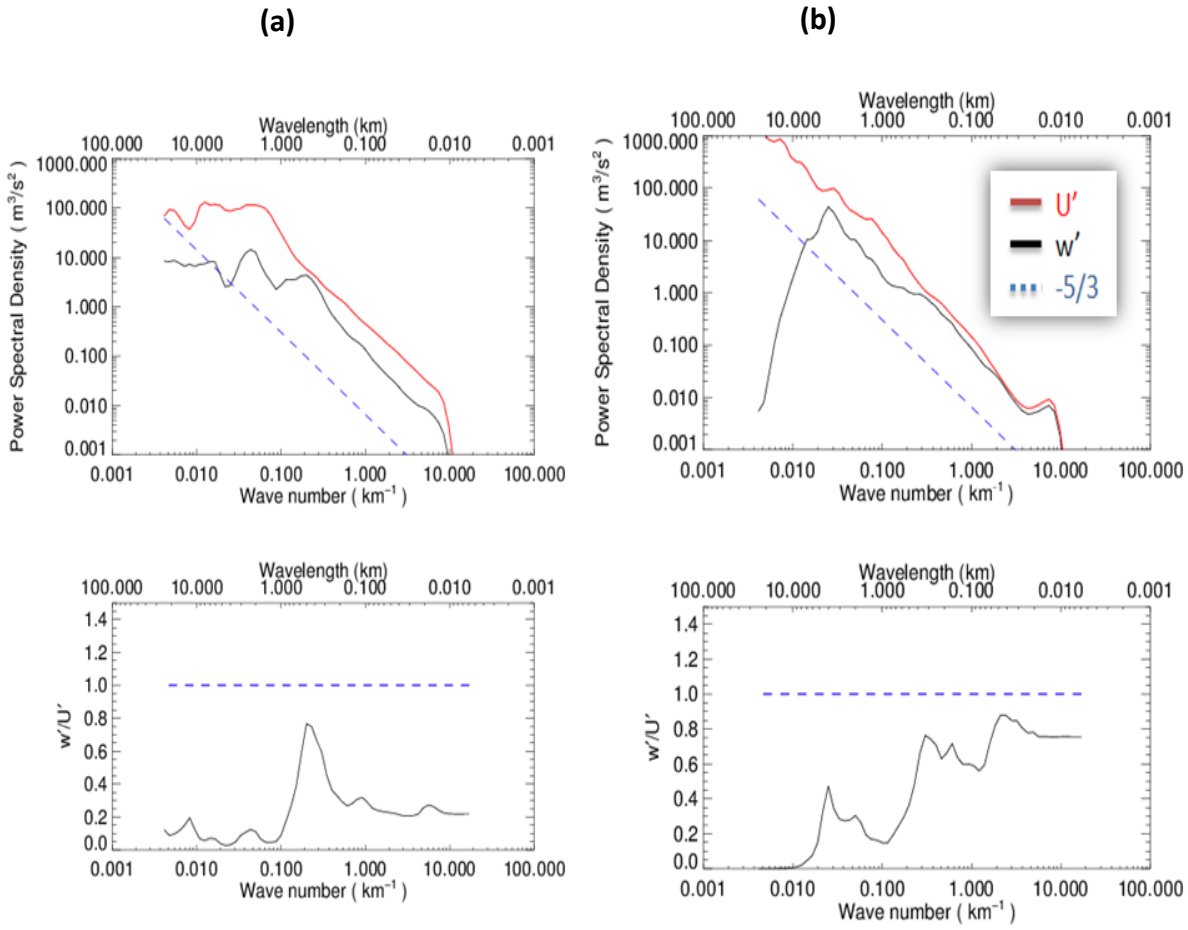

Figure 4.24: **(a)** [top] PSD for vertical (black) and horizontal (red) wind velocity fluctuations for June 6, 2000. [bottom] ratio of vertical to horizontal PSDs for June 6, 2000, **(b)** [top] PSD for vertical (black) and horizontal (red) wind velocity fluctuations for flight leg 2, November 23, 2002. [bottom] SR for flight leg 2, November 23, 2002.

Another available comparison of spectral characteristics of turbulence within the cirrus anvil outflow is with measurements in mid-latitude cirrus clouds during the EMERALD-

1 campaign carried out with the Egrett aircraft above Adelaide, Australia on September 19, 2001. Figure 4.25 shows the PSDs and SRs of the wind fluctuations in intense turbulence at the top and the base of the cloud. At the cloud top, the turbulence was generated by shear. The SR was less than 0.4 at scales smaller than 500m (Fig 4.25(a)). At the base of the cloud, however, the SR at these scales was slightly larger, but still less than the minimum value of 0.5 encountered in EMERALD-2.

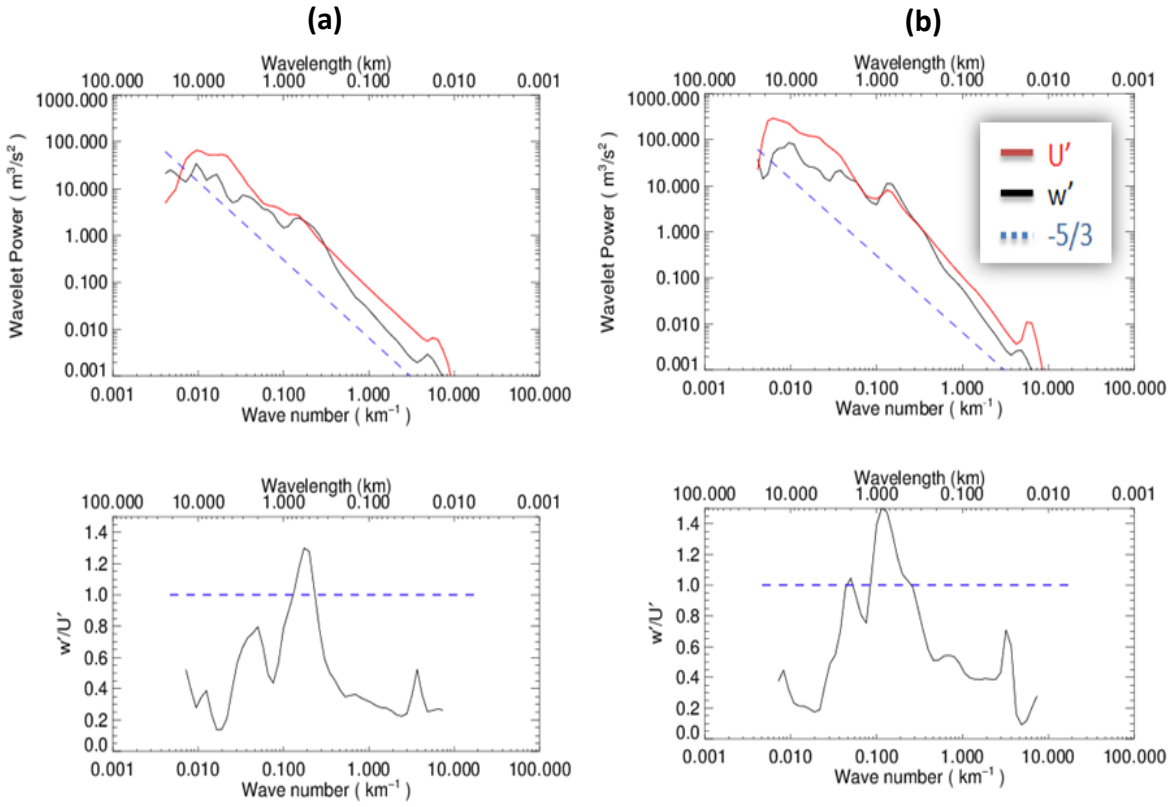

Figure 4.25: (a) [top] PSD for vertical (black) and horizontal (red) wind velocity fluctuations for top of cloud on September 19, 2001. Blue dashed line represents -5/3 slope. [bottom] ratio of vertical to horizontal PSDs for top of cloud, **(b)** [top] PSD for vertical (black) and horizontal (red) wind velocity fluctuations for bottom of cloud, September 19, 2001. [bottom] SR for bottom of cloud where there is greater convection and fall streaks / virga. Blue dashed line represents SR = 1.

Consequently, the relative proportion of spectral power in the vertical wind fluctuations was greater in the anvil outflow in comparison with similar measurements in shear generated CAT (Aberystwyth Egrett Experiment) and with shear generated turbulence within cirrus clouds (EMERALD-1.) This can be explained in terms of the mechanism of instability that generated the turbulence. In the case of the anvil outflow near the core of the convection, the background temperature gradient would have been very near the wet adiabatic lapse rate and the turbulence would have been driven by convective instability. There would not be as much shear within the anvil outflow required to generate turbulence. When there is less shear, the vertical displacements in the turbulence would not transport air with as much of a change in the horizontal velocity. In the case of shear generated turbulence (Wales, June 6, 2000 or Adelaide, Sept 19, 2001), the vertical displacements of air would carry large differences in the horizontal velocity and the PSD of horizontal wind perturbations would be greater in comparison to the PSD of the vertical wind perturbations. Figure 4.26 shows a comparison for the PSDs of the vertical wind on the same graph for each case, for the PSDs of the horizontal wind fluctuations and for the w'/U' ratios. It is seen that the relative enhancement of the horizontal wind fluctuations on June 6, 2000 (CAT) is the reason for the smaller w'/U' spectral ratio.

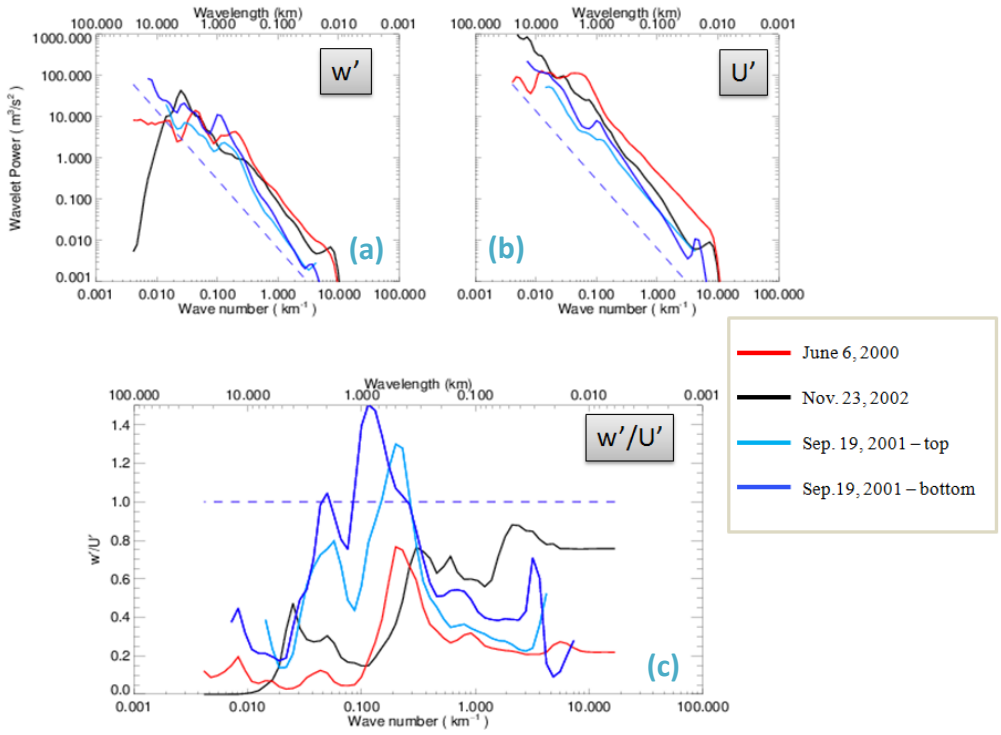

Figure 4.26: Spectral comparisons of scenarios with differently generated turbulence. **(a)** PSD for fluctuations in vertical velocity **(b)** PSD for fluctuations in horizontal velocity (U'=u'+v'). **(c)** Ratio of PSDs of vertical to horizontal wind fluctuations.

In Fig. 4.26, an interesting feature common to all spectra and spectral ratios is a peak which occurs in the range of scales between approximately 300 m and 1000 m. This region of the spectra can be considered to encompass the scales of the instability that generated the turbulence. The energy is input at this scale and cascades to smaller scales. The ratio of vertical to horizontal wind perturbation is greatest at the energy input scale. As the turbulent energy dissipates to smaller scales, there is a tendency for the horizontal fluctuations to become relatively more prominent.

4.9 Flight Legs 3 & 4: Dynamical Measurements along the Axis of the Anvil Outflow

The rationale behind conducting longitudinal flight legs was discussed in Section. 3.4.1. with lidar contour plots of both longitudinal flight legs being shown in Fig. 3.10. As shown Fig 3.11 of Section. 3.4.1, flight leg 3 (Nov. 23) was directed southward moving along the axis of the anvil outflow away from the convection. The height of the aircraft followed a sawtooth pattern between altitudes of approximately12 km and 14 km. The lidar and vertical wind measurements are shown in Fig. 4.27. The outflow cloud was not as optically thick during the longitudinal flight legs, so that the lidar signal was not entirely extinguished and could provide a measure cloud structure through the entire vertical extent.

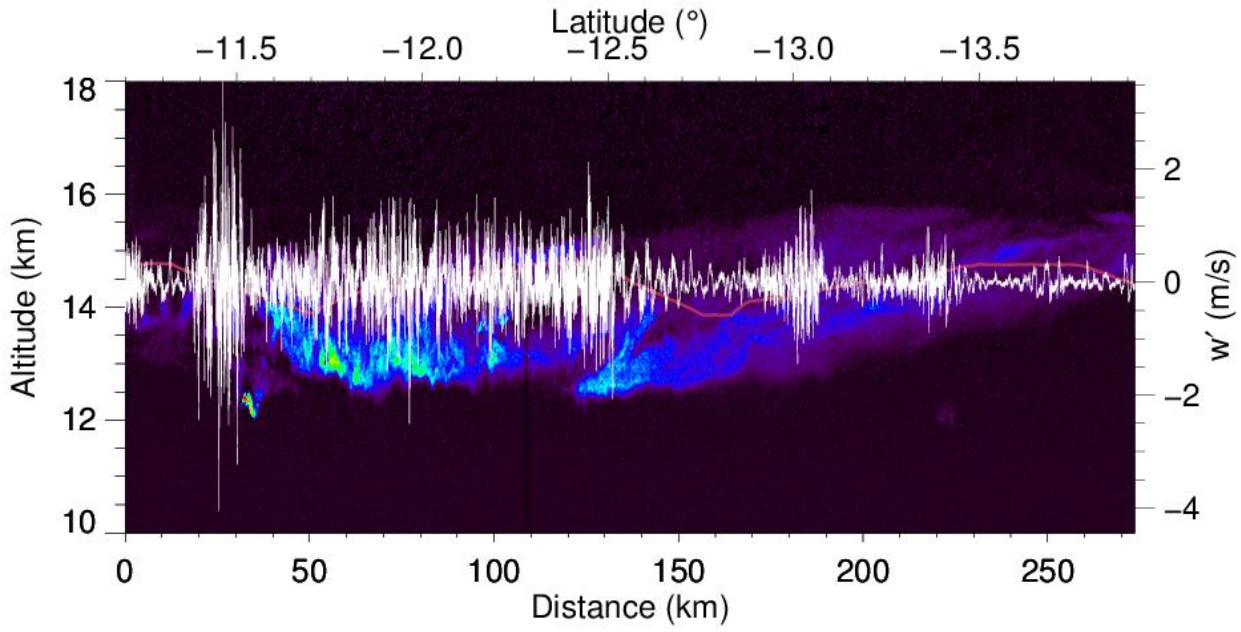

Figure 4.27: Flight leg 3. Egrett flight track shown in red with overlaid vertical velocity fluctuation measurements shown in white.

The subsequent flight leg, flight leg 4 (Fig. 4.28) returned along the same track as flight leg 3, initially following the same sawtooth pattern, but then descending from a height of approximately 14 km to 11.5 km. Altitude variations were conducted in a manner that pilots often refer to as "porpoising" which is a systematic, stepwise up and down height variation. A height distribution of microphysical properties of the cloud particles encountered along this leg was reported in Whiteway et al. (2004a).

The porpoising flight pattern provided a vertical profile of wind velocity and temperature measurements. The measurements were averaged vertically over a sequence of 100 m segments (boxcar average) in order to yield basic vertical profiles. As explained in Section 3.5, as in the case of horizontal averaging lengths, the vertical averaging length was selected experimentally as an acceptable trade-off between variability and over-smoothing of the data. The vertical profiles were then used to investigate the generation mechanisms for the turbulence detected within the cirrus anvil outflow cloud by calculating the Richardson number (Ri) as defined by Equation 2.45 (see Sect. 2.6). Vertical profiles of potential temperature, horizontal wind, vertical wind fluctuations, w' (used as a proxy for TKE) and Ri extracted from flight leg 4 (Fig. 4.28) are shown in Fig. 4.29.

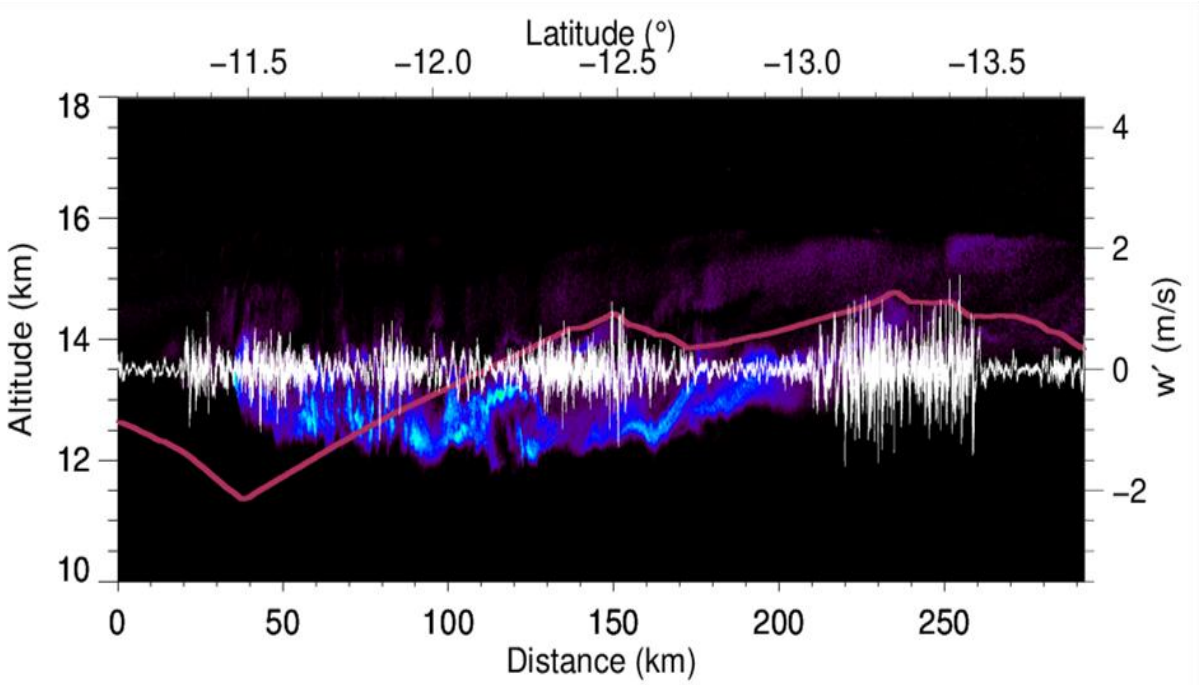

Figure 4.28: Flight leg 4. Egrett flight track shown in red with overlaid vertical velocity fluctuation measurements shown in white.

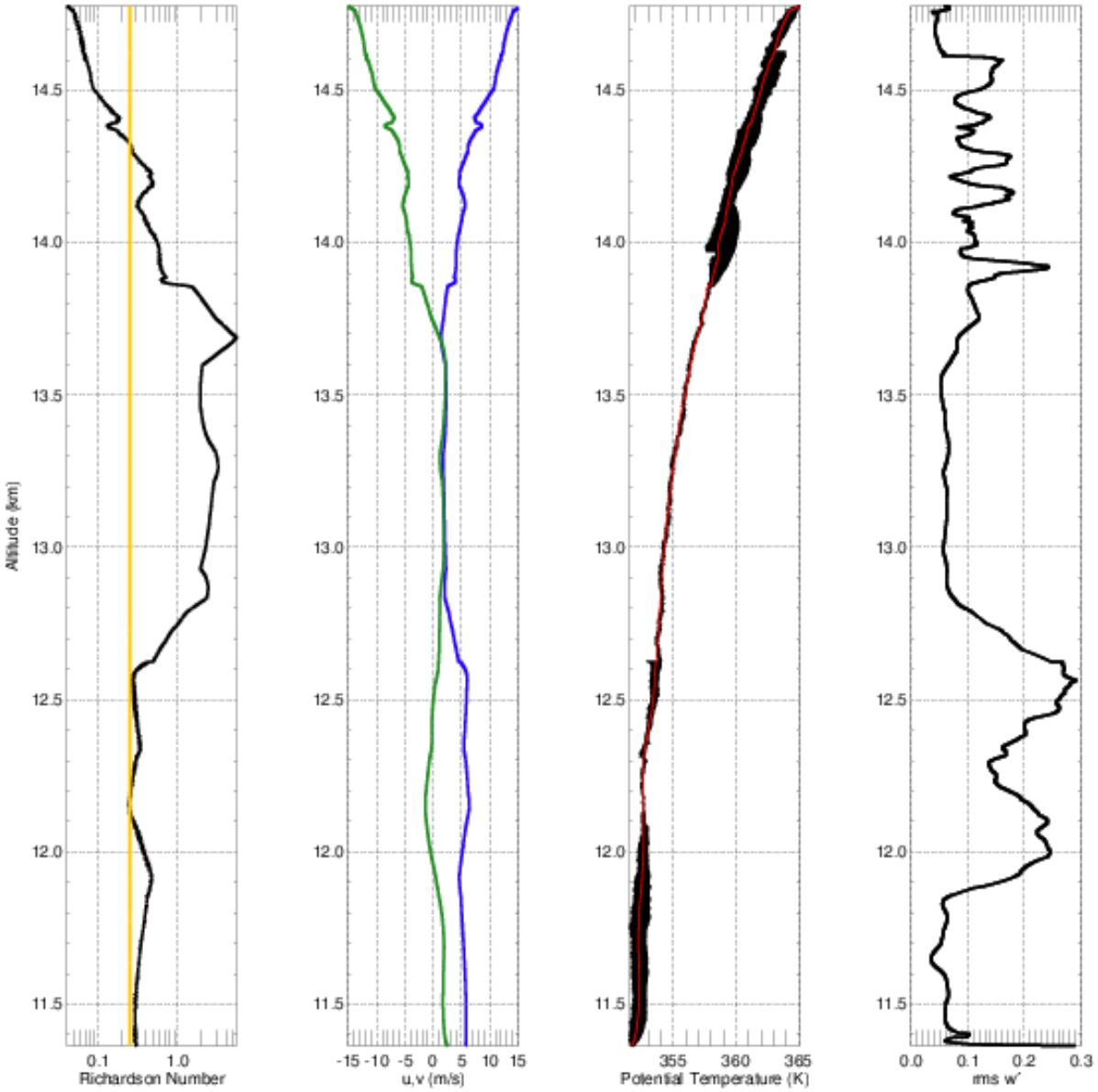

Figure 4.29: Vertical profiles of Richardson number (yellow line is critical Richardson number = 0.25), horizontal wind velocity (u = blue, v = green), potential temperature (red = vertical averaging of flight leg data over 100 m) and Root Mean Square (RMS) perturbation vertical velocity (w') used as a proxy for TKE from flight leg 4 on November 23rd.

Figure 4.29 provides an explanation for the turbulence generation. The relatively large values of RMS w' occurred only where the Ri was less than a value of unity and typically the critical value of 0.25. Also the enhanced RMS w' only occurred within the cloud that had a base height of approximately 12 km. Near to the cloud base in the remnant of the core of the convection (heights of 12 to 12.6 km corresponding to latitudes $11.7^{o} – 11.8^{o}$ S), the background potential temperature gradient was near zero (neutral) and very little shear was required to generate the turbulence. This was convectively generated turbulence. At heights above 14 km (near the far reaches of the outflow cloud beyond the latitude of 12.4^{o} S , the gradient in potential temperature is observed to be positive but there is strong shear present to reduce the Ri to below unity. At heights above 14 km the turbulence is generated by wind shear. A stable region with Ri greater than unity exists at heights 12.8 km to 13.6 km and consequently the RMS w' is minimal in this region.

Thus the locations of turbulent patches in the outflow can be explained with regard to the vertical gradients in temperature and wind in terms of the standard Richardson number (Ri). In the region near the remnant of the core of the convection the cause of the turbulence was buoyant instability. This was due to the mixing within the cloud. At the top of the cloud, farther away from the convective core, the turbulence was caused by wind shear. This wind shear was a result of the convection having blocked the background flow such that the air was moving faster as it moves over the top of the convection. This result has important general implications for flight safety since it provides a guide to where intense turbulence can occur around and within the outflow anvil. It was previously found that turbulence having flight safety implications was

encountered by commercial air traffic at 100s of km from convective activity (Lane et al, 2008). The results of this study identify important factors for prediction of the location of intense turbulence that should be avoided by commercial air traffic. For at least two hours after deep convection has ceased to be active, intense turbulence will be encountered in the following areas: (a) the remnants of the core of the convection, and (b) the top of the outflow anvil cirrus cloud. An important point is that turbulence is actively generated within the remnants of the convective system, rather than passively decaying as the air flows away from the prior convection. Such detailed in situ measurements of turbulence in convective anvil outflow were not available prior to this study.

Figures 4.30 and 4.31 present a projection of the vertically calculated Richardson number along the horizontal flight tracks of flight legs 3 and 4, respectively. Also displayed are potential temperature, aircraft altitude, vertical and horizontal wind velocities and TKE along both flight tracks. Figs. 4.30 and 4.31 indicate that turbulence persists in patches along the outflow as seen in the small-scale variations in vertical wind and the TKE. Between latitudes of -13.0^{o} and -13.5^{o}, the Egrett covered the same path in flight legs 3 and 4 in terms of both horizontal position and height. In the 30 minutes between flight legs 3 and 4, through approximately the same section of the cloud, the turbulence actually increases in intensity in most of this area Again this demonstrates that there was active generation of turbulence within the anvil outflow. The turbulence was therefore not a remnant of the original convection, passively decaying with outward movement along the outflow axis.

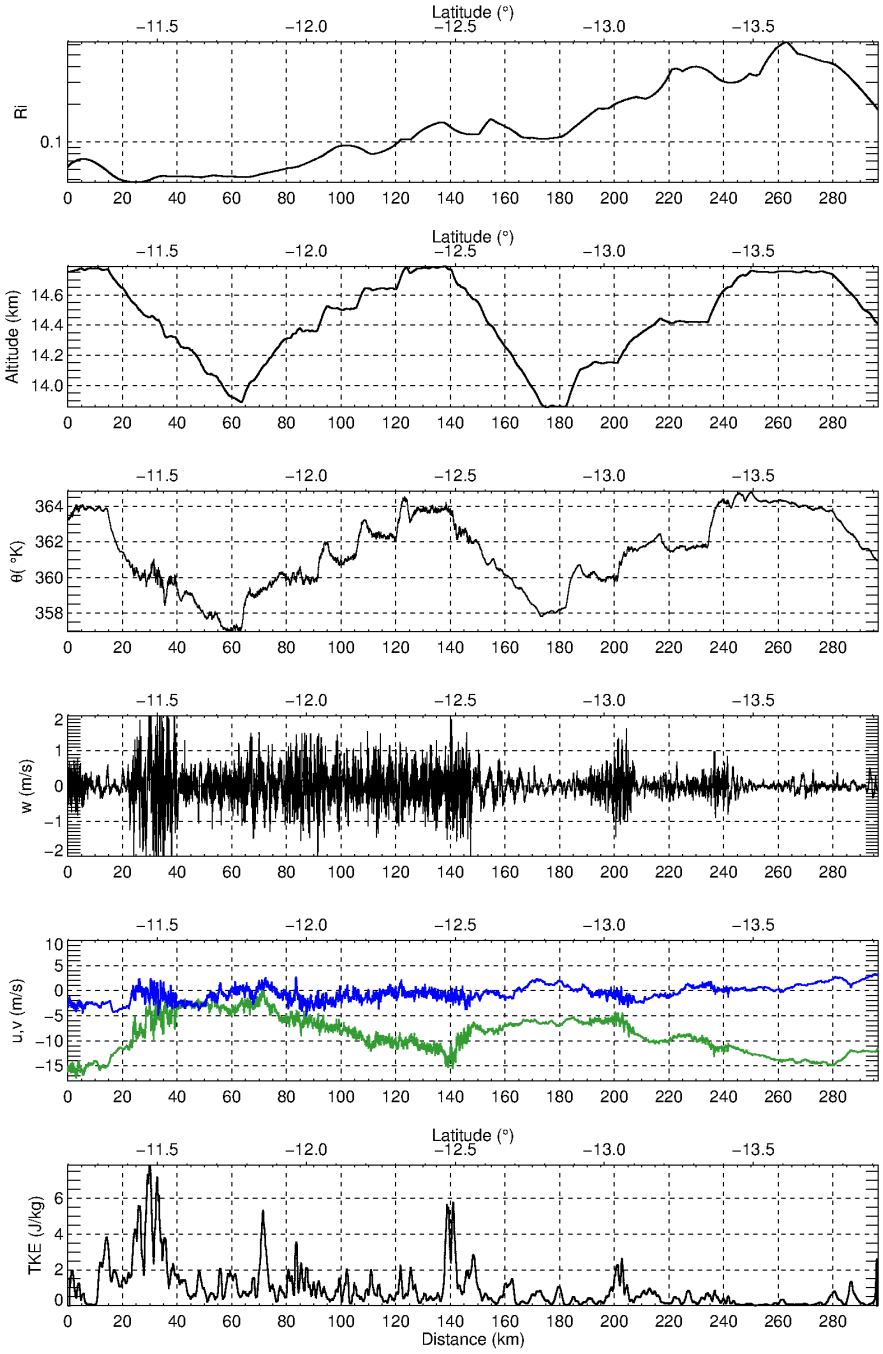

Figure 4.30: horizontal measurements of Richardson number, wind velocity and turbulence kinetic energy along flight leg 3. Zonal wind, u, measurements are in blue while meridional wind, v, measurements are in green.

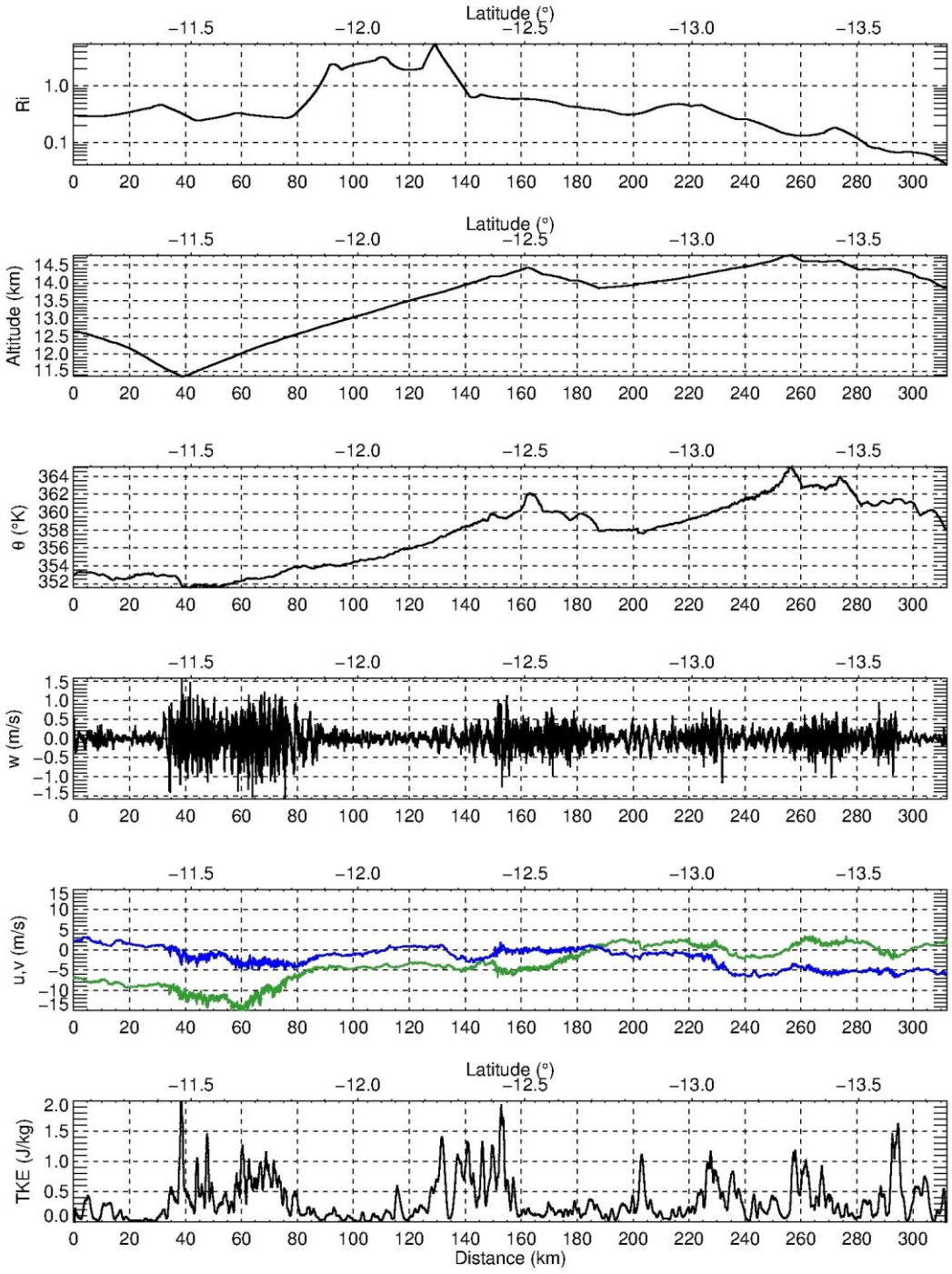

Figure 4.31: horizontal measurements of Richardson number, wind velocity and turbulence kinetic energy along flight leg 4. Zonal wind, u, measurements are in blue while meridional wind, v, measurements are in reen.

4.10 Evolution of the Spectrum of Turbulence along the Outflow

A key observation was made with respect to the evolution of the spectrum of turbulence according to the position at which the turbulence occurred within the outflow. With increasing distance from the convective core, the spectral properties of the turbulence changed. Specifically, turbulence close to the convective core region was seen to be more isotropic, meaning that air motions are divided approximately equally in power between the vertical and horizontal directions. Further from the core region, approaching the end of the outflow where greater shear exists, the turbulence had less of a vertical component and motions are more concentrated in the horizontal.

The changing properties of turbulence are illustrated by taking the spectrum in the two regions discussed above: (a) near the core and (b) at the end of the outflow. Figures 4.32 and 4.33 show the spectrum as calculated for flight legs 3 and 4 for both regions. Notable in Figs 4.32 and 4.33 is again the peak in the 300 m – 500 m region denoting the transition from laminar flow to turbulence. In the inertial subrange where turbulence occurs (below wavelengths of 500 m), the spectra in Figs. 4.32 and 4.33 are seen to be consistent in values of the spectral velocity aspect, or Spectral Ratio (SR, where SR = PSD(w')/PSD(U')) . Both flight legs show SRs near the core of approximately 0.8. The values of SR in the shear region at the end of the anvil outflow decreased to approximately 0.6 for flight leg 3 and 0.4 for flight leg 4. This indicates that the wind fluctuations in the turbulence become more horizontal and "flattened" in a pancake manner as one moves away from the core. This pancake effect was postulated by Lilly (1983) who referred to it as "stratified turbulence". It was predicted that the

turbulent fluctuation would become more horizontal moving away from the convective core along the anvil outflow.

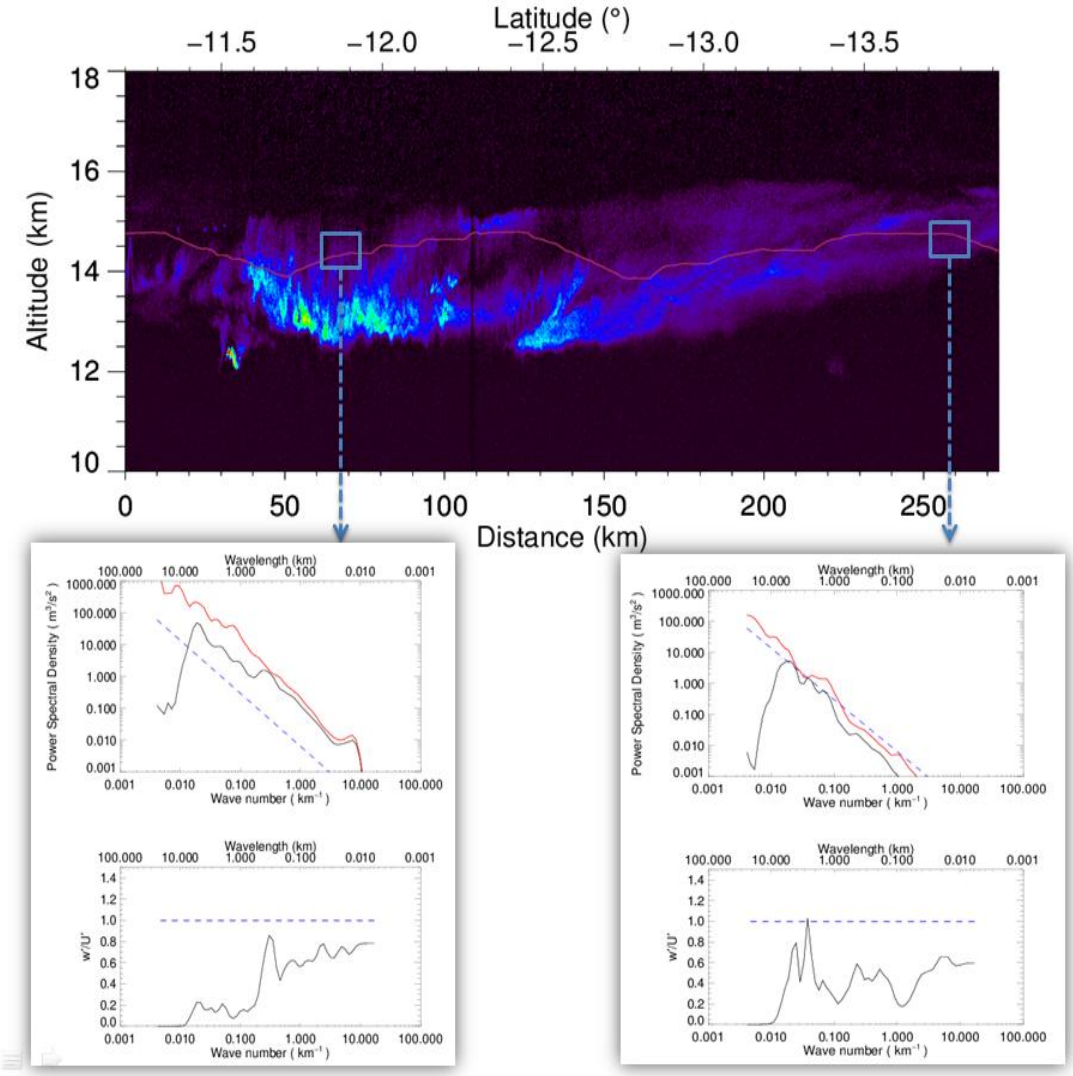

Figure 4.32: Lidar backscatter contour profile showing the outline of the cloud base as measured flight leg 3, Nov. 23, 2002. The convective core of the storm is located near -11.5 degrees and the end of the outflow occurs just beyond -13.5 degrees. The two regions where horizontal and vertical wind fluctuation PSDs are sampled are approximately located between 60 km – 75 km and 275 km -290 km, respectively. The Egrett flight track is shown in red.

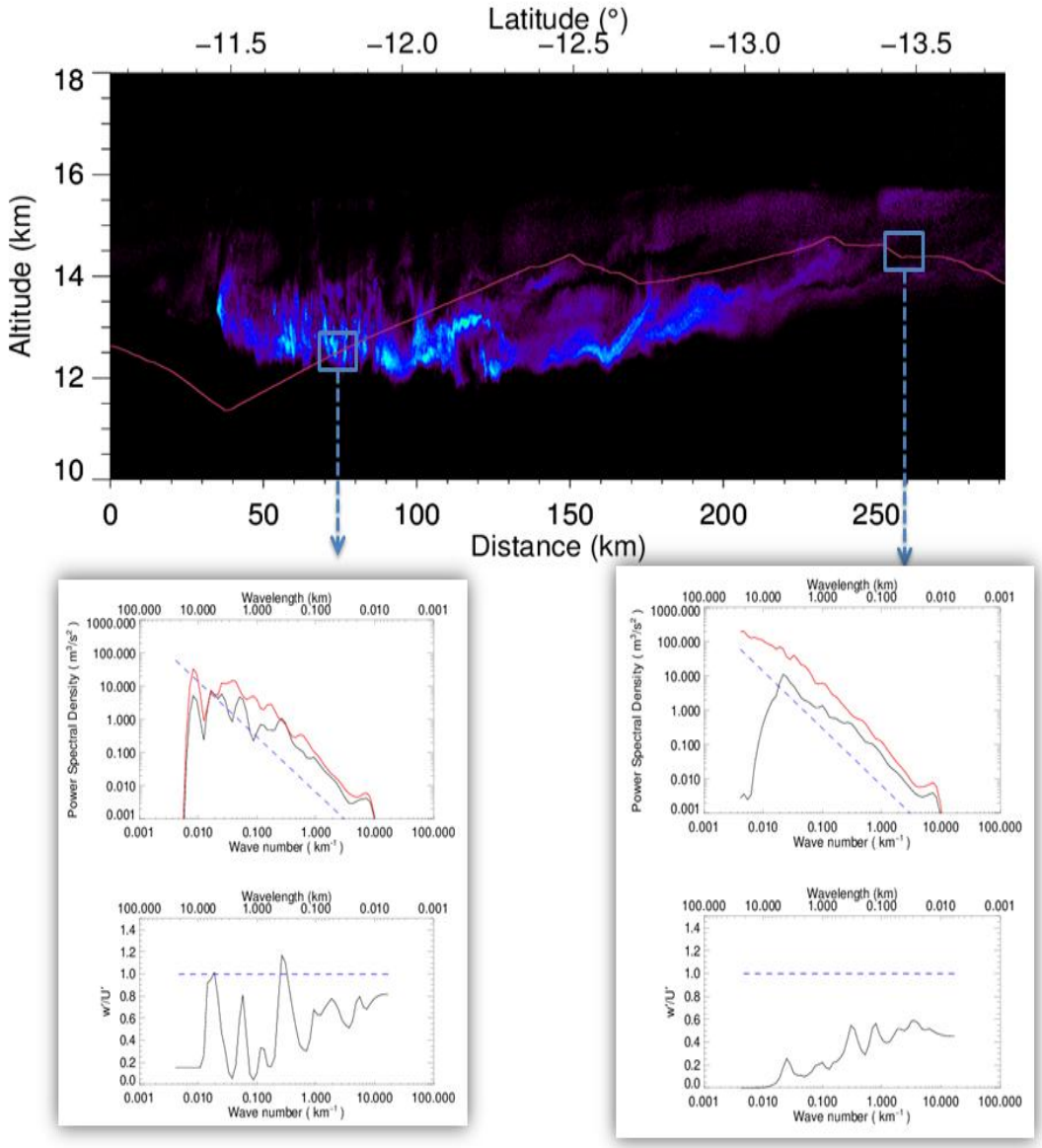

Figure 4.33: Lidar backscatter contour profile showing the outline of the cloud base as measured flight leg 4, Nov. 23, 2002. The convective core of the storm is located near -11.5 degrees and the end of the outflow occurs just beyond -13.5 degrees. The two regions where horizontal and vertical wind fluctuation PSDs are sampled are approximately located between 60 km – 75 km and 275 km -290 km, respectively. The Egrett flight track is shown in red.

The SR for both flight legs at the end of the outflow (0.5) is about the same as shear generated turbulence in jet stream cirrus as shown in Figs 4.24 and 4.25 in this chapter. This is again evidence that the spectra in a neutral saturated environment near the core is unique from spectra in an environment with stable stratification but strong wind shear.

To confirm this observation, the PSD in horizontal and vertical wind velocity perturbations was examined at regular intervals (ranging from 5km to 100km) with increasing distance from the convective core. Figure 4.34 displays the lidar plot of the anvil cloud with overlaid curves indicating the value of the spectral velocity aspect ratio as calculated at horizontal averaging intervals of 1km, 10km, 20km, 30km and 50km.

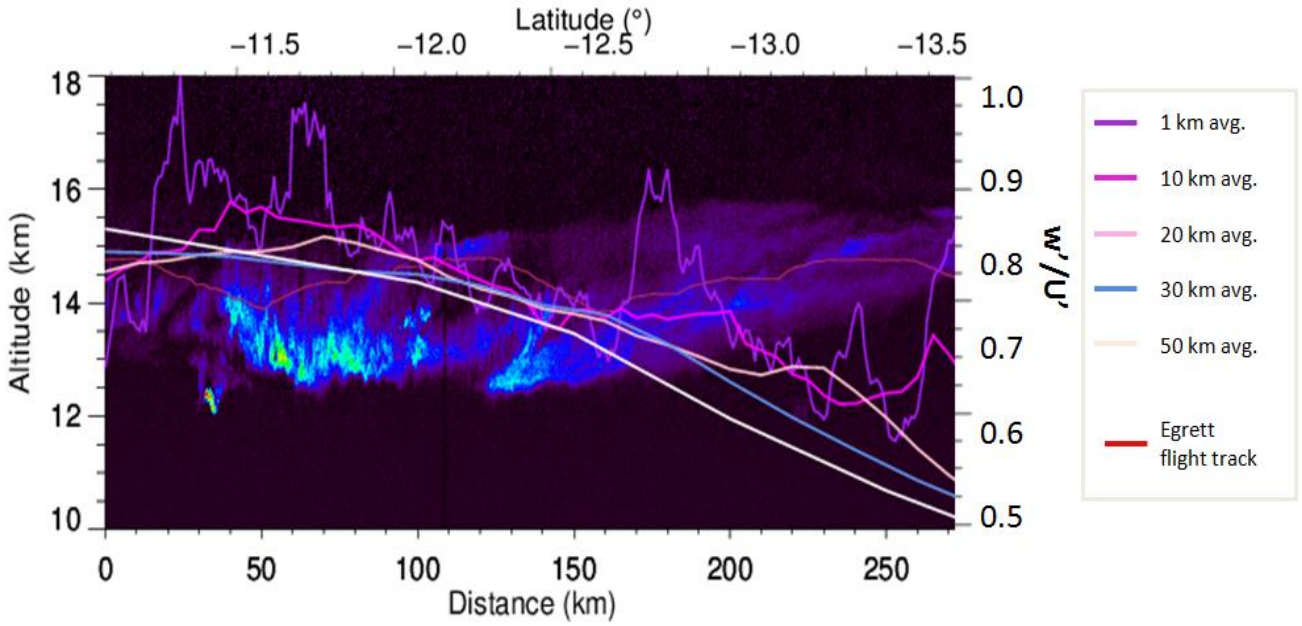

Figure 4.34: Lidar backscatter contour plot outlining anvil base taken in flight leg 3 (Nov. 23, 2002) with overlaid curves for different horizontal averaging periods displaying decreasing SR with increasing distance from the core.

It is evident from Fig. 4.34 that the ratio w'/U' ratio decreases nearly linearly with increasing distance from the core region.

4.11 Dynamics at the base of the anvil outflow

The flight pattern on 2 Dec., 2002 was designed to probe the base of the anvil outflow cloud on that day. There were 11 flight legs oriented parallel to the outflow axis (longitudinal) and stacked vertically through the regions below, at, and above the cloud base. The King Air was approximately 5 km below the Egrett for each flight leg, with the lidar measuring the cloud structure at the cloud base. The lidar measurements along the first flight leg are shown in Fig 4.35 along with the flight tracks that probed the cloud base. A summary of each flight leg is provided in Table 4.4. Figures 4.36 and 4.37 show the contour of the cloud base for six selected flight legs (those of the original 11 flight legs which were not significant ascents or descents in altitude.) As in the other contour plots presented throughout this chapter, these figures also include the Egrett flight path (red) and the measured vertical velocities (white.)

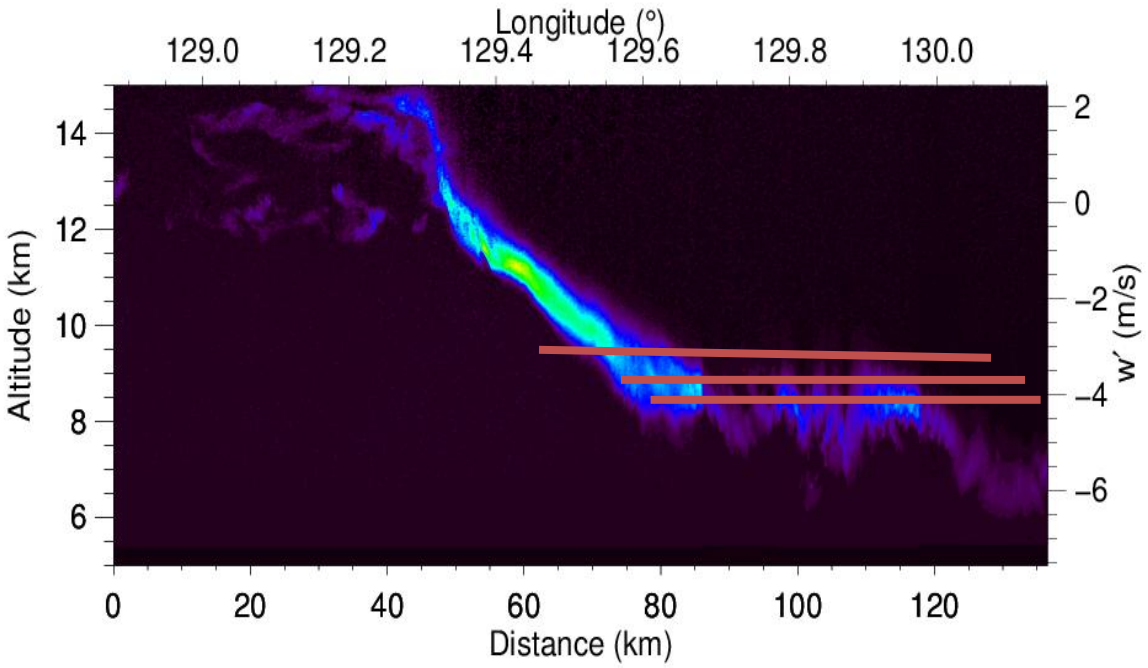

Figure 4.35: sample of stepwise flight leg pattern along outflow conducted on December 2, 2002.

Table 4.4: Properties of December 2, 2002 flight legs for the EMERALD 2 campaign.

EM2 Designation	Altitude (km)	Length (km)
a13dn1	5.00	110.97
a13r1_322	10.37	170.55
a13r2_dn	12.56	151.14
a13r3_281	9.09	64.29
a13r4_dn	8.06	66.28
a13r5_230	7.44	66.36
a13r5_dn	10.47	7.12
a13r6_216a	6.96	76.63
a13r6_216b	6.97	32.79
a13r7_dn	9.11	69.33
a13r8_341	11.04	42.60

Figure 4.36(a) (flight leg a13r2_dn) shows that the anvil cloud base did not always occur at a fixed altitude but sloped dramatically downward by as much as 5 km over a

horizontal distance scale of order 100 km. Fig. 4.36(b) illustrates a more typical scenario where the anvil cloud base height is relatively constant over the flight track distance. Figure 4.36(c) displays one such typical flight leg where the cloud base occurs at an altitude of approximately 8.1 km. Of interest in this leg is the region between approximately 25km and 50 km. The lidar contour plot in Fig. 4.36(c) reveals lobe-like protuberances or deformations, hanging down from the underside of the anvil cloud. This cloud base pattern is interpreted as being mammatus cloud formations, known to frequently be a feature manifested on the underside of the anvil outflow cloud from deep convection (Kanak and Straka, 2009.) These mammatus clouds will be discussed in further detail in the next section (Section 4.12)

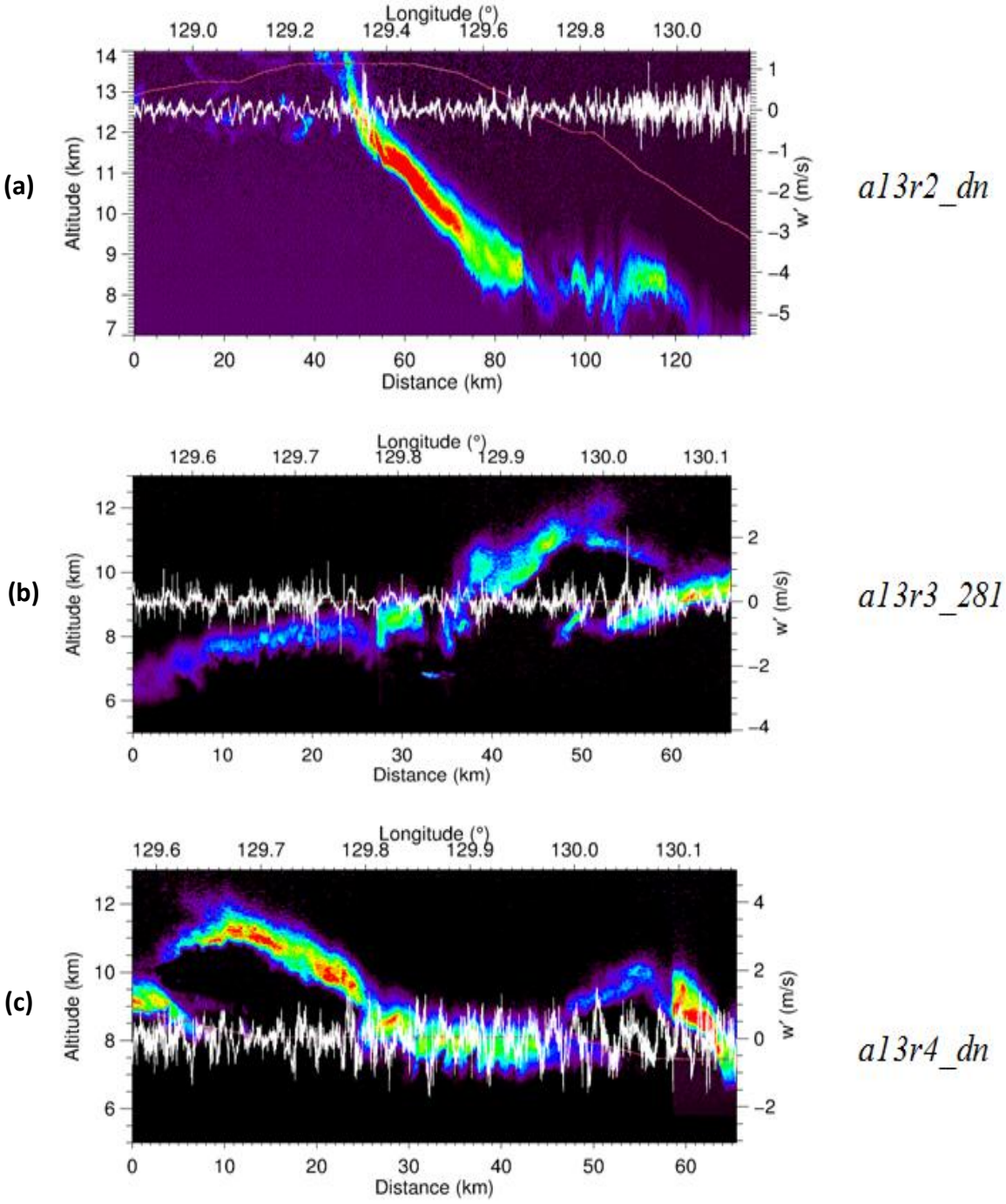

Figure 4.36: Lidar backscatter contour plots of flight legs along the anvil base at varying altitudes from December2, 2002.

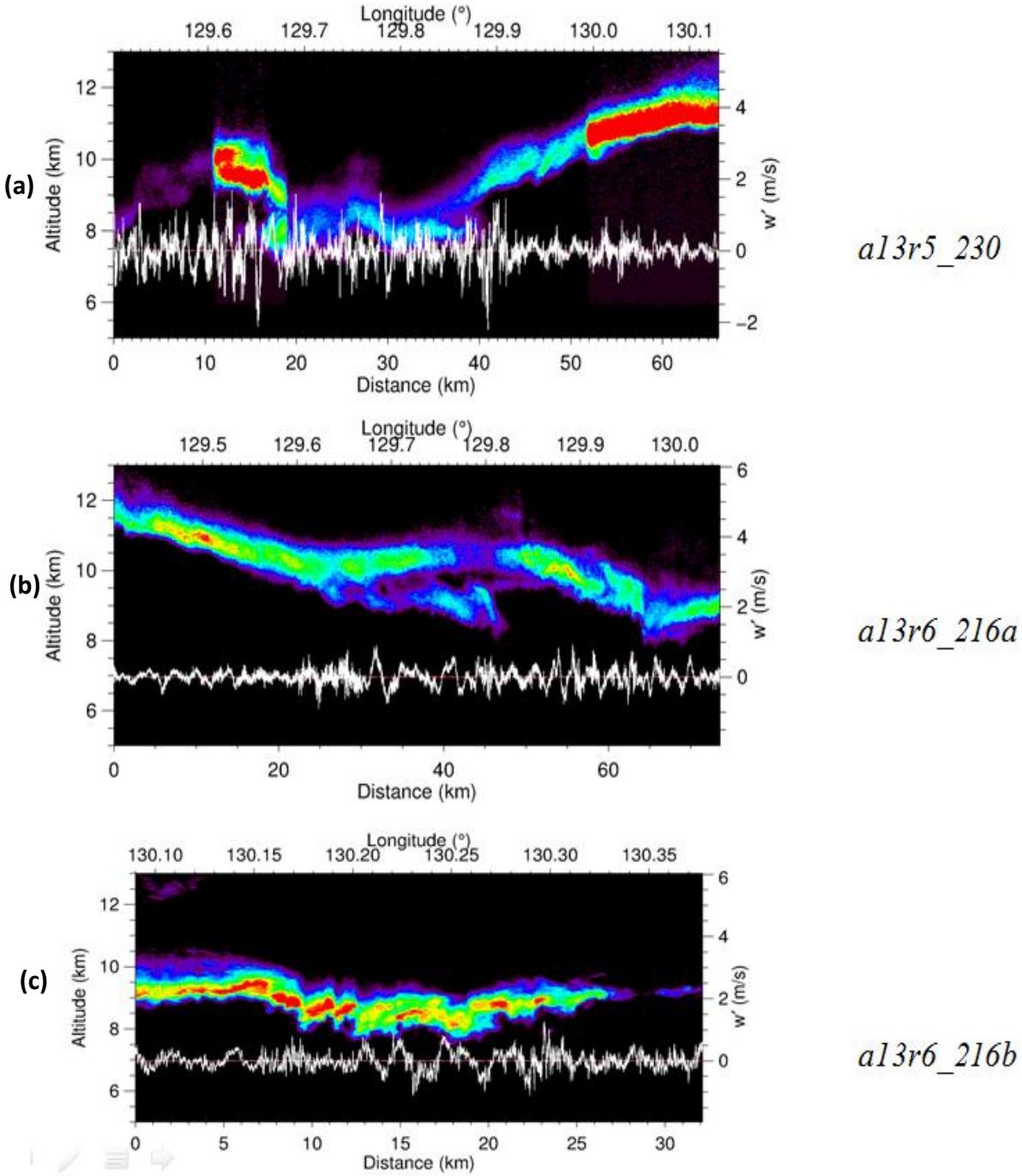

Figure 4.37: Lidar backscatter contour plots of flight legs along the anvil base at varying altitudes from December2, 2002.

The stepwise pattern in flight leg altitudes allowed for the construction of a vertical profile near the cloud base. Figure 4.38 displays the assembled vertical profile constructed from Dec. 2 flight legs spanning various heights within approximately 1 km of the cloud base showing potential temperature, horizontal wind velocities and the TKE.

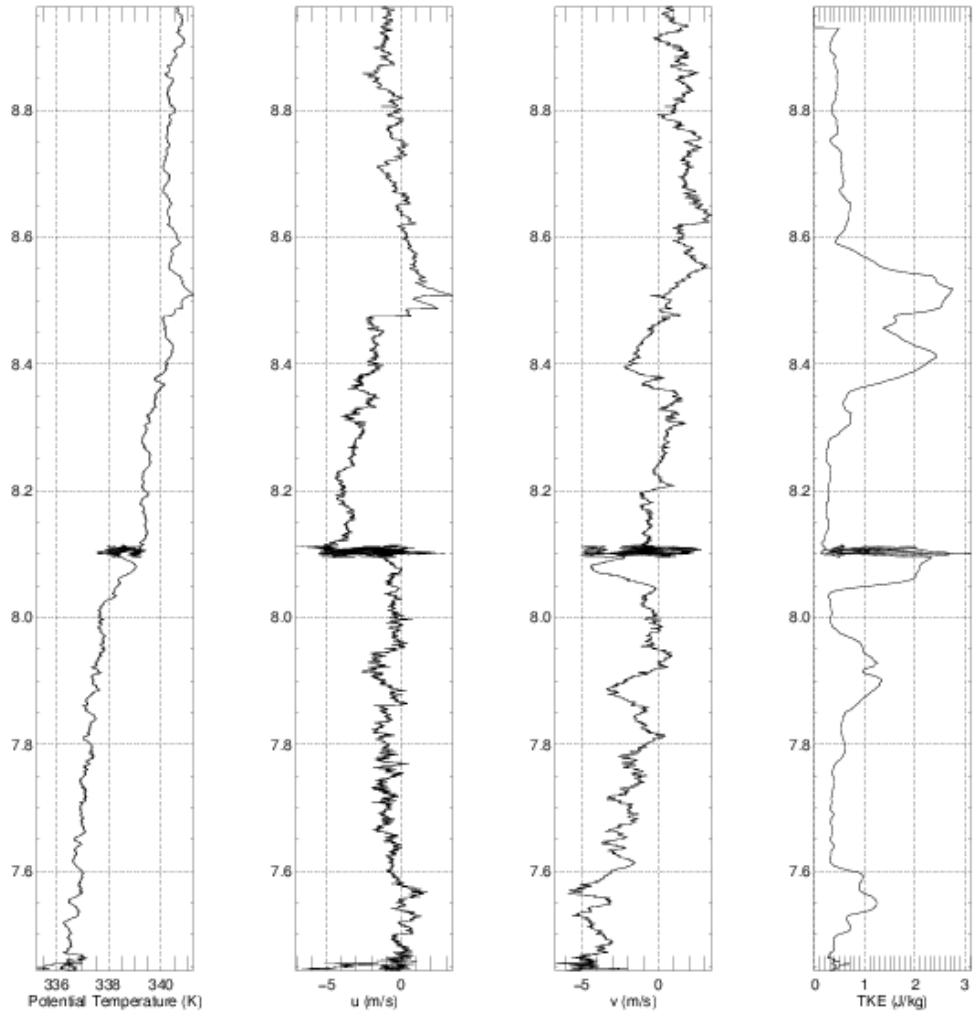

Figure 4.38: Vertical profiles of potential temperature, zonal and meridional wind velocities (absolute, i.e. quantities are u, v, w, not u', v', w') and turbulence kinetic energy in the vicinity of the cloud base (located around 8 km.)

Apparent at the cloud base altitude of 8.1 km is a clear disturbance across all variables. Potential temperature changed significantly (~2°K) upon entering the moist, saturated cloud layer. Winds changed both zonally and meridionally in magnitude by approximately 5 m/s and TKE increased by a factor of at least 2 immediately below and at the base. There is clearly a vast difference in environmental variables above and below the cloud base. Momentum fluxes (Section 3.5) were determined for each altitude of the 11 flight legs conducted and the resultant vertical profile of momentum flux is presented in Fig. 4.39.

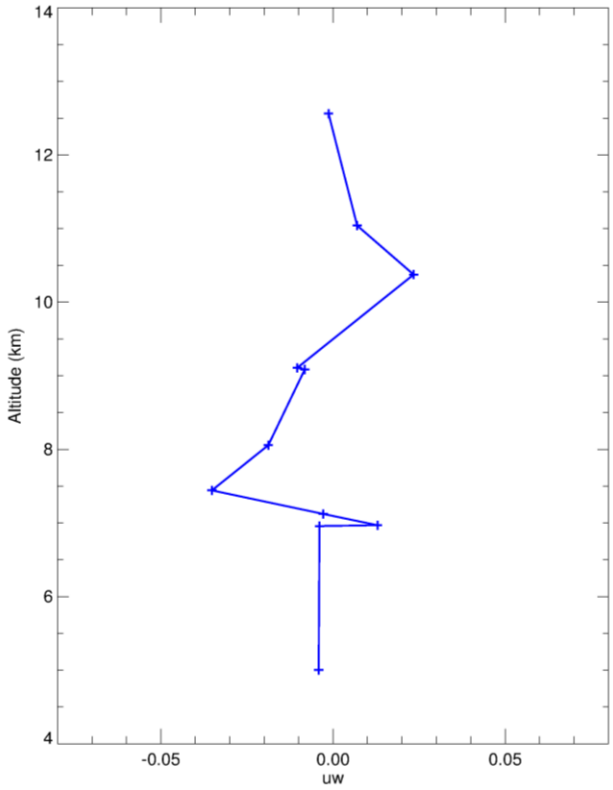

Figure 4.39: Momentum flux in the direction of outflow background wind (u) as calculated for all 11 legs on December 2, 2002. Each point represents momentum calculated over one flight leg from that day.

It is most reasonable to assume that the waves are propagating away from the cloud base, rather than toward it. Then the negative value of the momentum flux below the cloud base (8 km) means that the wave momentum transport occurred downward and eastward. The positive momentum flux above height 8 km means that above the cloud base the momentum transport was upward and eastward.

The interpretation here is that the buoyancy driven oscillations, i.e. high frequency gravity waves, propagate away from the cloud base, both upward and downward, toward the east. The deformations occurring at the base of the anvil cloud combined with increased shear result in strong vertical motions at altitudes around the cloud base and the generation of gravity waves. These conditions likely act together in a manner analogous to flow over a corrugated sheet. This shear flow over corrugations may act as a wave generation mechanism producing wave motions propagating away from the cloud base as illustrated in Fig. 4.40.

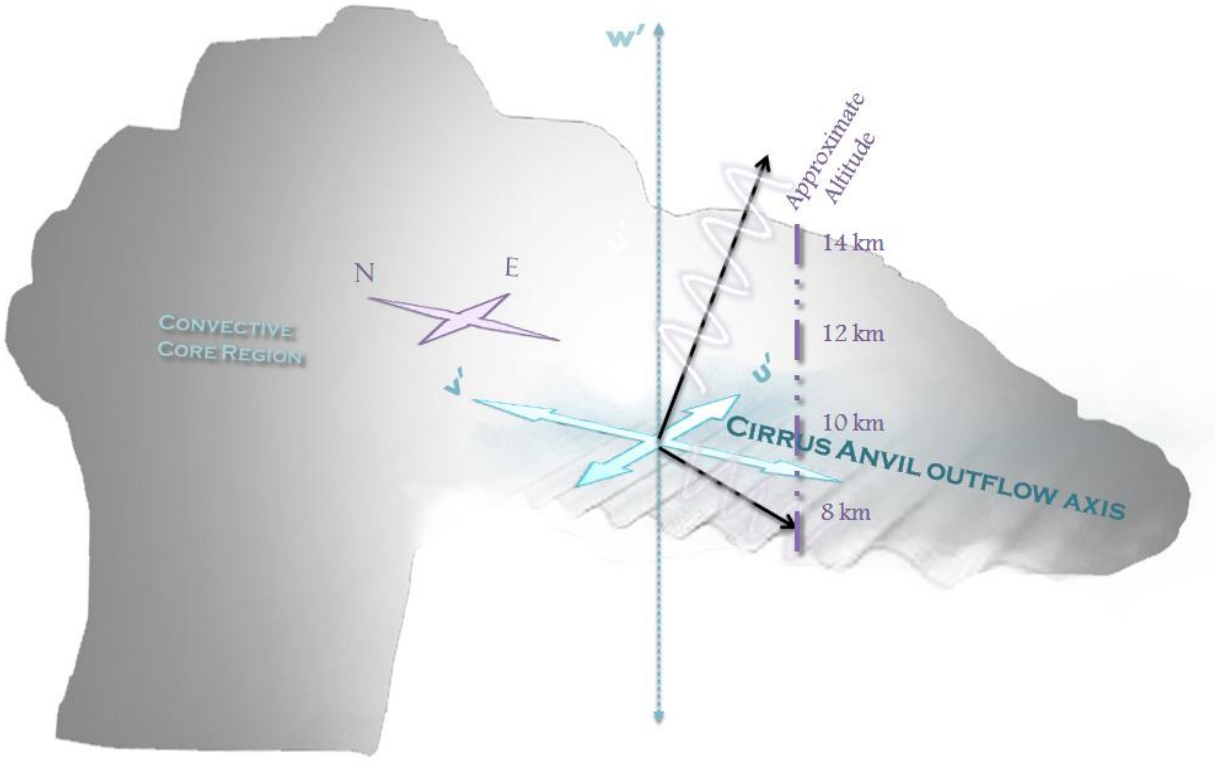

Figure 4.40: Gravity waves propagating upward and downward to the east, away from the cloud base.

4.12 Mammatus Clouds

A close up lidar contour plot concentrating on the mammatus formations described in the last section (see Fig. 4.36 (c)) with overplotted fluctuation in vertical velocity is displayed in Fig. 4.41. The mammatus shown in this contour plot are likely a result of buoyant instability due to cooling by latent heat absorption in sublimation of ice crystals falling into the dry air below the cloud base (e.g. Kollias, 2005).

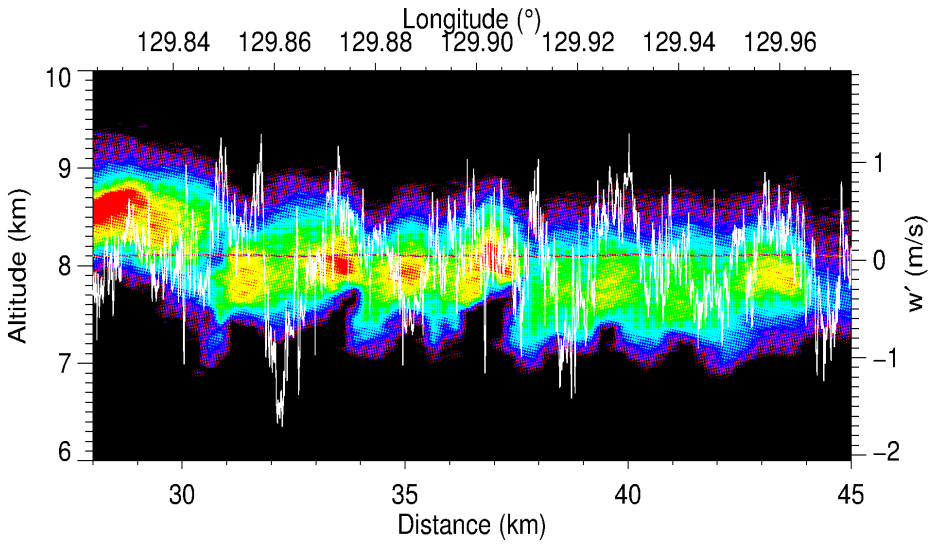

Figure 4.41: Close up of mammatus lobe formations from flight leg a13r4_dn on December 2, 2002.

In Fig. 4.41, mamma appear to be approximately 1 km in diameter, extending downward from the cloud base with a depth of approximately 0.3 km – 1 km. Additionally, correlation of the lidar measurements with the vertical wind perturbation measurements are seen in that one mammatus lobe corresponds with approximately one half a wavelength in vertical velocity fluctuation. Amplitudes in vertical velocity perturbation range from -1.35 m/s to 1.45 m/s. A comparison of observed mammatus properties from other radar and aircraft experiments is presented in Table 4.5.

Table 4.5: Comparison of observed properties of Mammatus

Study	**Year**	**Vertical Velocity (m/s)**	**Horizontal Lobe Extent (km)**
Clarke	1962	n/a	0.25 – 0.75
Warner	1973	-3.1 to -1.2	0.1 – 1
Martner	1995	-3.0 to +0.5	1.1
Stith	1995	-2.5 to +1.0	2-3
Winstead et al.	2001	-3 to -2	1-3
Kollias et al.	2005	-6.0 to +1.5	1-3
Lederman	2014	-1.45 to +1.35	0.3 – 1

From high resolution radar measurements taken of mammatus in mid-latitude cirrus anvil outflow, Martner (1995) postulated that while evaporative cooling plays a large role in shaping the mammatus lobes, especially in creating their smoothness, there must be some underlying wave-like or Rayleigh Bénard cell convection mechanism responsible for their depth and oscillatory structure. Martner's measurements revealed lobes occurring approximately every 1 km. This depth and spacing of mamma is consistent with what is observed in Fig. 4.41 as is the idea of a wave-like or Rayleigh-Bénard convective mechanism underlying mammatus scale and regularity.

Figure 4.42 shows a comparison plot of fluctuation in vertical velocity to potential temperature and horizontal velocities in the mamma region in order to gauge phase relationships.

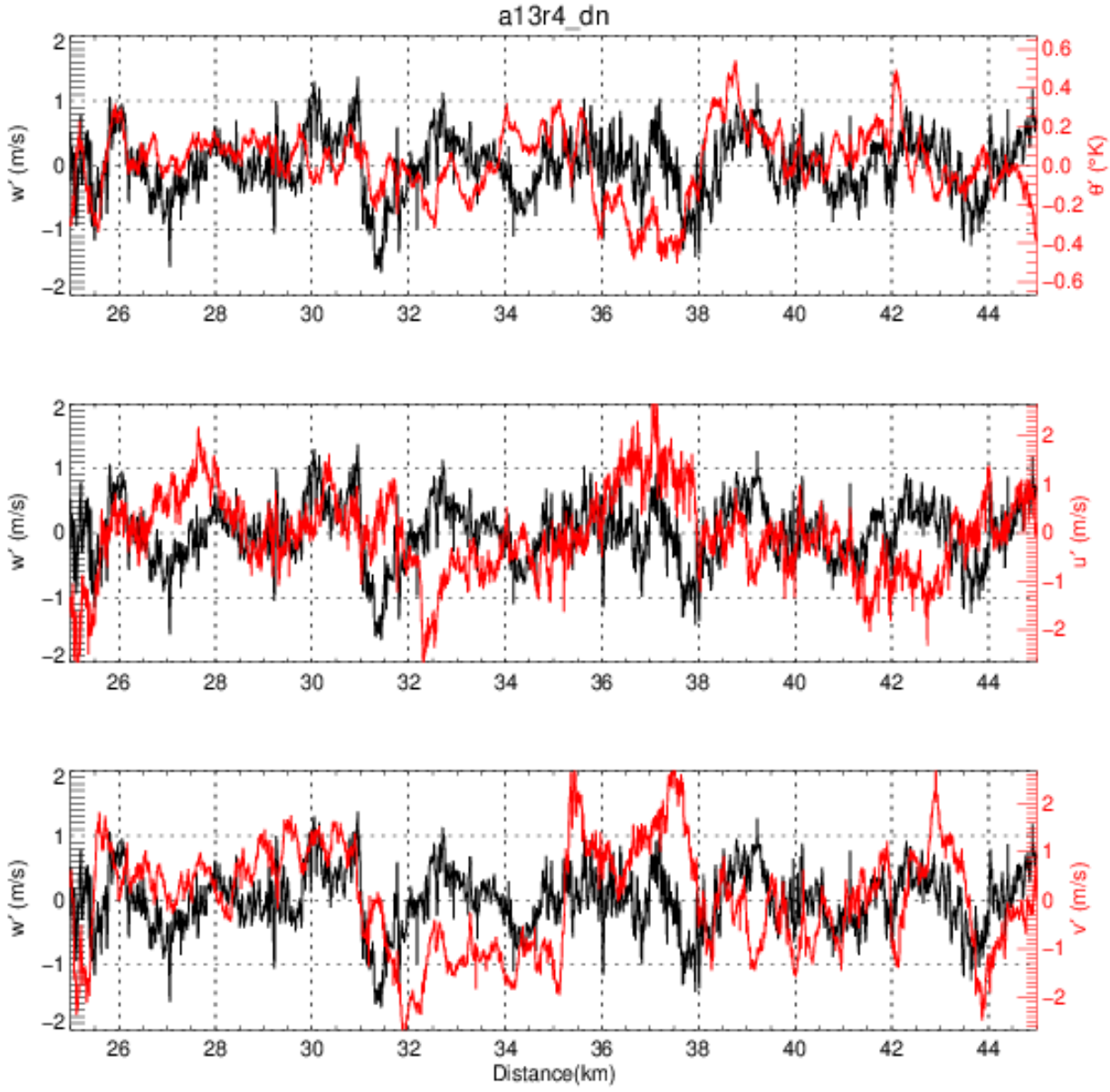

Figure 4.42: Fluctuations of vertical velocity (black) are over plotted against, from top to bottom, fluctuations in potential temperature, zonal, and meridional wind velocities for section of Dec. 2 flight leg a13r4_dn showing mammatus like lobes.

Unfortunately, it is not possible to discern definite phase relations between wind velocities and temperature. This is most likely due to vertical advection of background gradients. Wavelet phase analysis is inconclusive, again most likely due to high shear along the cloud base. Figure 4.43 shows the spectrum associated with the mammatus region. In the inertial subrange, the SR is approximately 0.2 and this is consistent with the shear driven turbulence from Section 4.8.

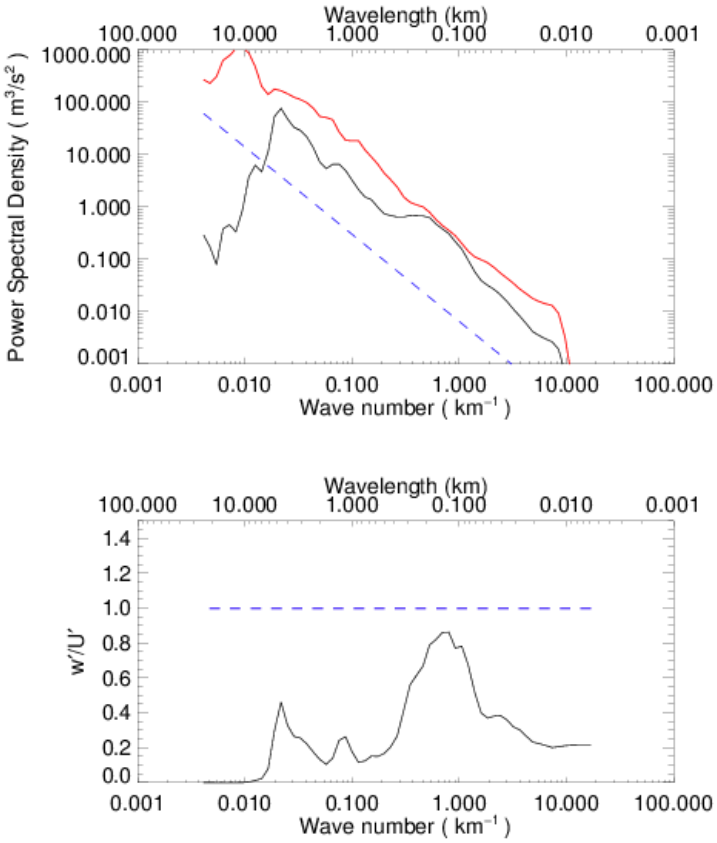

Figure 4.43: (a) PSD for vertical (black) and horizontal (red) wind velocity fluctuations for mammatus region of leg a13r4_dn. -5/3 slope is denoted by blue dashed line. (b) Ratio of vertical to horizontal PSDs. SR = 1 denoted by dotted blue line.

A recent paper by Garrett et al. (2010) presented high resolution numerical simulations of dynamics within the environment of a convective anvil outflow cloud. These simulations produced mammatus structures at the cloud base (altitude of 9 km) with lobes of approximately 0.5 km diameter which is comparable to the lobe diameter shown in the lidar contour plot in Fig. 4.41.

Garrett also provided the PSD of the vertical wind fluctuations at the height of the mammatus lobes and this is shown in Fig. 4.44 in comparison to the measurements from Dec. 2 at the cloud base. There is significant difference between the modeled and measured spectra. The model produces a flat spectrum of fluctuations from scales of 4 km to 100 m and a small spectrum of what appears to be the inertial subrange turbulence (below 100m) with the characteristic -5/3 slope. The measured and modeled spectra exhibit a similar magnitude at a scale of approximately 5 km, however, the measured spectral magnitude then decreases with the -5/3 slope and is substantially different from the modeled spectrum. The measured spectrum does not represent all possible realistic scenarios and consequently does not refute the modeled results, nor does it support the model.

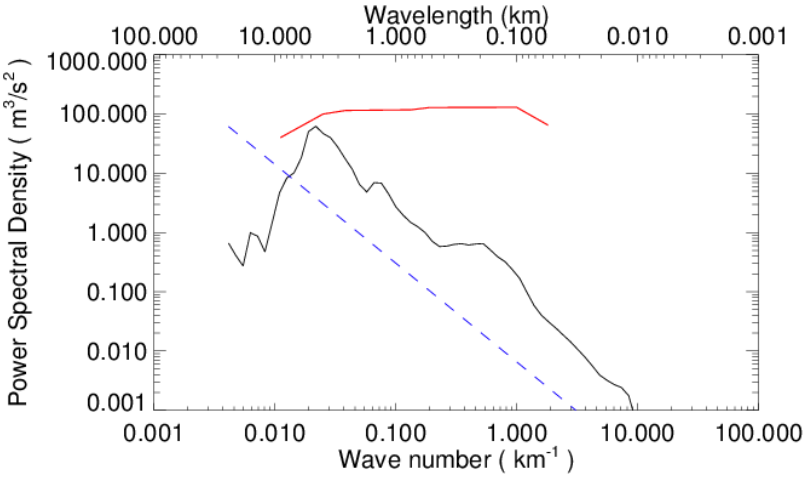

Figure 4.44: Comparison of measured mammatus spectrum (black) to numerical model of mammatus spectrum at anvil cloud base from Garrett, et al, 2010 (red.) Dashed blue line indicates -5/3 slope.

Numerical simulations performed by Kanak and Straka (2009) show that there is a threshold shear value at which Rayleigh-Bénard roll like convective motions evolve into 3d mammatus lobes or laminar stratification (no lobes.) This occurs in the simulations at a shear valued between 0.003 s^{-1} – 0.004 s^{-1} . Figure 4.44 displays graphical results of these simulations for shear values of 0.003 s^{-1}, 0.0035 s^{-1} and 0.004 s^{-1}, respectively.

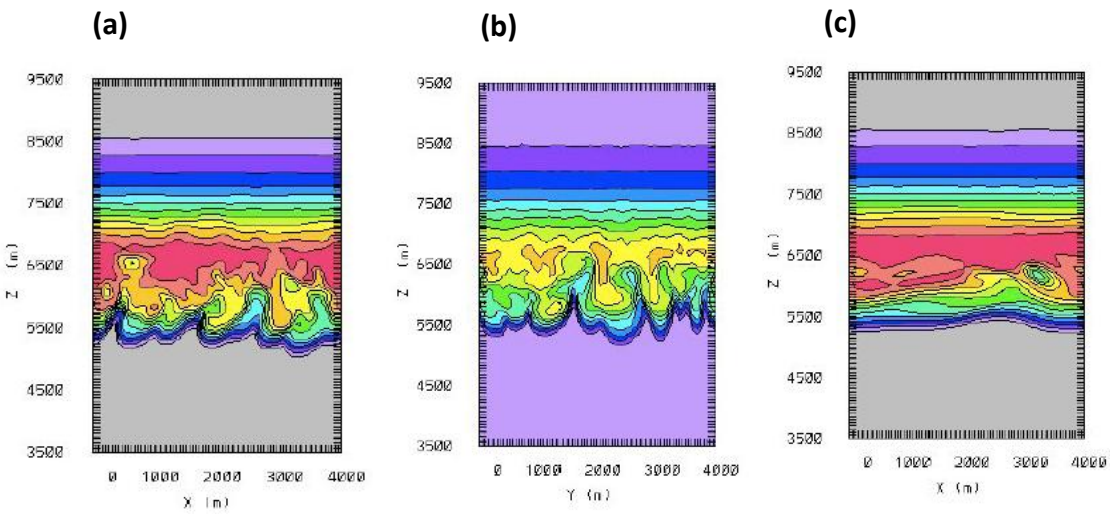

Figure 4.45: Kanak & Straka 2009 numerical simulations for mammatus formation at anvil base for different shear, from left to right, shear values are 0.0030 s^{-1}, 0.0035 s^{-1} and 0.0040 s^{-1}.

Panels (a) and (b) corresponding to shear values at $0.003s^{-1}$ and $0.0035s^{-1}$, appear most visually similar to the mammatus lobes shown in the lidar contour plot of Fig. 4.40. In fact, the shear as calculated from the vertical profiles in Fig. 4.38 near the cloud base is approximately 0.00325 s^{-1} which is consistent with being in the transition region.

Chapter 5: Summary and Conclusions

This thesis described the results of the analysis of measurements of air motions in the anvil outflow from tropical convection. The tropical deep convection was in the form of one of the world's largest annually occurring Mesoscale Convective Systems (MCS), named Hector which is active almost daily in the pre-monsoon period over the Tiwi islands of northern Australia.

An experimental field campaign entitled EMERALD-2 (Egrett Microsphysics Experiment with RAdiation, Lidar and Dynamics) used two aircraft: the Egrett and the King Air. Research flights were conducted out of Darwin, Australia to study the anvil outflow from the deep convection over the Tiwi Islands that occurred almost daily during November and December of 2002. The Egrett aircraft flew through the anvil outflow for in situ measurements up the heights of 15 km. In situ measurements of such quantities as wind velocity, temperature and pressure throughout the outflow were taken with turbulence probes mounted under each wing of the Egrett aircraft. The King Air flew in tandem with the Egrett but at a lower altitude of approximately 5 km with an upward pointing lidar system to map the structure of the anvil cloud.

The EMERALD-2 measurements were compared to two previous campaigns involving the same aircraft and instruments. These campaigns were EMERALD-1 (Adelaide, Australia, September 2001) and the Aberystwyth Egrett Experiment (Wales, May – June, 2000.) The EMERALD-1 campaign investigated the properties of mid-latitude cirrus clouds near Adelaide, Australia, while the Aberystwyth Egrett Experiment

investigated waves and turbulence in the vicinity of the jet stream over Wales. The comparisons revealed the existence of dynamical phenomena unique to the anvil outflow region. The main scientific contribution of this thesis is that it presents analysis of in situ dynamical measurements with sufficient resolution to resolve turbulent fluctuations. This has been the only project to date that has applied aircraft mounted turbulence probes with sufficient temporal resolution to investigate the full range of motions within anvil outflow; from gravity waves and coherent structures at scales of thousands of meters to turbulence at scales as small as 4 meters. Analysis of the measurements from over 100 flight legs from 13 separate flights has resulted in significant findings of phenomena that have not previously been observed in anvil outflow.

The findings (summarized graphically in Fig. 5.1) are as follows.

a). Isolated waves involving less than two oscillations with horizontal wavelengths of 1 km to 3 km were observed within and around the anvil outflow. These were identified as gravity waves since there was a 90 degree phase difference between the wave induced fluctuations in temperature and vertical wind. Comparison with similar waves previously observed over mountains indicated that the waves in the anvil outflow were likely near breaking. The relative amplitude of the horizontal and vertical wind perturbations was used to estimate the frequency of the waves and this was found to be greater than 50% of the buoyancy (Brunt-Vaisala) frequency. In some cases, it was estimated to be equal to the buoyancy frequency and in these cases the observed waves were vertical buoyancy oscillations rather than propagating gravity waves.

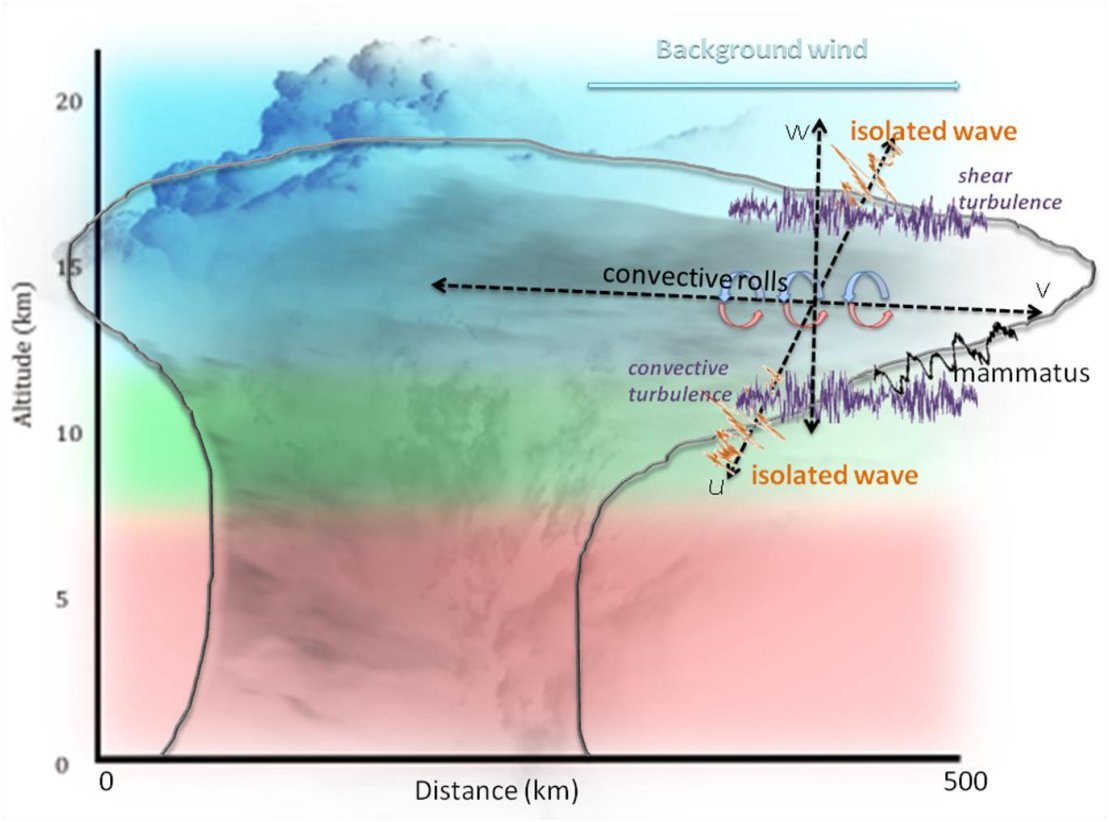

Figure 5.1: Schematic overview of where dynamical phenomena were generally observed in the anvil outflow of tropical convection for the total thirteen flight days of the EMERALD-2 experiment, conducted out of Darwin, Australia, Nov-Dec. 2002. Isolated waves were observed at the anvil edges and throughout the anvil in transverse flight legs while extended, wave-like structures and convective rolls were observed along the length of the outflow axis. Turbulence was observed along the top (shear generated) and bottom (convectively generated) of the outflow. The coloured shading behind the outflow outline roughly depicts local buoyancy conditions as inferred from Ri, i.e. stable (red), neutral (green) and unstable (blue).

b). There were extended waves with several wavelengths observed in the outflow. In some instances, the correlation between temperature and vertical wind were consistent with rolls, specifically, Rayleigh-Bénard convective rolls with diameters of 2 – 2.5 km. The rolls were found only in transverse flight legs and thus were aligned with the anvil outflow axis. The rolls found were effectively sandwiched between the warm cloud base

(heated radiatively from below) and the cold cloud top. This environment constitutes the conditions necessary for Rayleigh Bénard convection.

In other instances of extended waves the correlations between the perturbation variables were consistent with what would be expected for a gravity wave. In a small number of other cases, correlations did not suggest a clear interpretation of whether the coherent structure was a wave or a roll.

c). Turbulence was encountered in patches throughout the anvil where the local Richardson number was less than unity. The intensity of the turbulence was strong relative to similar measurements in mid latitude jet stream shear. Close to the core of the convection the background environment was buoyantly neutral and thus likely unstable in the saturated cloud environment. There was no wind shear in this region and thus the turbulence here was driven by convective instability. Further down wind and near the top of the outflow anvil the environmental temperature gradient was stable, but there was strong shear that caused the turbulence.

d). Anvil outflow turbulence is unique in comparison to previous turbulence measurements at similar altitudes in the jet stream or mid-latitude cirrus clouds. In comparison with shear driven turbulence in the jet stream at mid altitudes, the power spectral density (PSD) of the vertical wind fluctuations in the anvil outflow is significantly greater in magnitude relative to the horizontal wind fluctuations. In the anvil outflow, near to the core of the convection, the PSD of vertical wind fluctuations

was equal to or greater than the PSD for the horizontal fluctuations. In the previous measurements with the Egrett aircraft (EMERALD-1 or Aberystwyth) at midlatitudes it was observed that the PSD of the horizontal wind fluctuation was substantially greater than the PSD of the vertical wind fluctuations

The relative magnitude of the vertical wind fluctuation spectrum decreases at all wavelengths with increasing distance away from the core region of the storm. In the regions of the anvil outflow where the turbulence was generated by shear the relative magnitudes of the vertical and horizontal wind fluctuation, PSDs resembled the measurements in mid-latitude jet stream shear. This was due to the horizontal fluctuations becoming more prominent with distance away from the storm. It was interpreted that this was due to there being larger amplitude turbulent fluctuations in horizontal wind when there is greater shear. This results in the flattening out and confining to the horizontal plane (like a pancake) of the turbulence as it moves away from the core. Such an effect was predicted to occur in the anvil outflow region by Lilly (1983), and it was named "stratified turbulence."

e). Measurements in flights above and below the base of the anvil outflow indicated that the momentum flux was directed both upward and downward, away from the base of the outflow. This was interpreted to indicate that the combination of shear and the undulations in the cloud base produce flow over a corrugated surface which constitutes a mechanism for generating the high frequency gravity waves that were observed throughout the anvil outflow region. It is not clear whether the undulations in the cloud

base were driven by the wave generation or by convective instability associated with either sublimation cooling of in-cloud ice crystals or heating due to absorption of infrared radiation at the cloud base.

In summary, the presented results provide a window into small scale dynamics occurring within the anvil outflow of tropical convection. Results afford new knowledge on high frequency phenomena, such as isolated waves and convective rolls, which were previously unknown and consequently unaccounted for in existing outflow models (for example, Garrett et al., 2004; Garrett et al. 2010, Lilly, 1998.)

Accordingly, future research that could be done includes the integration of the dynamical findings presented in this thesis with the microphysical measurements taken during the EMERALD-2 campaign and previously published (Connolly et al., 2005). Correlations between such properties as ice crystal number density and habit distribution with the occurrence of the coherent structures characterized in this thesis could shed further light on the distribution of water vapour throughout the TTL.

References

Alexander,M. J., P. T. May, and J. H. Beres (2004), Gravity waves generated by convection in the Darwin area during the Darwin Area Wave Experiment, *J. Geophys. Res.*, **109**, D20S04, doi:10.1029/2004JD004729, in press.

Alexander, S.P., T. Tsuda, and J. Furumoto, (2007), Effects of Atmospheric Stability on Wave and Energy Propagation in the Troposphere. *J. Atmos. Oceanic Technol.*, **24**, 602–615. doi: http://dx.doi.org/10.1175/JTECH2046.1

Atticks, M. G., and G. D. Robinson (1983), Some features of the structure of the tropical tropopause, *Q. J. R. Meteorol. Soc.*, 109, 295–308.

Batchelor, G. (1956), The theory of homogenous turbulence. *Cambridge University Press*.

Beer, T. (1974), Atmospheric waves, *John Wiley, New York*, 300 pp.

Beringer, J., N.J. Tapper, and T. D. Keenan, (2001). Evolution of maritime continent thunderstorms under varying meteorological conditions over the Tiwi Islands, *Int. J. Climatol.* **21**, 1021–1036

Betts, A.K., (1990), Greenhouse warming and the tropical water budget, *Bull. Amer. Meteor. Soc.*, **71**, 1464-1465.

Birner, T., A. Dörnbrack, and U. Schumann, 2002: How sharp is the tropopause at midlatitudes?. *Geophys. Res. Lett., 29*, doi:10.1029/2002GL015142.

Bretherton, F. P. (1969), Momentum transfer by gravity waves, *Q. J. Roy. Meteor. Soc.* **95**, 213 243.

Brewer, A. W. (1949), Evidence for a world circulation provided by measurements of He and H20 in the stratosphere, *Q. J. R. Meteor. Soc.*, **75**, 351-363.

Bryan, A. J. Durant, T. J. Garrett, P. M. Klein, and D. K. Lilly (2006), The mysteries of mammatus clouds: Observations and formation mechanisms. *J. Atmos. Sci.*, **63,** 2409–2435.

Carbone, R.E., T.D. Keenan, J. Hacker, and J. Wilson (2000), Tropical island convection in the absence of significant topography. Part I: Life cycle of diurnally forced convection. *Monthly Weather Review*, **128**(10), 3459-3480.

Chui, C.K. (1992), An Introduction to Wavelets. *Academic Press, Inc.* Harcourt Brace Jovanovich, 266 pp.

Clarke, R.H., (1962), Pressure oscillations and fallout downdrafts, *Quart. J. Roy. Meteor. Soc.*, **88**, 459-469.

Connolly, P., C. Saunders, M. Gallagher, K. Bower, M. Flynn, T. Choularton, J. Whiteway, and R. Lawson (2005), Aircraft observations of the influence of electric fields on the aggregation of ice crystals. *Quart. J. RMS,* **608 (b)**, 1695-1712. Doi: 10.1256/qj.03.217.

Cook, C. (2004) Lidar observations of cirrus clouds, *Ph.D. thesis*, University of Wales, Aberystwyth (UK).

Crawford, T., and R. Dobsy (1997), Pieces to a puzzle: air surface exchange and climate, *GPS World,* November.

Crutzen, P. J. (1974), Photochemical reactions initiated by and influencing ozone in unpolluted tropospheric air, Tellus, 26(1–2), 47–57.

Daubechies, I. (1992), *Ten lectures on Wavelets.* Society for Industrial and Applied Mathematics.

Dobson, G. M. (1956), Origin and distribution of the polyatomic molecules in the atmosphere, *Proc. Roy. Soc. Ldn.*, **A236,** 187–193.

Dörnbrack, A. (1998), Turbulent mixing by breaking gravity waves, *J. Fluid Mech.* **375**, 113–141

Dunkerton, T. J., and N. Butchart (1984), Propagation and selective transmission of gravity waves in a sudden warming, *J. Atmos. Sci.*, **41**, 1443-I460.

Dunkerton, T. J. (1987), Effect of nonlinear instability on gravity wave momentum transport, *J. Atmos.Sci.,* **44**, 3188-3209.

Durran, D.R., and J.B. Klemp (1982), On the Effects of Moisture on the Brunt-Vaisala Frequency. *J. Atmos. Sci.,* **39**, 2152-2158.

Farge, M. (1992), Wavelet transforms and their applications to turbulence. *Ann. Rev. Fluid Mech.*, **24**, 395-457.

Fisher B.L., D.A. Short, D.B. Wolff, and O.W. Thiele (1997), The diurnal cycle of precipitation, temperature, and pressure over Melville and Bathurst Islands during MCTEX. *22nd Conference on Hurricanes and Tropical Meteorology, 19–23 May 1997, Ft. Collins, Colorado. American Meteorological Society:* Boston, MA; 370–371.

Folkins, I., and R. V. Martin (2005), The vertical structure of tropical convection and its impact on the budgets of water vapor and ozone, J. Atmos. Sci., 62, 1560–1573.

Folkins, I., R. Chatfield, D. Baumgardner, and M. Proffit (1997), Biomass burning and deep convection in southeastern Asia:Results from ASHOE/MAESA, J. Geophys. Res., 102(D11),13,291–13,299.

Folkins, I. (2002), Origin of lapse rate changes in the upper tropical troposphere, *J. Atmos. Sci.*, **59**, 992–1005.

Folkins, I., and R. V. Martin (2005), The vertical structure of tropical convection and its impact on the budgets of water vapor and ozone, *J. Atmos. Sci.*, **62**, 1560–1573.

Fritts, D. C., and M. J. Alexander (2003), Gravity wave dynamics and effects in the middle atmosphere, *Rev. Geophys.*, **41**, 1003, doi:10.1029/2001RG000106, 1.

Fritts, D. C., T. Tsuda, T. Sato, S. Fukao, and S. Kato (1988a), Observational evidence of a saturated gravity wave spectrum in the troposphere and lower stratosphere, *J. Atmos. Sci.* **45**, 1741-1759.

Fritts, D. C., and R. A. Vincent (1987), Mesospheric momentum flux studies at Adelaide, Australia:Observations and a gravity wave~tidal interaction model, *J. Atmos. Sci.* **44**, 605~519.

Fueglistaler, S., A. E. Dessler, T. J. Dunkerton, I. Folkins, Q. Fu, and P. W. Mote (2009), Tropical tropopause layer, Rev. Geophys., 47, RG1004, doi:10.1029/2008RG000267.

Gabor, D. (1946), Theory of communications. *J. IEEE* (London), **93**, 429-457.

Gage, K. and G. Nastrom (1986), Theoretical interpretation of atmospheric wavenumber spectra of wind and temperature observed by commercial aircraft during GASP. *J. Atmos. Sci*. **43**, 729-740.

Gamache, J.F., and R.A. Houze (1983), Water budget of a mesoscale convective system in the tropics, *J. Atmos. Sci.*, **40**, 1835-1850.

Garrett, T. J., A. J. Heymsfield, B. A. Ridley, M. J. McGill, D. G. Baumgardner, T. P. Bui, and C. R. Webster (2004), Convective generation of cirrus near the tropopause, *J. Geophys. Res.*, **109**, D21203, doi:10.1029/2004JD004952.

Garrett, T. J., C. T. Schmidt, S. Kihlgren, and C. Cornet (2010), Mammatus clouds as a response to cloud base radiative heating. *J. Atmos. Sci*. **67**, 3891–3903

Gettelman, A., P. Hoor, L. L. Pan, W. J. Randel , M. I. Hegglin and T. Birner, The Extratropical Upper Troposphere and Lower Stratosphere (2011), *Rev. Geophys*, **49**, RG3003.

Gettelman, A., and P.M. de F. Forster, 2002: A climatology of the tropical tropopause layer. *J. Meteo. Soc. Japan*, **80**, 911-924.

Gettelman, A., W. J. Randel, F. Wu, and S. T. Massie (2002a), Transport of water vapor in the tropical tropopause layer, Geophys. Res. Lett., **29**(1), 1009, doi:10.1029/2001GL013818.

Giaiotti, D. B., & Stel, F. (2006). The Rankine Vortex Model. *October. University of Trieste*.

Gill, A. (1982) Atmosphere-Ocean Dynamics, *Academic Press.*

Harries J E. (1996) The Greenhouse Earth: A view from space, *Quart. J. RMS*, **122**, 799-818.

Hartmann, D. L., J. R. Holton, and Q. Fu (2001a), The heat balance of the tropical tropopause, cirrus, and stratospheric dehydration, *Geophys. Res. Lett.*, **28**, 1969–1972.

Hartmann,D.L., L. A. Moy, and Q. Fu (2001b), Tropical Convection and the Energy Balance at the Top of the Atmosphere. *J. Climate*, **14**, 4495–4511.

Held, I.M., and B. Soden, (2000), Water vapour feedback and global warming, *Annu. Rev. Energy Environ.*, **25**, 441-475.

Hines, C.O. (1960), Internal gravity waves at ionospheric heights, *Can. J. Phys.* **38**, 1441-1481.

Hines, C. O. (1971), Generalizations of the Richardson criterion for the onset of atmospheric turbulence, *Quart. J Roy. Met. Soc.* **97**, 429-439.

Hines, C. O. (1972), Momentum deposition by atmospheric waves, and its effects on thermospheric circulation, *Space Res.* **12**, 1157.

Hines, C. O. (1988), The generation of turbulence by atmospheric gravity waves, *J. Atmos. Sci.* **45**, 1269-1278.

Hocking, W. (1987), Turbulence in the region 80-120 km. *Adv. Space Res.*,

Hodges, R. R., Jr. (1967), Generation of turbulence in the upper atmosphere by internal gravity waves, *J. Geophys. Res.* **72**, 3455-3458.

Hoinka, K. P., Statistics of the global tropopause pressure, *Mon.Wea. Rev.*, **126**, 3303– 3325, 1998.

Holland G.J. (1986), Interannual variability of the Australian summer monsoon at Darwin: 1952–82. *Monthly Weather Review,* **114**, 594–604.

Holland G.J. and Keenan, T.D. (1980), Diurnal variations of convection over the 'maritime continent' (picture of the month). Monthly Weather Review, **108**, 223–225.

Holton, J. R. (1983), The influence of gravity wave breaking on the general circulation of the middle atmosphere, *J. Atmos. Sci.*, **40**, 2497 2507.

Holton, J.R. (2004) An introduction to dynamic meteorology. *Academic Press, 4th edition.*

Holton, J. R., P. H. Haynes, M. E. McIntyre, A. R. Douglass, R. B. Rood, and L. Pfister (1995), Stratosphere-troposphere exchange, *Rev. Geophys.*, **33**, 403–439.

Houghton, J. (1990), The Physics of Atmospheres. *Cambridge University Press.*

Jourdain, N.C., A. Sen Gupta, A.S. Taschetto, C.M. Ummenhofer, A. Moise, and K. Ashok (2013). The Indo-Australian monsoon and its relationship to ENSO and IOD in reanalysis data and the CMIP3/CMIP5 simulations. *Clim. Dynam*, **41** (11), 3073-3102.

Kaimal, J.C. and J.J. Finnigan (1994), Atmospheric boundary layer flows, their structure and measurements. *Oxford University Press.*

Kanak, K. M. and Straka, J. M. (2009), Effects of linear, ambient wind shear on simulated mammatus-like clouds. *Atmosph. Sci. Lett.*, **10**, 226–232. doi: 10.1002/asl.224

Keenan T.D., Morton B.R., Manton M.J. and G.J. Holland, (1989), The island thunderstorm experiment (ITEX)—A study of tropical thunderstorms in the maritime continent. *Bulletin of the American Meteorological Society*, **70**(2), 152–159

Keenan T.D., Morton B.R., Zhang X.S. and K. Nyguen, (1990), Some characteristics of thunderstorms over Bathurst and Melville Islands near Darwin, Australia. *Quarterly Journal of the Royal Meteorological Society* **116,** 1153–1172.

Keenan T.D., Ferrier B and J. Simpson, (1994), Development and structure of a maritime continent thunderstorm. *Meteorology and Atmospheric Physics*, **53,** 185–222.

Kennedy, P. J., and M. A. Shapiro (1975), The energy budget in a clear air turbulence zone as observed by aircraft, Mon. Weather Rev., **103**, 650–654.

Klostermeyer, J., and R. Ruster (1984), VHF radar observations of wave instability and turbulence in the mesosphere, *Adv. Space Res.* **4,** 79-82.

Koch, S. E., et al. (2005), Turbulence and gravity waves in an upper-level front, J. Atmos. Sci., 62, 3885–3908, doi:10.1175/JAS3574.1.

Kollias, P., I. Jo, and B. A. Albrecht, (2005), High resolution observations of mammatus in tropical anvils. *Mon. Wea. Rev.*, **133,** 2105–2112.

Lane T.P., M.J. Reeder, and T.L. Clark (2001), Numerical modeling of gravity wave generation by deep tropical convection. *J. Atmos. Sci.*, **58**, 1249–1274.

Lane T.P., R.D. Sharman, T.L. Clark, and H-M Hsu (2003), An investigation of turbulence generation mechanisms above deep convection. *J. Atmos. Sci*., **60**, 1297–1321.

Lane, T.P., (2008) Some influences of background flow conditions on the generation of turbulence due to gravity wave breaking above deep convection. *Journal of Applied Meteorology and Climatology* **47** (11), 2777-2796

Lane, T. P., and M.W. Moncrieff (2008), Stratospheric gravity waves generated by multiscale tropical convection. *J. Atmos. Sci.*, **65** (8)

Lane, T.P. (July 27, 2012), media communication, *Sydney Morning Herald.* *http://www.traveller.com.au/turbulence-trouble-planes-flying-too-close-to-storms-211ek*

Lane, T. P., R. D. Sharman, S. B. Trier, R. G. Fovell, and J. K. Williams (2012), Recent advances in the understanding of near-cloud turbulence, *Bull. Am. Meteorol. Soc.*, **93**, 499–515.

Lau, K.M and H. Weng (1995), Climate Signal Detection Using Wavelet Transform: How to Make a Time Series Sing. *Bull. Am. Meteorol. Soc.*, **76** (12), 2391-2402.

Lilly, D. K. (1972), Wave momentum flux--A GARP problem, *Bull. Am. Meteor. Soc.*, **53**, 17-23.

Lilly, D.K. and P. F. Lester (1974), Waves and Turbulence in the Stratosphere. *J. Atmos. Sci.*, **31**, 800–812.

Lilly, D. (1978), A severe downslope windstorm and aircraft turbulence event induced by a mountain wave. *J. Atmos. Sci.* **35**, 59-77.

Lilly, D. (1983), Stratified turbulence and the mesoscale variability of the atmosphere. *J. Atmos. Sci.*, **40**, 749-761.

Lilly, D. K. (1998), Cirrus outflow dynamics, *J. Atmos. Sci.*, **45**, 1594 –1605.

Lindzen, R.S. (1990), Dynamics in Atmospheric Physics, *Cambridge University Press, New York*, 310pp.

Lindzen, R.S., M. Chou, and A.Y. Hou, (2001), Does Earth Have an Adaptive Infrared Iris?, *Bull. Amer. Meteor. Soc.*, **82**, 417-432.

Liou, K.N., and Y. Takano (2002), Interpretation of cirrus cloud polarization measurements from radiative transfer theory. *Geophys. Res. Lett.*,29, doi: 10.1029/2001GL014613, 27-1 - 27-4

Lu, C., and S. E. Koch (2008), Interaction of upper-tropospheric turbulence and gravity waves as obtained from spectral and structure function analyses, *J. Atmos. Sci.*, **65**, 2676–2690, doi:10.1175/2007JAS2660.1.

Ludlum, F. H., and R. S. Scorer (1953), Convection in the atmosphere. *Quart. J. Roy. Meteor. Soc.*, **79**, 317-341.

Lumley, J. and H. Panofsky (1964), The structure of atmospheric turbulence. *Interscience.*

Manabe, S., and R.T. Wetherald, (1967), Thermal equilibrium of the atmosphere with a given distribution of relative humidity. *J. Atmos. Sci.*, **24**, 241-259.

Martin P, (1985), Simulation of the mixed layer at OWS November and Papa with several models. *J. Geophys. Res.* **90,** 903–916.

Martner, B. E. (1995), Doppler radar observations of mammatus. *Mon. Wea. Rev.*, **123**, 3115–3121.

Meyers, S.D., B.G. Kelly, and J.J. O'Brien, (1993), An introduction to wavelet analysis in oceanography and meteorology: With application to the dispersion of Yanai waves. *Mon. Wea. Rev.*, **121**, 2858-2866.

Monks, P.S. (2005), Gas-Phase Radical Chemistry in the troposphere, *ChemInform*, **36,** 33.

Morlet, J (1983), Sampling theory and wave propagation. *NATO ASI Series*, Fl, Springer, 233-261.

Murrow, H.N. (1987), Measurements in atmospheric turbulence, *Atmospheric Turbulence relative to Aviation,Missile, and Space Programs, NASA Conf. Publ.*, 2468, 137-154.

Nappo, C. J. (2002), An Introduction to Atmospheric Gravity Waves, *Academic Press, San Diego, Calif*, 276 pp.

Neale, R. And J.M. Slingo (2003), The maritime continent and its role in the global climate: A GCM study. *J. Climate*, 16, 834-848.

Pavelin, E.G. (2002), Observations of gravity waves, turbulence and mixing in the tropopause region. *PhD thesis*, University of Wales Aberystwyth (UK).

Pavelin, E.G. and J. A. Whiteway (2002), Gravity wave interactions around the jet stream. *Geophys. Res. Lett.*, **29**, 2024.

Pavelin, E.G., J. A. Whiteway, and G. Vaughan (2001), Observation of gravity wave generation and breaking in the lowermost stratosphere. *J. Geophys. Res.*, **106**, 5173-5179.

Ramage, C.S. (1968), Role of a tropical “martime continent” in the atmospheric circulation. *Mon. Weather Rev.*, **96**, 365-370.

Sahai, Y., R. S. Dabas, Y. Otsuka, and M. Klimenko (2012), Low-Latitude Mesosphere, Thermosphere, and Ionosphere, *International Journal of Geophysics*, vol. 2012, Article ID 671240, 2 pages, 2012. doi:10.1155/2012/671240

Sato, K., Tateno, S., Watanabe, S., and Y. Kawatani, (2012), Gravity wave characteristics in the Southern Hemisphere revealed by a high resolution middle-atmosphere general circulation model, *J. Atmos. Sci.*, **69**, 1378–1396.

Schultz, D. M., Kanak, K. M., Straka, J. M., Trapp, R. J., Gordon, B. A., Zrnic, D. S. and D.K. Lilly, (2006). The Mysteries of Mammatus Clouds: Observations and Formation Mechanisms, *J. Atmos. Sci.*, ***63** (10)*, 2409-2435, doi:10.1175/JAS3758.1

Sharman, R. D., S. B. Trier, T. P. Lane, and J. D. Doyle (2012), Sources and dynamics of turbulence in the upper troposphere and lower stratosphere: A review, *Geophys. Res. Lett.*, **39**, L12803, doi:10.1029/2012GL051996.

Skinner, T. and, N. Tapper. (1994), Preliminary sea breeze studies over Bathurst and Melville Islands, northern Australia, as part of the island thunderstorm experiment (ITEX). *Meteorology and Atmospheric Physics* **53**,1-2, 77-94.

Snively, J. B., and V. P. Pasko (2008), Excitation of ducted gravity waves in the lower thermosphere by tropospheric sources, *J. Geophys. Res.*, **113**, A06303, doi:10.1029/2007JA012693

Solomon, S. (1999), Stratospheric ozone depletion: a review of concepts and history. *Rev. Geophys.*, **37**, 275-316.

Solomon, S., D. Qin, M. Manning, Z. Chen, M. Marquis, K.B. Averyt, M.Tignor and H.L. Miller, (2007), Climate Change 2007: The Physical Science Basis. *Contribution of Working Group I to the Fourth Assessment Report of the Intergovernmental Panel on Climate Change.*

Steiner, R. (1966), A review of NASA high-altitude clear air turbulence sampling programs, *J. Aircr.*, **3**, 48–52, doi:10.2514/3.43706.

Stith, J. L., 1995: In situ measurements and observations of cumulonimbus mamma. *Mon. Wea. Rev.*, **123**, 907–914.

Stull, R.B. (1976), Internal gravity waves generated by penetrative convection, *J. Atmos. Sci.*, **33**, 1279-1286.

Tennekes, H., and J. Lumley (1972), A first course in turbulence. *MIT Press*.

Torrence, C., and G. P. Compo, 1998: A practical guide to wavelet analysis. *Bull. Amer. Meteor. Soc.*, **19**, 61–78.

Tsuda, T., M. V. Ratnam, P. T. May, M. J. Alexander, R. A. Vincent, and A. MacKinnon (2004), Characteristics of gravity waves with short vertical wavelengths observed with radiosonde and GPS occultation during DAWEX (Darwin Area Wave Experiment), *J. Geophys. Res.*, **109**, D20S03, doi:10.1029/2004JD004946.

Vincent, R. A., A. MacKinnon, I. M. Reid, and M. J. Alexander (2004), VHF profiler observations of winds and waves in the troposphere during the Darwin Area Wave Experiment (DAWEX), *J. Geophys. Res.*, **109**, D20S02, doi:10.1029/2004JD004714.

Warner, C., (1973), Measurements of Mamma, *Weather*, **28**, 394-397

Weckwerth, T.M., J. W. Wilson, R.M. Wakimoto, and N. A. Crook (1997), Horizontal Convective Rolls: Determining the Environmental Conditions Supporting their Existence and Characteristics. *Mon. Wea. Rev.*, **125**, 505–526.

Weiss, S. and G. Ahlers, The large-scale flow structure in turbulent rotating Rayleigh-Bénard convection, *Journ. of Fluid Mech.* doi:10.1017/jfm.2011.392.

Whiteway, J. A., E. G. Pavelin, R. Busen, J. Hacker, and S. Vosper (2003), Airborne measurements of gravity wave breaking at the tropopause, *Geophys. Res. Lett.*, **30**, 2070, doi:10.1029/2003GL018207,20.

Whiteway, J., et al. (2004a), Anatomy of cirrus clouds: Results from the Emerald airborne campaigns,*Geophys. Res. Lett.*, **31**, L24102, doi:10.1029/2004GL021201.

Whiteway, J. A., G. P. Klaassen, N. G. Bradshaw, and J. Hacker (2004b), Transition to Turbulence in Shear above the Tropopause, *Geophys. Res. Lett.*, **31**, L02118, doi:10.1029/2003GL018509.

Winstead, N. S., J. Verlinde, S. T. Arthur, F. Jaskiewicz, M. Jensen, N. Miles, and D. Nicosia (2001), High- resolution airborne radar observations of mammatus. *Mon. Wea. Rev.*, **129**, 159–166.

Woods, B.K. and R.B. Smith, (2010), Energy Flux and Wavelet Diagnostics of Secondary Mountain Waves. *J. Atmos. Sci*, **67**, 3721-3738. doi: 10.1175/2009JAS3285.1

World Meteorological Organization, (1957), Definition of the tropopause. WMO bull., **6**, 136.

Wroblewski, D.E., O.R. Coté, J.M. Hacker, and R.J. Dobosy, (2007), Cliff–Ramp Patterns and Kelvin Helmholtz Billows in Stably Stratified Shear Flow in the Upper Troposphere: Analysis of Aircraft Measurements. *J. Atmos. Sci.*, **64**, 2521–2539. doi: 10.1175/JAS3956.1